Reconfigurable Integrated Vehicle Stability Control Using Optimal Control Techniques

by

Seyedeh Asal Nahidi

A thesis

presented to the University of Waterloo

in fulfillment of the

thesis requirement for the degree of

Doctorate of Philosophy

in

Mechanical and Mechatronics Engineering

Waterloo, Ontario, Canada, 2017

Examining Committee Membership

The following served on the Examining Committee for this thesis. The decision of the Examining Committee is by majority vote.

External Examiner	NAME: Dong Zuomin Title: Professor
Supervisor(s)	NAME: Amir Khajepour Title: Professor
Internal Member	NAME: Baris Fidan Title: Associate Professor
Internal Member	NAME: Behrad Khamesee Title: Professor
Internal-external Member	NAME: Sebastian Fischmeister Title: Associate Professor

I hereby declare that I am the sole author of this thesis. This is a true copy of the thesis, including any required final revisions, as accepted by my examiners.

I understand that my thesis may be made electronically available to the public.

Abstract

The motivation for the development of vehicle stability control systems comes from the fact that vehicle dynamic behavior in unfavorable driving conditions such as low road-tire adhesion and high speed differs greatly from its nominal behavior. Due to this unexpected behavior, a driver may not be successful in controlling the vehicle in challenging driving situations based only on her/his everyday driving experience.

Several noteworthy research works have been conducted on stability control systems over the last two decades to prevent car accidents due to human error. Most of the resultant stability controllers contain individual modules, where each perform a particular task such as yaw tracking, sideslip control, or wheel slip control. These design requirements may contradict each other in some driving scenarios. In such situations, inconsistent control actions can be generated with individual modules. The development of a stability controller that can satisfy diverse and often contradictory requirements is a great challenge.

In general, transferring a control structure from one vehicle to another with a different drivetrain layout and actuation system configuration requires remarkable rectifications and repetition of tuning processes from the beginning to achieve a similar performance. This can be considered to be a serious drawback for car manufacturing companies since it results in extra effort, time, and expenses in redesigning and retuning the controller.

In this thesis, an integrated controller with a modular structure has been designed to concurrently provide control of the vehicle chassis (yaw rate and sideslip control) and wheel stability (wheel slip ratio control). The proposed control structure incorporates longitudinal and lateral vehicle dynamics to decide on a unified control action. This control action is an outcome of solving an optimization problem that considers all the control objectives in a single cost function, so integrated wheel and vehicle stability is guaranteed.

Moreover, according to the particular modular design of the proposed control structure, it can be easily reconfigured to work with different drivetrain layouts such as all-wheel-drive, front-wheel-drive, and rear-wheel-drive, as well as various actuators such as torque vectoring, differential braking, and active steering systems. The high-level control module provides a Center of Gravity (CG) based error analysis and determines the required longitudinal forces and yaw moment adjustments. The low-level control module utilizes this information to allocate control actions optimally at each vehicle corner (wheel) through a single or multi-actuator regime. In order to consider the effect of the actuator dynamics, a mathematical description of the auction system is included in distribution objective

function. Therefore, a legitimate control performance is promised in situations requiring shifting from one configuration to another with minimal modifications.

The performance of the proposed modular control structure is examined in simulations with a high-fidelity model of an electric GM Equinox vehicle. The high-fidelity model has been developed and provided by GM and the use of the model is to reduce the number of labor-intensive vehicle test and is to test extreme and dangerous driving conditions. Several driving scenarios with severe steering and throttle commands, then, are designed to evaluate the capability of the proposed control structure in integrated longitudinal and lateral vehicle stabilization on slippery road condition.

Experimental tests also have been performed with two different electric vehicles for real-time implementation as well as validation purposes. The observations verified the performance qualifications of the proposed control structure to preserve integrated wheel and vehicle chassis stability in all track tests.

Acknowledgements

Foremost, I would like to express my sincere gratitude to my supervisor Prof. Amir Khajepour, my role model in life, for his ultimate support of my PhD research, patience and enthusiasm. I could not have imagined having a better supervisor for my PhD studies.

Besides my supervisor, I would like to thank Dr. Alireza Kasaeizadeh, my mentor, for his immense knowledge, unhesitating support, and encouragement in all the steps of this research.

I would like to acknowledge the Automotive Partnership Canada (APC), Ontario Research Fund (ORF), and General Motors for their financial support. Special thanks to Dr. Bakhtiar Litkouhi and Dr. Shih-ken Chen at the GM Research and Development Center in Warren for their technical support and valuable comments in improving my research.

Experiments in this thesis could not have been possible without the technicians in the Mechatronic Vehicle Systems laboratory, namely Jeff Graansma and Jeremy Reddekopp.

Last but not the least; I would like to thank my family, my parents, Jalal Nahidi and Simin Hamidini, for supporting me spiritually throughout my life, and my brother, Ata Nahidi, for his unending support during this journey.

Dedication

To my parents for all their love and support and putting me through the best education possible. I appreciate their sacrifices and I would not have been able to get to this stage without them.

Table of Contents

List of Figures

List of Tables

Nomenclature

AVSC	Advance Vehicle Safety Controller
ABS	Anti-lock Braking System
TCS	Traction Control System
ESC	Electronic Stability Control
LSD	Limited Slip Differential
AWD	All Wheel Drive
FWD	Front Wheel Drive
RWD	Rear Wheel Drive
HEV	Hybrid Electric Vehicle
EV	Electric Vehicle
UAV	Unmanned Aerial Vehicle
QP	Quadratic Programming
PWA	Piece Wise Affine
LMI	Linear Matrix Inequality
MMM	Milliken Moment Method
VTD	Variable Torque Distribution
CG	Center of Gravity
SMC	Sliding Mode Control
RHC	Receding Horizon Control
GPC	Generalized Predictive Control
MPC	Model Predictive Control
hMPC	Hybrid Model Predictive Control
NMPC	Nonlinear Model Predictive Control
HCC	Holistic Corner Control

LTV	Linear Time Variant
LPV	Linear Parameter Varying
DLC	Double Lane Change
TV	Torque Vectoring
AS	Active Steering
AFS	Active Front steering
ARS	Active Rear Steering
DB	Differential braking
ϑ	Control input
Θ	Control input sequence based on MPC prediction model
Θ^*	Transformed control input sequence
y	Control output
ξ	Actual (estimated/measured) state
ξ_{des}	Desired state
Ω	Predicted states over prediction horizon of N
Ω_{des}	Desired states over prediction horizon of N
N_p	Prediction horizon
N_c	Control horizon
N	Equal prediction and control horizon
A_t	Continuous system matrix
B_t	Continuous input matrix
C_t	Continuous known disturbance matrix
A_k	Discretized system matrix
B_k	Discretized input matrix
C_k	Discretized known disturbance matrix

L	Weight of state tracking error
R	Weight of control effort
$\bar{L}$	Diagonal weight of state tracking error
$\bar{R}$	Diagonal weight of control effort
$S^{\xi},\ S^{\vartheta},$ S^{c}	Batch approach matrices of MPC solution
$F_{X_{CG}}$	Total CG longitudinal force
$F_{X_{des}}$	Total desired CG longitudinal force
$F_{Y_{CG}}$	Total CG lateral force
$F_{Y_{des}}$	Total desired CG lateral force
$G_{Z_{CG}}$	Total CG yaw moment
$G_{Z_{des}}$	Total desired CG yaw moment
$G_{w_{ij}}$	Total torque of wheel ij
$F_{x_{i,j}}$	Longitudinal force of tire ij
$F_{y_{i,j}}$	Lateral force of tire ij
$F_{x_{brk}}$	Burkhardt model longitudinal force
$F_{y_{brk}}$	Burkhardt model lateral force
$F_{x_{act}}$	Measured longitudinal force
$F_{y_{act}}$	Measured lateral force
L_f	Distance between vehicle CG and front axle
L_r	Distance between vehicle CG and rear axle
L	Vehicle wheel base
L_w	Half of the vehicle wheel track
R_e	Effective wheel radius

m	Vehicle mass
I_z	Vehicle moment of inertia around vertical axis
J_ω	Wheel moment of inertia
θ_i	Road steering angle at i^{th} axle
u	CG longitudinal velocity
v	CG lateral velocity
r	CG yaw rate
ψ	Yaw angle
λ_{ij}	Slip ratio of ij tire
$\lambda_{threshold}$	Slip ratio threshold
S_{res}	Resultant tire slip
$\bar{C}_\alpha$	Tire cornering coefficient
μ	Road friction coefficient
c_1, c_2, c_3	Burkhardt tire model coefficients
α_{ij}	Tire ij slip
α_{ij_0}	Initial tire ij slip
$\mathrm{L_v}$	MPC lateral velocity weight
$\mathrm{L_r}$	MPC yaw rate weight
$\mathrm{L_\psi}$	MPC yaw angle weight
$\mathrm{L_{\lambda_{max}}}$	MPC maximum slip ratio weight
$\mathrm{R_{F_{x_f}}}$	MPC front axle longitudinal force weight
$\mathrm{R_{F_{x_r}}}$	MPC rear axle longitudinal force weight
$\mathrm{R_{G_z}}$	MPC yaw moment weight
E	HCC model based error

$\delta\mathcal{F}$	All corner horizontal force variations
$\delta\mathcal{F}_i$	All corner horizontal force variations at discretized time step i
$\delta\bar{\mathcal{F}}$	
$W_{d\mathcal{F}}$	HCC optimization control action weight
$W_{d\mathcal{F}_{act}}$	
W_E	HCC optimization CG error weight
W_{F_X}	HCC optimization CG longitudinal force weight
W_{F_Y}	HCC optimization CG lateral force weight
W_{G_Z}	HCC optimization CG yaw moment weight
T_s	Sampling time
D	Size of time window for desired yaw angle calculation
τ	Actuation system time-constant

Chapter 1

Introduction

1.1 Motivation

According to Transport Canada's National Collison Database, there were 1834 motor vehicle fatalities in 2014 [1]. The federal, provincial and territorial governments in Canada intend to reduce traffic related fatalities and serious injuries with both long-term and short-term plans of improving road safety. These accidents usually take place in unpleasant driving conditions such as situations with low road friction coefficients and high speeds. In these conditions, the behavior of the vehicle as a complicated nonlinear dynamic system may differ from the driver's expectation. For non-professional drivers, adequate response in critical driving situations is considered a challenging task. In recent decades, researchers devoted a serious effort to design Advanced Vehicle Safety Controllers (AVSC) to assist drivers in critical driving situations. Anti-lock Braking System (ABS), Traction Control System (TCS), and Electronic Stability Control (ESC) all emerged to provide stability and enhance vehicle handling. Although an impressive improvement has been achieved in vehicle stability control technologies hitherto, further investigation is still required to minimize road accidents [2-4].

Vehicle stability is considered supplementary to road safety for an overall safe drive experience. Since vehicle and road interaction occurs through their contact point, stability controllers target tires to correct the vehicle response. A locked or spinning tire provides less longitudinal force compared to a rolling tire. This highlights the importance of wheel dynamics control to provide enough grip for control adjustments. As wheel dynamics is much faster than vehicle dynamics, a preventive approach is usually more effective in comparison to a restorative approach. In this approach, traction control does not allow excessive tire slip by regulating the driver's requested torque. If traction control is incorporated with stability control, final control adjustment will be generated by optimally assisting in conservation of both longitudinal and lateral stabilities.

From the above discussion, it can be concluded that a preventive approach is preferable to a restorative one. To adopt this approach, a control algorithm should have a feature of

forecasting the impending tire saturation and compensate for it in advance by adjusting wheel torque. In control terminology, such a control algorithm is referred to as a Model Predictive Control (MPC). A model predictive control algorithm relies on a dynamic model and can provide insight into future system behavior. According to the foreseen behavior of the system, an optimal control action is found that minimizes a given cost function with specific criteria.

Furthermore, the MPC technique allows for the consideration of dynamic delays that may exist in all practical systems. These time delays can originate from actuation system or sensor communication lags. As a concern, the time-response of an actuation system plays a significant role in providing sufficient and punctual control effort. For instance, according to functionality properties of a torque distribution system, the generated torque may be different from what is desired resulting in degradation of the control performance. In order to counteract the adverse effect of control action evolution delay, the MPC prediction model can be upgraded with a mathematical description of the respective actuator.

In order to enhance stability and performance, a vehicle may be equipped with multi actuators. The vehicle stability control by means of actuation systems can be classified in three important categories as differential braking, active steering, and active torque distribution. As mentioned before, the vehicle stability control can be considered as adjusting tire longitudinal and lateral forces in a planar motion. Any of the aforementioned actuation systems intends to rectify vehicle safety and mobility by controlling one of the horizontal tire forces. Among all stability actuators, differential braking has received the most attention since it can be executed on almost all vehicles regardless of configuration and drivetrain. In this method, a negative differential torque adjusts the longitudinal tire force for traction and yaw moment control to follow the target dynamics. On the other hand, active steering control regulates driver steering command and consequently adjusts lateral tire forces for lateral stability and minor yaw moment control. Torque distribution devices such as center couplers and Limited Slip Differentials (LSD) in conventional vehicles and electric motors in electric vehicles generate negative/positive torque at wheels for torque vectoring and integrated wheel and chassis stability control purposes. It was shown that incorporating different actuation systems allows for better stability control and provides more flexibility for vehicle stabilization when actuators are restricted in boundaries. In addition to a variety of actuators with particular properties, different vehicle configurations such as Front-Wheel-Drive (FWD), Rear-Wheel-Drive (RWD), and All-Wheel-Drive (AWD) are required to be considered in control action decision making.

Designing a control structure that is implementable with a number of actuators and drivetrain arrangements requires not only constrained optimal control algorithms to adopt the best feasible solution but also modularity. Modularity allows for the differentiation between two obligations. The first obligation is stability analysis, and the second one is how to process this analysis to achieve the desired vehicle dynamics with available actuation system(s) in a certain vehicle configuration.

1.2 Proposed Control Structure Design Objectives

In order to design a vehicle stability controller with the highlighted features, the following objectives have been set:

- **Integrated Vehicle Chassis and Wheel Control:**

  The first objective of this thesis is to develop a combined longitudinal and lateral stability controller. In this methodology, instead of designing a separate module for slip ratio control, the requested adjustment of the integrated controller maintains vehicle chassis and wheel stability (sideslip and slip ratio control), and minimizes over/understeering (yaw rate control) yaw rate error in critical driving situations. Consider a driving scenario such as acceleration in turn on a slippery road condition, where tire capacity is limited to maximum longitudinal and lateral forces that can be generated through road and tire contact. In this condition, maintaining the vehicle stability can be considered as a challenging task, can be interpreted as an optimal compromise between longitudinal and lateral stabilities such that certain criteria should be achieved with minimal effort. In this study, in order to address this issue, a model predictive strategy will be utilized to anticipate impending wheel and vehicle slip and provide an integrated stability.

- **One Controller - Any Car:**

  The second objective of this thesis is designing a controller that can be implemented on any vehicle with any actuator and powertrain configuration with no significant modifications and tuning. This objective has been achieved with a modular control structure. Figure 1.1 shows a schematic of the proposed control structure. The high-level module is responsible for vehicle CG error analysis. In this level, regardless of actuation system functionality and characteristics, an analysis can be conducted on vehicle CG horizontal forces and yaw moment for error detection. In a low-level module, the required adjustment at the wheels in accordance with the available actuation system can be found optimally considering actuator restrictions. The vehicle drivetrain configurations that are

studied in this research are AWD and RWD, and the actuators have a variety of electric motors, differential braking, active steering, or any of their combinations.

In addition, a modular control structure can effectively reduce computational burden for a real-time solver and provide a ground for module-to-module developments.

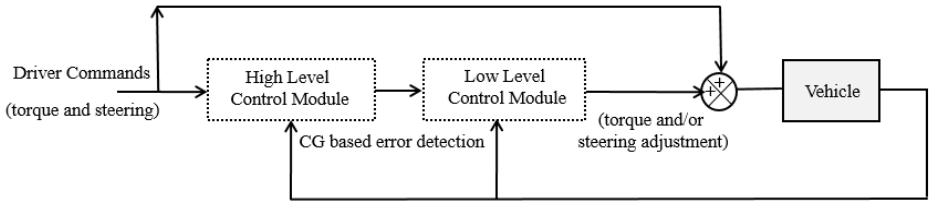

Fig 1.1 Schematic of the proposed modular control structure

- **Actuation System Constraint and Dynamic Modelling Treatment:**

  Vehicle stabilization is susceptible to actuator functional properties and dynamic responses. The third objective of this thesis is to design a control structure that is capable of working properly with a variety of actuators with different time-responses and extremities. In order to consider the effect of actuation dynamics and time-response, a corner based single-step optimization in the low-level control is upgraded to a multi-step one. Multi-step optimization allows anticipation of control action evolution trend and compensation for any possible time-delay. Moreover, the employed constrained optimal control strategy in low-level module allows for actuation restrictions in decision-making.

- **Robustness:**

  Vehicle stability maintenance is usually considered a more demanding task on a slippery road condition where tire force capacity is less in comparison with dry road condition. The fourth objective of this thesis is to provide a controller that is capable to show a robust performance on different road conditions and driving scenarios. In order to fulfill this objective, instead of constraining the desired dynamic behavior of the vehicle to road condition that is difficult to be estimated, robustness is achieved through controlling the lateral skidding of the vehicle indirectly.

  In addition, the proposed control structure should be able to run in real-time for experimental verification purposes on RWD and AWD GM Equinox electric vehicles.

1.3 Thesis Outline

The second chapter of this thesis reviews literature of vehicle stability control. The importance of the vehicle stability control and handling enhancement, particularly in

adverse road conditions, are discussed. The literature review of vehicle stability control is focused mainly on the techniques that adopt a constrained optimal control and model predictive control strategies.

The third chapter is devoted to introducing constrained optimal control techniques that have been utilized in this thesis. First, a mathematical description of a dynamic system in a general linear time-varying state-space model is considered as a prediction model. A batch approach is employed to adopt MPC formulation, and an analytical optimal solution with side constraints is provided for MPC optimization. Second, the concept of vehicle CG force and moment error analysis for the purpose of corner control is discussed, and finally, background knowledge of a holistic corner control technique is presented.

In the fourth chapter of this thesis, a modular control structure for integrated longitudinal and lateral vehicle stability control (vehicle chassis and wheel stability control) via torque vectoring is developed. In the high-level module, a predictive control approach is utilized to determine the required CG longitudinal force and yaw moment adjustments to achieve the desired dynamics. An analytical Burkhardt tire model has been employed in the MPC prediction model to consider the combined slip situations and tire longitudinal and lateral force interactions. A cost function that is considered for sideslip, yaw rate, yaw angle, and slip ratio control with torque vectoring method is introduced. Then, optimization constraints due to actuation system limitations are developed. The optimization problem is presented in quadratic programming form. Using the QP analytical solving method presented in the previous chapter, the optimum control action is obtained. Then, using MPC outputs, an optimal distributor generates the required torque adjustment at each wheel. Experimental results are illustrated as a close-loop response of an electric AWD GM Equinox vehicle with the proposed controller interventions. The capability of the controller in stabilizing the vehicle in severe driving conditions is demonstrated.

The fifth chapter presents a control scheme design for the integrated longitudinal and lateral stability control through combined active steering and torque vectoring. Implementation of the proposed control structure on different vehicle configurations with different actuation systems is feasible due to CG based error analysis in the high-level module. Different vehicle drivetrains, such as RWD and AWD, and different combination of actuators, such as electric motor-active steering and differential braking-active steering, are tested in simulation and experimental evaluations. According to these evaluations, the proposed control structure is capable of working with the aforementioned actuators. It has also been

shown that a better performance is achieved with multiple actuators in extreme driving situations, and less torque/braking intervention is required with steering correction.

In sixth chapter of this thesis, in order to consider the effect of actuation system dynamics on vehicle stability control, the distribution algorithm in the low-level control module is modified with actuator evolution model. Instead of a single-step optimization in low-level control, a multi-step optimization is proposed, which is to be conducted while considering the dynamic development trend of required control action. The developed multi-step control approach is based on a holistic corner control method that uses CG error analysis from the proposed high-level control module. A sluggish electrohydraulic differential braking system was modeled and used to evaluate the effectiveness of the proposed approach. According to the simulation and experimental results, it was illustrated that actuation modelling can greatly improve the handling performance.

In chapter seven, the conclusion and contributions of this thesis are highlighted. In addition, some possible future work to continue this research is mentioned.

Chapter 2

Literature Review

2.1 Introduction

In this chapter, a literature review on vehicle stability analysis and control is presented. The major concentration is on constrained optimal control methodologies such as a model predictive and optimal control allocation methodologies such as holistic corner control that can be employed for optimal vehicle stability maintenance. Since the constraints on vehicle stability control mainly originate from the actuator characteristics and limitations, different actuators as well as their functionality constraints will be discussed according to various research works.

2.2 Envelope Control

In order to evaluate and analyze the stability of a vehicle, a region can be defined according to the behavior of the vehicle dynamics where maintaining the vehicle within this region can be interpreted as a control success. The driver is allowed to maneuver up to the safety limits with no instability risk and control interventions. This concept can be considered as an envelope control that was originally applied to aircrafts. A broad spectrum of constraints exist for different aircrafts such as safety limitations on angle of attack, pitch, bank angle, and speed, all of which contribute to aircraft safety [5] . However, for ground vehicles, the definition of a safe envelope is restricted to measurements of speed, yaw rate, sideslip angle, and road adhesion coefficient. Recent developments in model-based estimation assists in the identification of handling limits and facilitates real-time envelope control.

2.3 Vehicle Stability Analysis Based on Phase Plane Approach

The lateral dynamics of a vehicle is usually described with a two-state model. In order to design an envelope, the phase plane is employed to visualize the vehicle stability analysis. An open-loop trajectory of a vehicle on a phase plane can be plotted by setting a constant forward speed and steering angle. The vehicle is considered to be stable if it converges

onto a steady equilibrium point, and it is considered to be unstable if it diverges. For a locally and globally valid stability analysis, encompassing a nonlinear tire model and its effects on the phase plane parameters is essential. According to previous research, the phase plane method has normally been concentrated on two sets of dynamic states: sideslip-sideslip rate or sideslip-yaw rate, shown in Fig 2.1. In this terminology, yaw rate r refers to the vehicle heading angle change and sideslip angle, and β refers to the angle between the longitudinal tire axis and the velocity vector of vehicle CG. The trajectories in Fig 2.1 are generated using initial conditions on the vehicle sideslip and the yaw rate or the sideslip rate at a constant forward speed and steering angle. The gray areas are considered unstable since divergence of trajectories is observed.

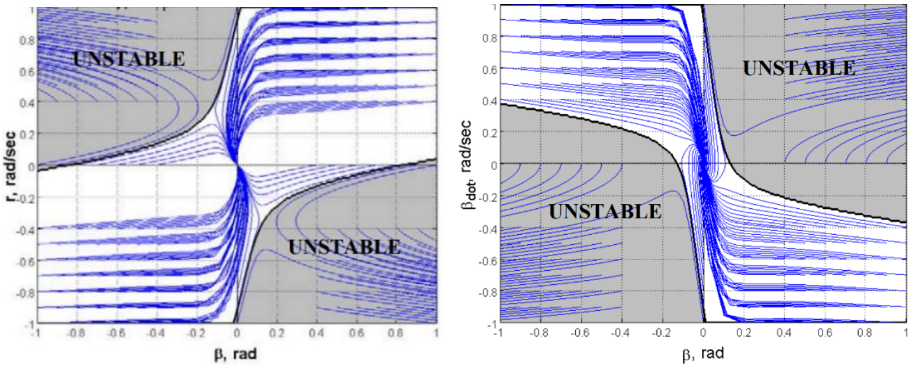

(a) **(b)**

Fig 2.1 Typical phase planes (a) sideslip-yaw rate (b) sideslip rate-sideslip [6]

Inagaki et al. inquired the stable region of a vehicle with the $\beta - \dot{\beta}$ phase plane [6]. They illustrated that despite the $\beta - r$ phase plane, in the $\beta - \dot{\beta}$ phase plane, the saddle and equilibrium points move along a horizontal axis, where $\dot{\beta}$ vanishes. That was the main reason that they preferred to use the $\beta - \dot{\beta}$ phase plane. However, their provided stability region is based on an open-loop stability analysis of a vehicle, and may not be useful for a real situation when the driver is operating.

Although many researchers proposed sideslip and sideslip rate phase portraits for vehicle stability analysis, none of these dynamic states is measured in production cars. Vehicle sideslip can be computed using lateral and longitudinal CG velocity estimations, and sideslip rate can be obtained with the derivation of a computed sideslip with respect to time. Hoffman et al. introduced an alternative approach introduced as the Milliken Moment Method (MMM) that calculates vehicle reaction forces based on steering θ and sideslip β angles [7]. Using the time history of states θ and β, a dynamic maneuver can be mapped

onto the yaw moment coefficient (C_N) – lateral acceleration (a_Y) diagram. A lookup table is usually provided for the mapping process, and the safety boundaries are correlated with tire saturation. An example of this mapping is shown for a driving maneuver at vehicle speed of 70 km/hr. The proposed MMM method was verified with the standard $\beta - \dot{\beta}$ phase plane stability method.

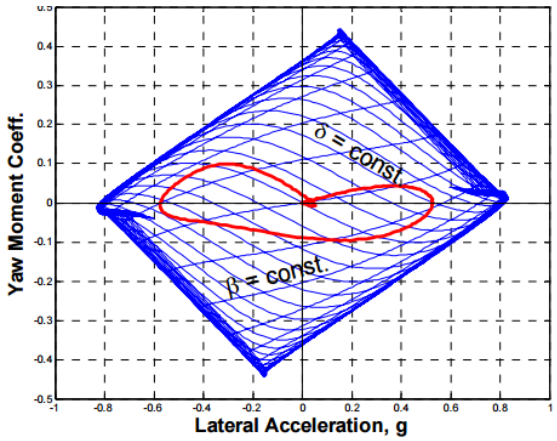

Fig 2.2 Typical MMM diagram and trajectory [7]

However, this approach to overcoming obstacles using the $\beta - \dot{\beta}$ phase plane stability analysis in practice is shifting toward the use of the $\beta - r$ phase portrait. Yaw rate is measured with simple IMU systems found on every production car, which makes stability analysis based on yaw rate instead of sideslip rate more convenient. Another privilege of using yaw rate is that it can be directly corrected with available actuation systems such as differential braking, active steering, and torque vectoring.

Crolla et al. proposed an integrated Active Front Steering (AFS), Active Rear Steering (ARS), and Variable Torque Distribution (VTD) to improve vehicle handling and directional stability [8]. Stand-alone steering controllers are designed to improve the yaw rate tracking on low to mid traction surfaces using Sliding Mode Control (SMC) algorithm, while VTD is responsible for generating the required yaw moment when the sideslip angle exceeds the stable region defined in [9] with a proportional control algorithm. This methodology detects vehicle instability when vehicle sideslip angle becomes relatively large (more than 6 degrees) and yaw rate tracking is lost.

Ono et al. investigated vehicle stability using a saddle-node bifurcation in the $\beta - r$ phase plane. They designed a steering controller to prevent vehicle spin and improve handling performance [10]. It was shown that with steering adjustments, the rear lateral forces are

controlled to avoid tire saturation. The stability analysis also validated the competency of the steering controller tested in the simulation environment.

Yasui et al. analyzed the stability of the vehicle transient response through a $\beta - r$ phase plane in slalom driving scenarios in simulation and experiment. An external yaw moment was generated using a hydraulics brake system to correct the vehicle response [11]. As an envelope control approach, the yaw moment never reestablishes before tire is saturated and the friction limit is reached. In another different research, Klomp studied the $\dot{\beta} - \dot{r}$ phase plane for primary instability detection in Electronic Stability Control (ESC) systems using the $\dot{\beta} - \dot{r}$ phase plane [12].

2.4 Vehicle Stability Analysis Based on Reference Tracking Approach

According to the literature review on vehicle stability control, there are two emulating perspectives in controller design. One perspective is restricting the vehicle in a safe region, which is discussed through envelope control, and the other one is tracking a reference vehicle behavior at all times (no boundary). A vehicle model with the desired dynamic response (usually desired yaw rate and sideslip) is used to define the reference signals.

Manning and Crolla published a review paper that focuses on vehicle stabilization with different objectives such as yaw rate, sideslip, and combined yaw rate and sideslip control [8]. The yaw control objective is mainly responsible for enhancing the steerability of the vehicle while the sideslip angle is viewed from stability perspective and should consistently be small if not zero. Although several research works only concentrate on yaw rate control, the combined yaw rate and sideslip control approach provides a better handling performance and stability. This approach often incorporates two or more actuators or only uses one with nonlinear and linear control strategies.

Cho et al. designed a unified chassis controller with reference to a yaw tracking approach [13]. In this unified chassis controller, different control modules such as differential braking and active steering were incorporated to achieve lateral stability and maneuverability. Longitudinal and lateral tire force adjustments were carried out optimally to provide the required yaw moment with minimal longitudinal deceleration and speed drop. The performance of the controller was tested and compared to conventional electric stability controllers with CarSim simulations.

Abe et al. used a sliding surface algorithm to stabilize the sideslip using direct yaw control [14]. The sideslip angle is estimated utilizing a linear model based observer. Precise tracking of reference sideslip angle via direct yaw control is a difficult task to accomplish, however, experimental data shows the controller's success in vehicle stabilization. Driving scenarios in experiments included a single and double lane change with harsh maneuvering. Furthermore, it was indicated that sideslip control is more influential in case of stability deterioration due to the tires' nonlinear behavior.

Hong et al. employs a yaw rate and slip tracking approach for steerability and stability enhancement [15]. The longitudinal and lateral vehicle dynamics are considered in an integrated manner for a superior performance, and controlled through a braking system. The actuator generates the required yaw moment as well as sufficient longitudinal force adjustments for yaw rate, sideslip, and optimal longitudinal slip tracking. In order to consider the nonlinear characteristics of lateral tire force, a lookup table was established based on steady-state cornering simulations of a full vehicle model. The controller performance was evaluated in a double lane change maneuver with a hardware-in-the-loop simulator.

According to literature, stability controllers are designed to constantly control the vehicle to follow the desired dynamics even in less severe maneuvers when stability is not a matter of concern. In many studies, the desired yaw rate is defined based on vehicle speed, steering command, geometrical properties of the vehicle, and road adhesion coefficient, while the sideslip angle is minimized to zero. From a stability point of view, minimization to zero can be considered desirable, but it might lead to a conservative control since the restriction of the sideslip to small value ($\leq 6°$) would be sufficient. Although state tracking is an effective approach to stabilize a vehicle, it is sensitive to vehicle model and state estimation/measurement uncertainties.

2.5 Vehicle Stability Control Using Optimal Control Algorithms

Up to this point, the vehicle stability analysis has been discussed using a safe envelope or reference signal approaches. In order to maintain the vehicle within safe bounds or follow target dynamics, a control adjustment may be required on the vehicle. This control adjustment is the output of a control system with a particular control algorithm. The performance of a controller is generally evaluated in terms of time and frequency domain

criteria [16]. Complex, multi-input, and multi-output control systems that may have radically different performance criteria can be designed via modern control algorithms. Optimal control is one special branch of modern control that provides the best possible outcome, and in spite of classical control it is not sufficient enough to be stable [17]. The objective of optimal control theory is to determine a control law that minimizes (or maximizes) some performance criterion while satisfying physical constraints. An optimal control problem can be identified with:

- A mathematical presentation of the process that requires control.
- A statement of the physical constraints.
- An objective or performance criterion.

Vehicle stabilization is a constrained optimal control problem due to contradictory criteria (pleasant maneuverability requires non-zero sideslip) and actuator limitations. Some actuation limitations can be pointed out as electric motor power capacity, torque transferability ratio of limited slip differential, or active steering correction limit. Incorporation of different actuation systems may add more complications to constraint treatment. In order to address these design requirements, two constrained optimal control algorithms known as Model Predictive Control (MPC) and Holistic Corner Control (HCC) are proposed. The former offers a model based optimal solution with explicit constraint satisfaction that distinguishes it from other optimal control approaches in vehicle stability control. As a significant development has been achieved on real-time computational hardware devices, where the MPC has become more of the center of attention. The latter also offers an optimal solution with soft constraint satisfaction that is extendable somewhat to include a dynamic model, but it is best fit to be employed for optimal control allocation based on a model based error.

2.5.1 Model Predictive Control

Among several forms of optimal control algorithms, a model predictive control also known as Receding Horizon Control (RHC) has received a lot of attention from researchers in recent decades. In this control strategy, a mathematical description (model) of a system is used to predict its behavior over a finite/infinite horizon of time [18]. This MPC algorithm allows for the solution of optimal control problems such as tracking problems (minimization of discrepancies between predicted and reference signals) subject to constraints considering the impact of current control action on the future behavior of a

system [19]. Constrained optimization with the MPC algorithm has encouraged many researchers to use it in many automotive control aspects other than vehicle stability control.

Li et al. designed an adaptive cruise control in order to improve tracking capability, fuel economy, and driver desired response [20, 21]. The high-level control module is an MPC based on objectives of minimal tracking error and fuel consumption, and additionally, car-following features constrained to longitudinal ride comfort, tracking range, and rear-end safety. The computational impracticalities are overcome with constraint softening approaches. The low-level control module compensates for nonlinear vehicle dynamics and aims to follow target acceleration. Simulations on a heavy truck have been performed to study the competency of the controller to fulfill the objectives. It was concluded that the proposed controller was capable of improving fuel economy without sacrificing safety and tracking performance in comparison to the baseline controller.

Del Re et al. used an MPC for the engine control problem, which has a considerable impact on the emission of passenger cars [22]. The control system had to enable the vehicle to follow a standard speed profile under normal circumstances while maintaining the mean emission under a certain threshold and fulfilling the customers' requirements. The MPC boasts multi-objectiveness with possible conflicting targets, and constraints such as injection times and quantities, recirculating gas valve position, and turbocharger position require the MPC since it stand outs thanks to its constrained optimization algorithm.

Moreover, the model-based nature of the MPC provides a prediction of the system behavior that is a highly appealing feature in case of actuation, sensor, and communication delays in a system [23]. Li et al. studied a group of decoupled agents prone to communication delays with a distributed MPC whose efficiency for large-scale control systems has been proven. A waiting mechanism is considered in the MPC scheme that compensates for communication delays. The stability and feasibility characteristics of the controller was evaluated, and it was depicted that under certain conditions, the system is stable. Some simulations have been provided to show the effectiveness of the approach [24].

Luo et al. utilized an MPC approach to provide a dynamic control allocation algorithm that considered actuation dynamics. The goal is to generate a non-redundant control action to address control objectives subject to a set of constraints. The actuation dynamics is taken into account directly as a hard constraint in the MPC prediction model. The approach is extendable to encompass a number of actuation dynamics without any general change in

the control scheme, and simulation results shows qualifications of this generic approach in comparison with the baseline control scheme.

The MPC prediction model plays a significant role in the performance of the controller. The predictive model should be accurate enough to capture the most significant dynamics of the system, and at the same time, simple enough for real-time implementation [25]. Linear prediction models are less costly in computation and implementation; however, nonlinear models for particular purposes such as vehicle stability control in a nonlinear tire force region are superior in terms of accuracy [26, 27].

Falcone et al. proposed a path following Nonlinear Model Predictive Control (NMPC) based control structure via combined differential braking and active steering [28]. Two controllers are designed to achieve the obstacle avoidance objective. One is designed based on a simple bicycle vehicle model, and the other one is designed based on a ten degree of freedom full vehicle model. The former controller is compared to the later one in terms of performance and computational burden in vehicle stabilization in low and high speeds. It was shown that with the simplified vehicle model, real-time implementation of the controller is feasible, but performance at high speeds will be sacrificed. Whereas, fair simulation comparisons show that the MPC optimization process with full a vehicle model is very time-consuming, but could stabilize the vehicle both at low and high speeds.

Palmieri et al. incorporated the roll dynamics in a simple bicycle vehicle model for a path following problem through an AFS system [29]. Expanding the prediction model with roll dynamics to consider the load transfer effect showed a remarkable stability improvement in double lane change maneuvers on low traction surfaces and high speeds.

2.5.1.1 Nonlinear Model Predictive Control

The Nonlinear Model Predictive Control (NMPC) is referred to as an MPC algorithm that employs a nonlinear prediction model to forecast the system behavior. As mentioned above, the main advantage of using a nonlinear prediction model is a prediction of the vehicle response in a broader range of operations with more accuracy. Therefore, the global dynamics of a system can be described better with a nonlinear model, and this is the most compelling reason for researchers to investigate NMPC.

Borhan et al. studied the NMPC to design a power management system for a Hybrid Electric Vehicle (HEV) equipped with a planetary gear set to synthesize and divide the power of the electric motor and combustion engine [30]. Two cost functions were optimized at each sampling time to divide the power between the electric motor and

combustion engine to achieve best fuel economy. A high-fidelity model is used to simulate different driving cycles and evaluate the effectiveness of the approach on power management. The results illustrate a remarkable improvement in comparison with available software on market and LTV MPC energy management systems.

Borrelli *et al.* investigated an NMPC control approach for autonomous vehicle stabilization through active steering constrained to actuation limitations [31]. This study was a part of ongoing internal Ford research activities where the NMPC was first offered in [32], and it was then continued to be investigated for more specific purposes. These purposes can be summarized as increasing the stability region of the controlled system in comparison with linear controllers, examining computational burden of a nonlinear controller, and generating a baseline controller to compare its performance with sub-optimal controllers. The nonlinear programming problem has been solved using commercial an NPSOL software package in [33]. NPSOL is a set of FORTRAN programs designed for constrained optimization that may encompass linear and nonlinear smooth bounds on state variables. In addition, the effect of preview steps on the desired path in different speeds has been highlighted, and a minimum prediction horizon is provided for an acceptable performance at a certain speed. The simulation results show that complex steering maneuvers such as a double lane change on a snow-covered road with a speed of 17 m/s could be controlled using the proposed MPC feedback policy. Similar research works have been conducted in [34, 35] using the NMPC. Although satisfactory results have been obtained even for relatively severe maneuvers, the computational burden is a serious obstacle for experimental validation and real-time implementation. Some alternative approaches are suggested to manage the computational complexities such as using piecewise linear models or linear models.

2.5.1.2 Hybrid Model Predictive Control

The Hybrid Model Predictive Control (hMPC) is considered to be an MPC algorithm that employs a Piece Wise Affine (PWA) approximation of future system behavior. According to the literature, in PWA systems, the state-input space forms polyhedral regions, and each region has an affine equation that defines the system dynamics [36]. In a trade-off between prediction precision and complexity, hybrid dynamic models can be considered as proper alternatives instead of nonlinear ones [37, 38]. Hybrid prediction models result in a mixed integer/linear quadratic programming that can be solved using software packages such as SCIP [39].

Di Cairano et al. investigated vehicle stability control using an hMPC that coordinates multiple actuation systems such as differential braking and active steering [40]. In this control structure, the MPC is allowed to switch between linear and saturated force models, but not during the prediction horizon since that was assumed constant at each sample time. The preliminary evaluation of the controller showed that real-time execution of the structure is feasible on current automotive electronic units in terms of computational load and memory. It could achieve high performance on low friction surfaces in experimental tests.

Borrelli et al. studied an anti-skidding system based on an hMPC where a mixed-logical dynamic hybrid model of the open-loop system is provided [41]. According to this modelling, an optimal PWA controller is designed using multi-parametric programming approaches. The design flow allows for more a detailed description model and easy extendibility. The performance of the controller is assessed experimentally on a test vehicle, and it was depicted that the controller is robust in different driving scenarios without ad-hoc supervision or logical interventions.

2.5.1.3 Linear Time-Varying Model Predictive Control

Although stability control of vehicle dynamics is usually needed in the nonlinear range, real-time execution of the NMPC and hMPC is not a simple task to accomplish. Therefore, many studies have been conducted based on the use of a successive linearization of a nonlinear model to avoid nonlinear constrained optimization. Although this approach may provide a sub-optimal control technique, it requires considerably less computational effort.

Bemporad and Rocchi applied a hierarchical LTV MPC approach on Unmanned Aerial Vehicles (UAVs) while considering constraints such as motor thrust, vehicle angle and position, and collision avoidance [42]. The LTV MPC approach utilizes a simplified dynamic model of the stable UAV and a novel convex approximation of the feasible state. Simulation results illustrated a satisfactory level of performance in comparison with more complicated hybrid prediction models with a minor performance sacrifice and less computational complexity. The proposed approach provides a 3D path in real-time that is more favorable since in a real-life situation, the position of the obstacle might not be known in advance or before flight operation.

Canale et al. reduced the computational complexities of a nonlinear MPC with an efficient approximation method based on a set membership technique [19]. The performance of the controller was tested with software-in-the-loop simulations and was compared to a more

accurate nonlinear model. The reported performance of the controller was satisfactory in comparison with the accurate nonlinear model; however, it is more advantageous over the nonlinear one due to its real-time implementation feasibility. They also investigated the stability and constraint satisfaction of the proposed approximate NMPC controller in control demanding conditions. The stability analysis demonstrated that the controller is able to handle a system with nonlinearities, constraints, and model uncertainties in a systematic way.

Falcone et al. used a sub-optimal LTV MPC controller based on successive online linearization around the operating point of the nonlinear vehicle model to tackle the path tracking problem of an autonomous vehicle [28]. The control inputs were front steering angles that were applied to the active steering actuation system in order to follow the appropriate trajectory on slippery roads. Although the predictive model was linear, the effectiveness of the proposed MPC formulation was proven by simulation and experimental tests up to 21 m/s on ice covered roads. The major contribution of this study is to present a linear MPC controller with acceptable performance. In another work, they investigated the vehicle stability problem of an autonomous vehicle through an LTV MPC with combined active front steering, active braking, and active differentials [43]. The desired trajectory is assumed to be known at each sampling time, and control inputs are calculated in order to competently follow it on a slippery road condition with a certain forward speed. Successive online linearization similar to their previous work has been done with multiple actuation systems for integrated longitudinal and lateral stability control. The simulation results are compared to cases when only steering/braking actuation is available.

2.5.2 Holistic Corner Control

According to the control structure requirements and design objectives, an optimal control allocation technique is selected to be reviewed known as Holistic Corner Control (HCC). This optimal control algorithm was first used by Chen et al. for vehicle stabilization. According to this research, an analytical approach to control the tire forces (corner) based on the CG is described [44]. A cost function, based on the CG's actual and desired horizontal forces and yaw moment is minimized in real-time to stabilize a vehicle in severe driving maneuvers. As control actions are longitudinal and lateral tire forces, they are constrained to a maximum capacity on a certain road condition and specific tire properties. The tire reserve is considered to be a soft constraint in the cost function. In case of tire saturation, the corresponding weight increases exponentially and becomes dominant in the

cost function. The control algorithm has been verified using CarSim simulations with spike maneuver in a double lane change that may push the tire forces into nonlinearity. A crucial feature of this tire-force based holistic corner control methodology is that it does not require a complex combined-slip tire model since tire forces are generated directly as control actions. In most tire models, longitudinal slip, lateral slip, and normal load are considered to be variables of the tire force functions [45-48] According to this fact, CG error minimization can be accomplished also by controlling the corner slip instead of corner force. In another study, Pylypchuk et al. studied HCC optimal distribution methodology that is designed based on a precise combined slip tire model developed using hyperbolic and trigonometric functions. The control methodology is tested in simulations by driving the vehicle into nonlinear and non-stable driving conditions. It was concluded that the corner force based approach is more robust against tire model uncertainties.

Kasinathan et al. extended the HCC methodology by adding actuation constraints to the optimization problem [49, 50]. The methodology is applicable on conventional/electric vehicles with differential braking, hybrid torque vectoring on front wheels and differential braking on rear wheels, and other configurations by constraint alteration. Simulation and experimental results show that the methodology can handle linear constraints for a real-time implementation.

Fallah et al. worked on the gain optimization of the HCC methodology using Linear Matrix Inequality (LMI) and Genetic Algorithm (GA) techniques [51]. A modular control structure is used where the high-level control module interprets driver request to the desired vehicle dynamics and motion, and in the low-level module using corner based control, the discrepancy between actual and desired vehicle dynamics is minimized. Similar to previous HCC based study, the adaptivity feature of the control algorithm to different vehicle configurations is also confirmed.

2.6 Integrated Vehicle Stability Control

In addition to lateral stability control (yaw rate and sideslip control), longitudinal stability control is also a substantial task that is generally analyzed based on tire slip ratios [52-57]. If tire slip ratios exceed a certain threshold on a specific road condition, it can be interpreted as the saturation of tires in the longitudinal direction and a lack of capacity in the lateral direction. This phenomenon leads to loss of track on lateral dynamics and significant understeer or oversteer situations during turning maneuvers. A traditional technique to

maintain the tire slip ratios under a certain threshold is to design a separate traction/brake control module along with a yaw controller that does not allow for an excessive slip ratio.

However, it is evident that the longitudinal and lateral capacity of the tire should be occupied optimally to achieve best vehicle dynamic behavior. Although the design of a separate module to control the tire slip ratio decreases modelling and control complexities, it may not result in a superior performance. An optimal compromise between longitudinal and lateral stability control can be obtained when the wheel and vehicle chassis dynamic states are integrated and studied as a single control module [58, 59].

Zhou *et.al* investigated the integrated wheel slip and vehicle lateral stability control problem since the state variables of the MPC prediction model includes yaw rate, sideslip angle, and slip ratio [60]. The performance evaluation of the proposed integrated controller is illustrated in simulations with consideration of differential braking as an available actuation system.

Li et al. studied longitudinal, lateral, and integrated longitudinal and lateral tire force models to design an ABS [61]. According to this study, it was seen that in pure-slip tire models there is a risk of deteriorating the wheel slip while improving handling or vice versa. However, the combined slip tire models provide a more considerate decision on the allocation of the differential braking forces for integrated stability purposes.

2.7 Vehicle Stability Control with Different Actuators

Heretofore, the vehicle stabilization is discussed from different perspectives. Some optimal control algorithms such as the MPC and HCC that can be utilized to decide on the control action are propounded. In addition to the algorithm of decision making, the mechanism that is responsible for the generation of the required control action is also important. This mechanism is referred to as an actuator, and recently, three different categories as differential braking, active steering, and active torque distribution actuation systems have been introduced for vehicle stability control [62]. The general functionality of these systems can be summarized as:

- Differential braking systems: Utilizing ABS on the vehicle to apply differential braking between the right and left wheels.
- Active steering systems: Adding a correction steering to the driver's steering input.
- Active torque distribution systems: Applying the required torque at each wheel through torque distribution devices such as electric motors or limited slip differentials.

2.7.1 Vehicle Stability Control via Differential Braking

Among all stability control actuators, differential braking has received the most attention from researchers and the automotive industry in recent years. Some research works in this field are established on one wheel control due to its simplicity, and some others consider all four wheels and solve an optimization problem. In these systems, the ABS on the vehicle is utilized to apply differential negative torque between the right and left wheels in order to generate the required yaw moment as well as wheel slip control in some minor cases. Differential negative torque is generated by increasing the brake pressure at one side compared to the other side, typically by means of hydraulic modulators. The sensor set used by a differential braking system usually consists of four-wheel speeds, yaw rate, steering angle, accelerometer, and brake pressure sensors.

Corno et al. used a rear active differential braking system with a Linear Parametric Varying (LPV) robust yaw control algorithm to propose a cost-effective approach for an active control of lateral dynamics of a four-wheel vehicle during braking [63]. In this study, the effect of load transfer is taken into account despite many studies that focused on lateral and yaw dynamics by neglecting change in the borne load. The vehicle model and simulation results were verified with experimental results.

Zhao et al. studied a brake-by-wire differential braking system with a fuzzy logic-based yaw control algorithm for vehicle stabilization [64]. A nonlinear vehicle model was presented, and wheel dynamics were incorporated with lateral dynamics. The resultant yaw rate with this approach was shown to be always within reasonable range of tire reserve, and it was assumed that the driver could respond to the yaw rate disturbances quick enough to avoid instability.

Bera et al. investigated integrated vehicle stability control with an ABS using an on–off control strategy [65]. They designed a general ABS control scheme to maintain the tire slip ratios within the desired range. The reconfigurable model of the vehicle and the braking system with variable parameters served a prototyping and design platform.

Anwar studied a brake-by-wire system using a Generalized Predictive Control (GPC) to predict the future yaw rate and use control actions to minimize the yaw rate error [66]. The employed tire model is a simple linear model without tire saturation consideration. The effectiveness of the proposed control algorithm and actuation system is evaluated experimentally in oversteer/understeer conditions in mild maneuvers on packed snow.

2.7.2 Vehicle Stability Control via Active Steering

Although only using the braking system leaves the steering system intact, some researchers show that the joint use of the braking and steering systems highly improve the lateral performance and vehicle stability [67, 68].

Tjønnås and Johansen used active steering and adaptive braking systems with Lyapunov based control allocation algorithm for vehicle stabilization [69]. In this research, the control structure is designed in three levels: high, intermediate, and low. The high-level module was responsible for desired yaw rate generation. Then, the desired slip and adjusting steering angle command were generated in the intermediate-level. Finally, the longitudinal slip control and maximal tire-road friction estimation with a desirable distribution of control forces while satisfying actuator constraints were followed out in the low-level module. The proposed control structure can be employed for over-actuated mechanical systems that need high reliability and low production cost.

Poussot-Vassal et al. studied vehicular yaw rate and lateral stability control through active steering and braking systems with the synthesis of an again-scheduled controller [70]. The control methodology was established mainly on a differential braking control method, and the active steering was only considered if the braking system exceeded its limits. Control objectives were achieved in an LPV framework by providing a solution to the LMI problem.

Competency and robustness of the controller were tested in simulations with a high fidelity full vehicle model in relatively severe driving scenarios.

Burgio and Zegelaar utilized state a feedback linearization technique to design integrated vehicle stability control with active steering and braking systems [71]. Despite, the aforementioned research, the error compensation was fulfilled mainly by steering correction, and braking correction only took place necessary. A globally smooth and stable vehicle response was achieved in an experiment. Some other research works are also investigated the incorporation of active steering and differential braking actuators to maintain and enhance vehicle stability and performance such as in [72-74].

2.7.3 Vehicle Stability Control via Active Torque Distribution

Although joint use of the braking and steering systems highly improve the lateral performance and safety control in many aspects, the functionality of such an active stability control system may has some drawbacks. Active braking systems reduce the vehicle speed

drastically such that the vehicle stability can be taken under control. Consequently, it may conflict with the driver's command during acceleration scenarios. Active steering systems also may not be useful in some driving scenarios. In the case of tire saturation, further increasing the wheel slip angle does not generate additional lateral force, and usually, steering systems are constrained to a few amounts of adjustability [68]. In order to improve the functionality of a control system actuator wise and reduce energy waste, active torque distribution systems can be replaced by two other actuation methods. Active torque distribution systems usually distribute the required torque among the wheels via electric motors in Electric Vehicles (EVs) and active differentials in conventional vehicles.

Many other research works were executed to investigate the performance of active electric motors such as [75-77], where all demonstrated a satisfactory performance in providing the required torque adjustments on vehicle corners.

Sawase and Sano developed a torque transfer mechanism with a light-weight compact structure that minimizes energy loss and provides the ability to freely control the torque difference between left and right wheels [78]. The torque transfer mechanism allows more control under extreme situations and improves cornering capabilities without interfering with the enjoyment of driving.

Annicchiarico et al. designed a semi-active differential to improve vehicle stability [79]. In this study, a purpose-built differential with particular technical features such as yaw and wheel spin controls were presented. Some simulation results were shown to compare the vehicle response with the proposed mechanism to a conventional passive locking differential.

Deur et al. worked on the development of a generalized mathematical model of an active differential dynamics using a bond graph modeling technique [80]. Different levels of model complexity were considered for an auto Limited Slip Differentials (LSD) with single clutch mechanisms. Generally, the major advantage of LSD in comparison with conventional open differentials is the restriction of the independency between the wheels on an axle. In the open differentials, the engine torque is transmitted to a planetary gear set via drive shaft, and it is distributed between the right and left wheels. However, in limited slip differentials, the engine power follows the path of the least resistance. The independency design between the axle wheels can be achieved with a number of mechanical, electrical, and hydraulic systems [81]. In addition, some patents and technical

reports have been found such as [78, 82] that were oriented to achieving outstanding differential design features for active torque distribution.

According to the above discussion, any actuation system may have different modelling features and limitations that can affect the resultant control action. In order to consider the impact of actuation dynamics, a mathematical description of it should be considered in the proposed control structure while employing constrained optimization techniques for limit satisfaction. An integrated vehicle chassis and wheel slip optimal stability controller that can be configured to work with a variety of actuators and drivetrain designs is unparalleled in literature. The proposed sub-optimal control structure in this thesis allows for the integration of chassis and wheel slip control as well as re-configurability.

2.8 Summary

This chapter reviewed the literature of vehicle stability control with a focus on papers that investigated stability control through different actuation systems on electric and conventional vehicles as well as constrained optimal control strategies for the best feasible solution provision. It was discussed that enabling the vehicle to show a desired dynamic response can be performed using reference tracking or safe region methods. In the former, a reference dynamic response is defined based on a vehicle model and driver requests. The controller compensates for the discrepancies between actual and reference states at all times. However, in the latter, the controller is only activated once the vehicle response is out of stable boundaries. In this thesis, the first approach is utilized since the persistent mode change of the controller from activation to deactivation (vice versa) is considered an unfavorable task. Moreover, a minimal control intervention may be required if the reference state is defined properly within stable boundaries. Vehicle stability control was investigated from a different actuator type perspective, as one of the contributions of this thesis is to propose a control structure that can be configured to work with a variety of actuators and drivetrains. According to the control design objectives, model predictive control and holistic corner control techniques were studied vastly for a constrained optimal control design scheme. The former technique was studied with nonlinear, hybrid, and linear prediction models. In this thesis, a nonlinear prediction model, which is linearized successively around the vehicle operation point, is utilized to avoid the NMPC and its computational complexities. This leads to a Quadratic Programming (QP) problem that can be easily managed for real-time implementation with available computational devices. The latter technique also provides a constrained optimal solution with a center to corner based

control algorithm. In this technique, the vehicle stability can be analyzed at vehicle CG, and instability is prevented by control adjustments at corners. Since a mapping from the vehicle CG to corners would be required, an optimal allocation can be accomplished at the corners based on a model based CG error detection.

Furthermore, it was mentioned that in literature, for simplicity purposes, traction control (longitudinal stability control) is usually considered to be a separate module that sacrifices a portion of control adjustment optimality, and only few research works considered combined longitudinal and lateral vehicle stabilities. In this thesis, yaw rate and sideslip as indicators of lateral stability control and tire slip ratio as an indicator of longitudinal vehicle stability are considered in the vehicle stability control problem.

Another objective of this thesis is not only to design a controller that considers actuation limitations, but also to provide a control structure that facilitates switching from one actuation to another or could work with more than one actuator as well different drivetrain schemes. To augment such a requirement, a modular control structure can be considered. As a general concept, if a CG based error analysis regardless of available actuator is accomplished in the high-level control module and the low-level module optimally distributes control adjustments between vehicle corners such that CG error is minimized, this objective could be achieved.

Chapter 3

Background

3.1 Introduction

The background materials for the proposed control method are discussed in this chapter. First, the model predictive control algorithm that is employed in the high-level module (see Fig 1.1) is reviewed. An LPV prediction model is utilized to represent the mathematical description of a general dynamic system. Using the batch approach, an optimal solution scheme for a constrained MPC optimization problem is provided. The general optimization objectives are reference tracking with minimal control effort. Then, an optimal solution is provided to address MPC optimization with an additional range of constraints on the control effort. According to the modular control structure shown in Chapter 1, a corner based control allocation using CG error analysis for vehicle stability control is presented. A holistic corner control approach is studied with a single-step optimization process at each sampling time, and this is considered as the fundamental algorithm of the low-level distribution module in the proposed control structure.

3.2 Model Predictive Control Theory

The general control scheme of the MPC is shown in Fig 3.1. An observer utilizes knowledge of the plant inputs ϑ and measurements y to arrive at a state estimate ξ. The optimization process aims to find the optimal control input sequence in order to minimize the error between the estimated state and its reference signal not only in the current sampling time, but also in the future. In order to anticipate the system's future behavior, starting from the estimated/measured state ξ, one can employ the dynamic model of the system as a prediction model and utilize previous control inputs to predict the dynamic behavior of the system over a finite prediction time horizon N_p where the manipulated inputs are changed over a finite control time horizon N_c.

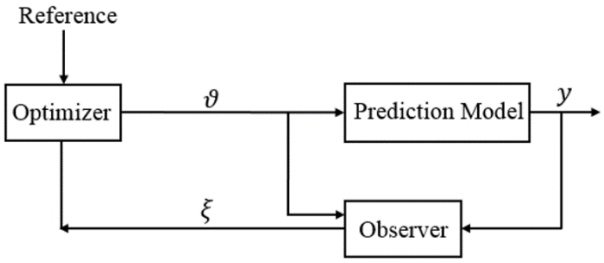

Fig 3.1 MPC general control scheme

The task of the optimizer shown in Fig 3.1 is to compute the present and future manipulated inputs $\vartheta(k), \dots, \vartheta(k + N_c - 1)$ such that the predicted outputs follow the reference states in a desirable manner while considering state and control input constraints (finite time horizon constrained MPC problem). Fig 3.2 visualizes the concept of reference tracking with MPC interventions.

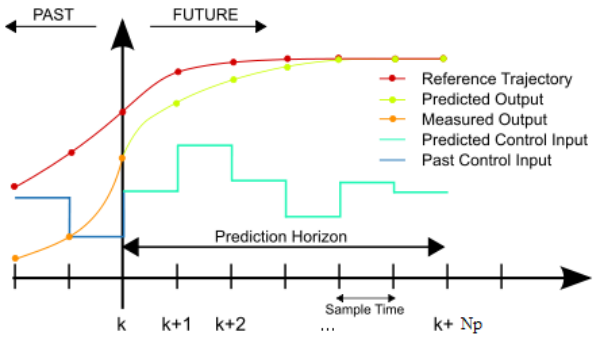

Fig 3.2 Schematic of MPC Optimization Problem [83]

3.2.1 MPC Formulation for Linear Time Variant (LTV) Systems

In order to investigate the general formulation of the LTV-MPC, a general form of a linear time varying dynamic model is considered:

$$\dot{\xi} = A\,\xi + B\,\vartheta + C \tag{3.1}$$

where, $\xi \in \mathcal{R}^n$ and $\vartheta \in \mathcal{R}^m$ are the state variable and control input signals, respectively. Also, A, B, and C are the continuous time dependent system, control, and known disturbance matrices at time t, respectively. Discretization of the prediction model at sampling time t will result in:

$$\xi_{t+1} = \bar{A}\xi_t + \bar{B}\vartheta_t + \bar{C} \tag{3.2}$$

where, $\bar{A}$, $\bar{B}$, and $\bar{C}$ are the discretized system, control, and known disturbance matrices at time step *t*. The system in Eq. (3.2) can represent a prediction model over the prediction time horizon $N_p \in Z^+$. If the optimization goal was set to minimize the error between the actual and desired state ξ and ξ_{des}, then the following quadratic cost function J_{MPC} can be defined over a finite time horizon as:

$$J^*_{MPC} = \min_{V(t)} \sum_{k=1}^{k=N_p} \left\| \xi_{t+k|t} - \xi_{des_{t+k|t}} \right\|^2_L + \sum_{k=0}^{k=N_c-1} \left\| \vartheta_{t+k|t} \right\|^2_R \quad (3.3a)$$

$$s.t. \qquad \xi_{k+1|t} = \bar{A}\xi_{k|t} + \bar{B}\vartheta_{k|t} + \bar{C} \quad (3.3b)$$

$$\xi_{k|t} \quad \in X \quad k = t+1, \dots t+N_p \quad (3.3c)$$

$$\vartheta_{k|t} \quad \in V \quad k = t+1, \dots t+N_c-1 \quad (3.3d)$$

where, *L* and *R* are the state tracking error and control effort weight matrices of appropriate dimensions, respectively. In Eq. (3.3), it is assumed that the weight matrices *L* and *R* are positive semi-definite ($L = L^T \geq 0$) and positive definite ($R = R^T > 0$) matrices, respectively. In addition, $\xi_{t+k|t}$ is the predicted state trajectory at time step $t+k$ adopted by applying the control sequence $\vartheta_t, \vartheta_{t+1}, \dots, \vartheta_{t+N_c-1}$ to the system defined in Eq. (3.2), starting from the initial state ξ_t, with prediction horizon of N_p. The state and control input constraints are defined with *X* and *V* symbols, respectively. According to MPC theory, at each time step, once the solution to optimization Eq. (3.3) is found, the first sample of the control input sequence is applied to the system and the rest are discarded. In the next time step, the optimization process is repeated for the updated measurements/estimations of the system states.

3.2.2 Solution to LTV-MPC Optimization Tracking Problem

Two approaches can be employed to solve the problem described in Eq. (3.3); the first one is a recursive approach, and the second one is a batch approach that has been utilized in this thesis. Assume that the control and prediction horizons are about the same length equal to N. According to this approach, all the future steps of states ξ_{t+1}, $\xi_{t+2} \dots, \xi_{t+N}$ are written based on the control inputs $\vartheta_t, \vartheta_{t+1}, \dots, \vartheta_{t+N-1}$ and initial states ξ_t . In fact, the intermediate states are eliminated due to successive substitution of previous states and

control inputs up until initial state. The predicted states Ω using the batch approach can be presented as [18]:

$$\Omega = \begin{bmatrix} I \\ A \\ A^2 \\ \vdots \\ A^N \end{bmatrix} \xi_t + \begin{bmatrix} 0 & \dots & \dots & 0 \\ B & 0 & \dots & 0 \\ AB & \ddots & \ddots & \vdots \\ \vdots & \ddots & \ddots & \vdots \\ A^{N-1}B & \dots & \dots & B \end{bmatrix} \Theta + \begin{bmatrix} 0 \\ I \\ A \\ \vdots \\ A^{N-1} \end{bmatrix} C_t \tag{3.4a}$$

where, $\Theta = \{\vartheta_t, \vartheta_{t+1}, \dots, \vartheta_{t+N-1}\}^T$ (3.4b)

With the proper definition of S^{ξ} and S^{ϑ}, Eq. (3.4) can be rewritten in the following form:

$$\Omega = S^{\xi}\xi_t + S^{\vartheta}\Theta + S^{c}C_t \tag{3.5a}$$

where, (3.5b)

$$S^{\xi} = \begin{bmatrix} I \\ A \\ A^2 \\ \vdots \\ A^N \end{bmatrix}, \; S^{\vartheta} = \begin{bmatrix} 0 & \dots & \dots & 0 \\ B & 0 & \dots & 0 \\ AB & \ddots & \ddots & \vdots \\ \vdots & \ddots & \ddots & \vdots \\ A^{N-1}B & \dots & \dots & B \end{bmatrix}, \text{ and}$$

$$S^{c} = \begin{bmatrix} 0 \\ I \\ A \\ \vdots \\ A^{N-1} \end{bmatrix}$$

As can be seen, all the future states in Ω are explicit functions of the present state ξ_t and the future inputs $\vartheta_t, \vartheta_{t+1}, \dots, \vartheta_{t+N-1}$. The desired state variables over the prediction control horizon can be considered as:

$$\Omega_{des} = \{\xi_t, \xi_{t+1}, \dots, \xi_{t+N}\}^T_{des} \tag{3.6}$$

Using the same notation, the tracking problem optimization cost function can be defined as:

$$J_{MPC} = (\Omega - \Omega_{des})^T \bar{L} (\Omega - \Omega_{des}) + \Theta^T \bar{R} \Theta \tag{3.7a}$$

where, (3.7b)

$$\bar{L} = diag(L)\,, \bar{R} = diag(R)$$

Substituting Eq. (3.5) in to Eq. (3.7) yields:

$$J_{MPC} = \Theta^T \left(S^{\vartheta^T} \bar{L} S^{\vartheta} + \bar{R}\right) \Theta + 2{\xi_t}^T S^{\xi^T} \bar{L} S^{\vartheta} \Theta + 2{C_t}^T S^{c^T} \bar{L} S^{\vartheta} \Theta - 2{\Omega_{des}}^T \bar{L} S^{\vartheta} \Theta + {\xi_t}^T S^{\xi^T} \bar{L} S^{\xi} \xi_t + 2{\xi_t}^T S^{\xi^T} \bar{L} S^c C_t + {C_t}^T S^{c^T} \bar{L} S^c C_t - 2{\Omega_{des}}^T \bar{L} S^c C_t - 2{\Omega_{des}}^T \bar{L} S^{\xi} \xi_t + {\Omega_{des}}^T \bar{L} \Omega_{des} \quad (3.8)$$

With the following definition of H , F, and Y, Eq. (3.8) can be written in a compact form as:

$$J_{MPC} = \Theta^T H \Theta + 2F\Theta + Y \quad (3.9a)$$

where, (3.9b)

$$H = S^{\vartheta^T} \bar{L} S^{\vartheta} + \bar{R}$$

$$F = {\xi_t}^T S^{\xi^T} \bar{L} S^{\vartheta} + S^{c^T} {C_t}^T \bar{L} S^{\vartheta} - {\Omega_{des}}^T \bar{L} S^{\vartheta} \quad (3.9c)$$

$$Y = {\xi_t}^T S^{\xi^T} \bar{L} S^{\xi} \xi_t + 2{\xi_t}^T S^{\xi^T} \bar{L} S^c C_t + {C_t}^T S^{c^T} \bar{L} S^c C_t - 2{\Omega_{des}}^T \bar{L} S^c C_t - 2{\Omega_{des}}^T \bar{L} S^{\xi} \xi_t + {\Omega_{des}}^T \bar{L} \Omega_{des} \quad (3.9d)$$

It should be noted that if $\bar{R}$ is a positive definite matrix, then J_{MPC} is a positive definite quadratic function of Θ. Then, the optimal solution to Eq. (3.9) can be obtained as:

$$\Theta^* = -H^{-1} F^T \quad (3.10)$$

where, Θ^* is the solution to the optimization problem constrained to the system dynamic model.

3.2.3 Analytical Solution to MPC Optimization Constrained to Input Bandwidth

In this section, an analytical solution to a specific case of MPC constrained optimization control problem is provided. Assume that in addition to the dynamic system constraint, there is a range constraint on the control input in the optimization problem, and it is presented with constant lower and upper bounds. Using the transformation below:

$$\bar{\Theta} = \Theta + 2H^{-1} F \quad (3.11)$$

where $\Theta \in [lb,\ ub]$

It should be notified that lb and ub are lower and upper bounds for the control sequence. Eq. (3.9a) can be rewritten as:

$$\min_{\bar{\Theta}} J_{MPC} = \bar{\Theta}^T H \bar{\Theta} \tag{3.12}$$

$$s.t. \quad \bar{\Theta} \in [\widehat{lb},\ \widehat{ub}]$$

where, $\widehat{lb}$ and $\widehat{ub}$ are lower and upper bounds of the transformed control sequence. Using the Lagrangian function, one can convert the optimization problem in Eq. (3.12) to:

$$L(\bar{\Theta}, L_1, L_2) = \bar{\Theta}^T H \bar{\Theta} + L_1\left(\widehat{ub} - \bar{\Theta}\right) + L_2(\bar{\Theta} - \widehat{lb}) \tag{3.13}$$

where, L_1 and L_2 are Lagrangian multipliers corresponding to the upper and lower control input bounds. According to Karush–Kuhn–Tucker (KKT) conditions, the following equations hold:

$$\bar{\Theta}^T H \bar{\Theta} + L_1\left(\widehat{ub} - \bar{\Theta}\right) + L_2\left(\bar{\Theta} - \widehat{lb}\right) = 0 \tag{3.14a}$$

$$L_1\left(\widehat{ub} - \bar{\Theta}\right) = 0 \tag{3.14b}$$

$$L_2\left(\bar{\Theta} - \widehat{lb}\right) = 0 \tag{3.14c}$$

$$\widehat{ub} - \bar{\Theta} \geq 0\ , \bar{\Theta} - \widehat{lb} \leq 0 \tag{3.14d}$$

In order to find the analytical solution, all combinations of the above cases must be studied:

I. Scenario of KKT conditions:

$$\bar{\Theta}^T H \bar{\Theta} + L_1\left(\widehat{ub} - \bar{\Theta}\right) + L_2\left(\bar{\Theta} - \widehat{lb}\right) = 0 \tag{3.15a}$$

$$\widehat{ub} - \bar{\Theta} = 0 \tag{3.15b}$$

$$L_1 \geq 0 \tag{3.15c}$$

Therefore,

$$\bar{\Theta}^* = \widehat{ub}, \quad \Theta^* = \widehat{ub} - 2H^{-1}F = ub + 2H^{-1}F - 2H^{-1}F = ub \tag{3.16a}$$

II. Scenario of KKT conditions:

$$\bar{\Theta}^T H \bar{\Theta} + L_1\left(\widehat{ub} - \bar{\Theta}\right) + L_2\left(\bar{\Theta} - \widehat{lb}\right) = 0 \tag{3.17a}$$

$$\widehat{lb} - \bar{\Theta} = 0 \tag{3.17b}$$

$$L_2 \leq 0 \tag{3.17c}$$

Therefore,

$$\bar{\Theta}^* = \widehat{lb}, \Theta^* = \widehat{lb} - 2H^{-1}F = ub + 2H^{-1}F - 2H^{-1}F = lb \tag{3.18a}$$

III. Scenario of KKT conditions:

$$\bar{\Theta}^T H\bar{\Theta} + L_1\left(\widehat{ub} - \bar{\Theta}\right) + L_2\left(\bar{\Theta} - \widehat{lb}\right) = 0 \tag{3.19a}$$

$$\widehat{ub} - \bar{\Theta} \geq 0, \bar{\Theta} - \widehat{lb} \leq 0 \tag{3.19b}$$

$$L_1 = 0, L_2 = 0 \tag{3.19c}$$

Therefore,

$$\bar{\Theta}^* = 0, \Theta^* = -2H^{-1}F \tag{3.20}$$

IV. Scenario of KKT conditions:

$$\bar{\Theta}^T H\bar{\Theta} + L_1\left(\widehat{ub} - \bar{\Theta}\right) + L_2\left(\bar{\Theta} - \widehat{lb}\right) = 0 \tag{3.19a}$$

$$\widehat{ub} - \bar{\Theta} \geq 0, \bar{\Theta} - \widehat{lb} \leq 0 \tag{3.19b}$$

$$L_1 \neq 0, L_2 \neq 0 \tag{3.19c}$$

Therefore, no feasible solution can be provided for Eq. (3.19). In Eqs. (3.12-3.20), $\bar{\Theta}^*$ and Θ^* are optimal transformed and actual control inputs of Eq. (3.12), respectively. According to the discussed cases, the analytical solution can be written as:

$$\Theta^* = \min(\max((-2H^{-1}F\,, lb), ub) \tag{3.21}$$

From Eq. (3.21), it can be concluded that if the control input of the MPC optimization problem is constrained to a particular range of operation, an analytical solution can be provided based the Lagrangian function method.

3.2.4 Vehicle Stability Control using CG Horizontal Forces and Yaw Moment Analysis

In order to design a control structure that is compatible with different vehicle configurations (any sort of actuation systems such as electric motor, differential braking, and active steering as well as any drivetrain layout) a general control structure can be proposed. In this control structure, deviation of the vehicle's actual dynamic states from the desired values can be correlated to CG horizontal forces and yaw moment errors. Therefore, a vehicle CG based error analysis can be conducted on the vehicle regardless of vehicle configuration, and this information can be used to generate the required control

action through the available actuation system. For validation purposes of stability analysis based on CG horizontal forces and yaw moment errors, the vehicle CG dynamics can be written as:

$$F_{X_{CG}} = \sum_{i=f,r} \sum_{j=r,l} (F_{x_{i,j}} \cos\theta_i - F_{y_{i,j}} \sin\theta_i) \tag{3.22a}$$

$$F_{Y_{CG}} = \sum_{i=f,r} \sum_{j=r,l} (F_{x_{i,j}} \sin\theta_i + F_{y_{i,j}} \cos\theta_i) \tag{3.22b}$$

$$\begin{aligned} G_{Z_{CG}} = {} & L_f \sum_{i=f} \sum_{j=r,l} (F_{x_{i,j}} \sin\theta_i + F_{y_{i,j}} \cos\theta_i) \\ & - L_r \sum_{i=r} \sum_{j=r,l} (F_{x_{i,j}} \sin\theta_i + F_{y_{i,j}} \cos\theta_i) \\ & + L_w \sum_{i=f,r} \sum_{j=r} (F_{x_{i,j}} \cos\theta_i - F_{y_{i,j}} \sin\theta_i) \\ & - L_w \sum_{i=f,r} \sum_{j=l} (F_{x_{i,j}} \cos\theta_i - F_{y_{i,j}} \sin\theta_i) \end{aligned} \tag{3.22c}$$

where, $F_{X_{CG}}$, $F_{Y_{CG}}$, and $G_{Z_{CG}}$are CG longitudinal, lateral, and yaw moment of the vehicle. $F_{x_{i,j}}$ and $F_{y_{i,j}}$ are tire ij[th] longitudinal and lateral forces, and θ_i is road steering angle at the i[th] axle. In the above equation, $i = f, r$ demonstrates front and rear axles, and $j = r, l$ demonstrates right and left sides, respectively. Additionally, L_f, L_r, and L_w stand for the distance between the front axle to the CG, the distance between the rear axle to the CG, and half of the vehicle wheel track. The dependency on the CG longitudinal and lateral force and yaw moment to corner forces can be shown by explicit reformation of Eq. (3.22) as:

$$F_{X_{CG}} = F_{X_{CG}}(\mathcal{F}) \tag{3.22a}$$

$$F_{Y_{CG}} = F_{Y_{CG}}(\mathcal{F}) \tag{3.22b}$$

$$G_{Z_{CG}} = G_{Z_{CG}}(\mathcal{F}) \tag{3.22c}$$

where,

$$\mathcal{F} = \left\{F_{x_{fl}}, F_{y_{fl}}, F_{x_{fr}}, F_{y_{fr}}, F_{x_{rl}}, F_{y_{rl}}, F_{x_{rr}}, F_{y_{rr}}\right\} \tag{3.23}$$

Using Eq. (3.22) and (3.23), dependency on the CG horizontal forces and yaw moment to tire forces can be shown with a single equation using Jacobian matrix $A_{\mathcal{F}}$ as:

$$\begin{Bmatrix} F_{X_{CG}} \\ F_{Y_{CG}} \\ G_{Z_{CG}} \end{Bmatrix} = A_{\mathcal{F}}\mathcal{F} \tag{3.24}$$

where, Jacobian matrix $A_{\mathcal{F}}$ can be defined as:

$$A_{\mathcal{F}} = \begin{bmatrix} \frac{\partial F_{X_{CG}}}{\partial F_{x_{fl}}} & \frac{\partial F_{X_{CG}}}{\partial F_{y_{fl}}} & \frac{\partial F_{X_{CG}}}{\partial F_{x_{fr}}} & \frac{\partial F_{X_{CG}}}{\partial F_{y_{fr}}} & \frac{\partial F_{X_{CG}}}{\partial F_{x_{rl}}} & \frac{\partial F_{X_{CG}}}{\partial F_{y_{rl}}} & \frac{\partial F_{X_{CG}}}{\partial F_{x_{rr}}} & \frac{\partial F_{X_{CG}}}{\partial F_{y_{rr}}} \\ \frac{\partial F_{Y_{CG}}}{\partial F_{x_{fl}}} & \frac{\partial F_{Y_{CG}}}{\partial F_{y_{fl}}} & \frac{\partial F_{Y_{CG}}}{\partial F_{x_{fr}}} & \frac{\partial F_{Y_{CG}}}{\partial F_{y_{fr}}} & \frac{\partial F_{Y_{CG}}}{\partial F_{x_{rl}}} & \frac{\partial F_{Y_{CG}}}{\partial F_{y_{rl}}} & \frac{\partial F_{Y_{CG}}}{\partial F_{x_{rr}}} & \frac{\partial F_{Y_{CG}}}{\partial F_{y_{rr}}} \\ \frac{\partial G_{Z_{CG}}}{\partial F_{x_{fl}}} & \frac{\partial G_{Z_{CG}}}{\partial F_{y_{fl}}} & \frac{\partial G_{Z_{CG}}}{\partial F_{x_{fr}}} & \frac{\partial G_{Z_{CG}}}{\partial F_{y_{fr}}} & \frac{\partial G_{Z_{CG}}}{\partial F_{x_{rl}}} & \frac{\partial G_{Z_{CG}}}{\partial F_{y_{rl}}} & \frac{\partial G_{Z_{CG}}}{\partial F_{x_{rr}}} & \frac{\partial G_{Z_{CG}}}{\partial F_{y_{rr}}} \end{bmatrix} \tag{3.25}$$

$$= \begin{bmatrix} \frac{\partial F_{X_{CG}}}{\partial \mathcal{F}} \\ \frac{\partial F_{Y_{CG}}}{\partial \mathcal{F}} \\ \frac{\partial G_{Z_{CG}}}{\partial \mathcal{F}} \end{bmatrix}$$

According to Eq. (3.25), the Jacobian matrix associates with the vehicle road steering and geometrical properties and describes how the corner forces can be mapped to the vehicle CG. The elements of this matrix can be derived using Eq. (3.22) and (3.25) as:

$$A_{\mathcal{F}} = \tag{3.26}$$

$$\begin{bmatrix} \cos\theta_f & \cos\theta_f \\ \sin\theta_f & \sin\theta_f \\ -L_w\cos\theta_f + L_f\sin\theta_f & L_w\cos\theta_f + L_f\sin\theta_f \end{bmatrix},\ldots$$

$$\begin{bmatrix} \cos\theta_r & \cos\theta_r \\ \sin\theta_r & \sin\theta_r \\ -L_w\cos\theta_r - L_r\sin\theta_r & L_w\cos\theta_r - L_r\sin\theta_r \end{bmatrix}$$

In this equation, for the purpose of simplicity, an assumption has been made that at each axle, the right and left steering angles are equal ($\theta_{fl} = \theta_{fr} = \theta_f$, and $\theta_{rl} = \theta_{rr} = \theta_r$). The direct control of the longitudinal and lateral tire forces is pragmatic using torque distribution and steering control actuation systems. Therefore, CG horizontal forces and yaw moment errors can be compensated for by controlling the corner forces using the available actuation system on the vehicle.

3.2.5 CG Forces and Yaw Moment Error Determination using MPC

As discussed, in order to design a control structure that is compatible with any vehicle configuration (any sort of actuation systems such as electric motor, differential braking, and active steering as well as any drivetrain layout); a modular control structure has been proposed. In this control structure, the high-level control module is designed based on the MPC algorithm. This control module is responsible in determining the required horizontal forces and yaw moment error detections at the vehicle CG in response to driver requests. The required CG adjustments are provided using a prediction model that is capable of anticipating vehicle response for a certain set of driver commands on a particular road surface, and then, solving a reference tracking optimization problem to minimize state error. Fig 3.3 illustrates a schematic of such a modular control structure where the high-level module is MPC based and its output sequence provides the required adjustments at vehicle CG. According to the available actuator, a low-level module is responsible for using CG horizontal forces and yaw moment error analysis for optimal control allocation between vehicle corners.

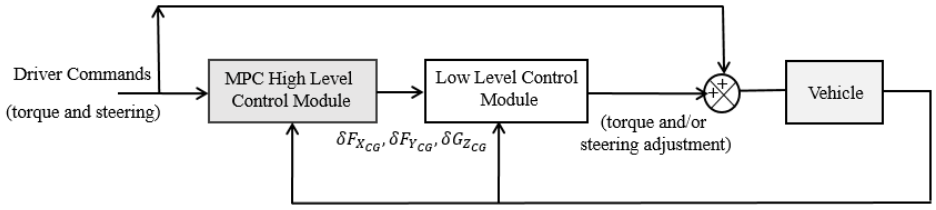

Fig 3.3 Schematic role description of MPC high-level module

3.3 Holistic Corner Control Theory

In this section, the formulation of the HCC technique, which can be used to optimally distribute torque such that CG horizontal and yaw moment errors are minimized, is discussed. According to HCC theory, if the error between the actual and desired CG horizontal forces and yaw moments is considered as:

$$E = \begin{Bmatrix} F_{X\,des} - F_X(\mathcal{F} + \delta\mathcal{F}) \\ F_{Y\,des} - F_Y(\mathcal{F} + \delta\mathcal{F}) \\ G_{Z\,des} - G_Z(\mathcal{F} + \delta\mathcal{F}) \end{Bmatrix}_{CG} \tag{3.27}$$

One can minimize E and maintain vehicle stability by adjusting $\delta\mathcal{F}$. According to the Taylor series expansion, an approximation can be estimated on the error as:

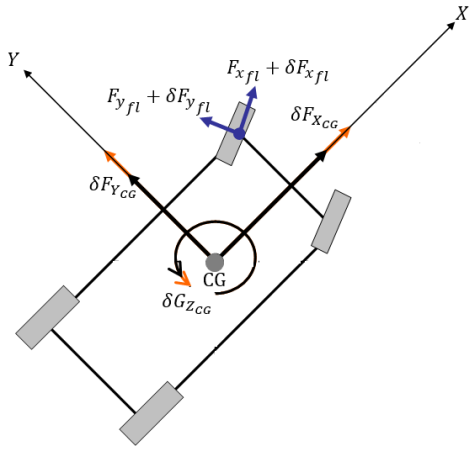

Fig 3.4 Interactions between the vehicle CG, corners forces, and moments [44]

$$F_{X_{des}} - F_X(\mathcal{F} + \delta\mathcal{F}) = F_{X_{des}} - \left\{F_X(\mathcal{F}) + \frac{dF_X(\mathcal{F} + \delta\mathcal{F})}{\partial\mathcal{F}}\delta\mathcal{F}\right\} \tag{3.28a}$$

$$F_{Y_{des}} - F_Y(\mathcal{F} + \delta\mathcal{F}) = F_{Y_{des}} - \left\{F_Y(\mathcal{F}) + \frac{dF_Y(\mathcal{F} + \delta\mathcal{F})}{\partial\mathcal{F}}\delta\mathcal{F}\right\} \tag{3.28b}$$

$$G_{Z_{des}} - G_Z(\mathcal{F} + \delta\mathcal{F}) = G_{Z_{des}} - \left\{G_Z(\mathcal{F}) + \frac{dG_Z(\mathcal{F} + \delta\mathcal{F})}{\partial\mathcal{F}}\delta\mathcal{F}\right\} \tag{3.28c}$$

The idea of controlling the vehicle corner to maintain vehicle CG stability is shown in Fig 3.4. Rewriting Eq. (3.27) using Eqs. (3.28) and (3.24) yields:

$$\begin{Bmatrix} F_{X_{des}} - F_X(\mathcal{F} + \delta\mathcal{F}) \\ F_{Y_{des}} - F_Y(\mathcal{F} + \delta\mathcal{F}) \\ G_{Z_{des}} - G_Z(\mathcal{F} + \delta\mathcal{F}) \end{Bmatrix}_{CG} = E - A_{\mathcal{F}}\delta\mathcal{F} \tag{3.29}$$

Now, in order to minimize the aforementioned CG error with minimal control effort, the following cost function is defined [44]:

$$J^*_{HCC} = \min_{d\mathcal{F}} \|E - A_{\mathcal{F}}\delta\mathcal{F}\|^2_{W_E} + \|\delta\mathcal{F}\|^2_{W_{d\mathcal{F}}} \tag{3.30}$$

$$s.t. \qquad \delta\mathcal{F}_{min} \le \delta\mathcal{F} \le \delta\mathcal{F}_{max}$$

where, $\delta\mathcal{F}_{min}$ and $\delta\mathcal{F}_{max}$ are lower and upper bounds on the control input due to physical constraints of the actuator, and W_E and $W_{d\mathcal{F}}$ are weight matrices corresponding to the CG error and control input minimizations and can be defined as below:

$$W_{d\mathcal{F}} = I \tag{3.31a}$$

$$W_E = diag(W_{F_X}, W_{F_Y}, W_{G_Z}) \tag{3.31b}$$

where, I is the identity matrix, and W_{F_X}, W_{F_Y}, and W_{G_Z} are tunable variable weights on the CG's longitudinal and lateral force, and yaw moment errors. Therefore, solving the optimization problem in Eq. (3.30) leads us to obtain $\delta\mathcal{F}$ as the required control output.

3.3.1 Solution to HCC Optimization Problem

Since the optimization problem in Eq. (3.31) provides a quadratic cost function with respect to the tire force variations $\delta\mathcal{F}$, the necessary condition of the solution is given by solving the equation:

$$\frac{\partial J_{HCC}}{\partial \delta\mathcal{F}} = 0 \tag{3.32}$$

The solution is a set of linear algebraic equations with respect to the tire force adjustments that can be represented as:

$$\delta\mathcal{F}^* = \left\{W_{d\mathcal{F}} + \left(A_{\mathcal{F}}{}^T W_E\right) A_{\mathcal{F}}\right\}^{-1} A_{\mathcal{F}}{}^T W_E E \tag{3.33}$$

3.3.2 Tire-Force Based Corner Control using HCC

As discussed in sections (3.2.4) and (3.3.5), The MPC high-level control module in the proposed control structure determines the CG's horizontal forces and yaw moment errors, and a low-level control module is required to distribute required torque adjustment between the vehicle corners or regulate driver steering such that vehicle stability is guaranteed. As HCC theory allows for corner based control and this algorithm has been utilized in the proposed control structure in this thesis. Fig 3.5 schematically illustrates the role of the HCC low-level control module.

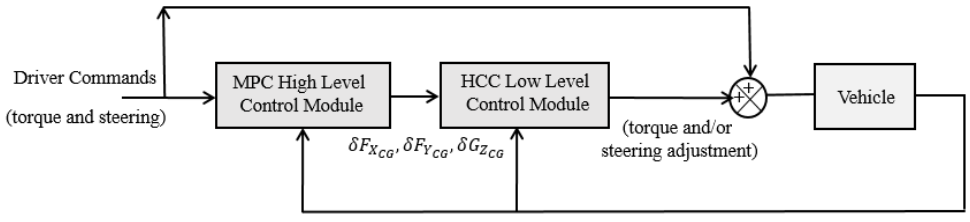

Fig 3.5 Schematic role description of HCC low-level module

Assuming that the essential actuation systems are available, in order to generate longitudinal force in the form of wheel torque adjustment and lateral force in the form of

steering angle adjustment, longitudinal force components of $\delta\mathcal{F}$ in Eq. (3.33) can be interpreted to the torque δT as:

$$\delta T_{ij} = R_e \delta F_{x_{ij}} \quad \text{for } i = \{f, r\} \text{ and } j = \{l, r\} \tag{3.34}$$

where, R_e is the effective wheel radius. And, lateral force components of $\delta\mathcal{F}$ can be interpreted to $\delta\theta$ as [6]:

$$\delta\theta_{fl} = \frac{\delta F_{y_{fl}}}{\bar{C}_{\alpha_{fl}}} + \alpha_{fl_0} + \tan^{-1}\frac{v + L_f r}{u - L_w r} - \theta_f \tag{3.35a}$$

$$\delta\theta_{fr} = \frac{\delta F_{y_{fr}}}{\bar{C}_{\alpha_{fr}}} + \alpha_{fr_0} + \tan^{-1}\frac{v + L_f r}{u + L_w r} - \theta_f \tag{3.35b}$$

$$\delta\theta_{rl} = \frac{\delta F_{y_{rl}}}{\bar{C}_{\alpha_{rl}}} + \alpha_{rl_0} + \tan^{-1}\frac{v - L_r r}{u - L_w r} - \theta_r \tag{3.35c}$$

$$\delta\theta_{rr} = \frac{\delta F_{y_{rr}}}{\bar{C}_{\alpha_{rr}}} + \alpha_{rr_0} + \tan^{-1}\frac{v - L_r r}{u - L_w r} - \theta_r \tag{3.35d}$$

where, v, u, and r are the CG lateral and longitudinal velocities, and yaw rate, respectively. Also, $\bar{C}_{\alpha_{ij}}$ is the tire cornering coefficient that can be obtained based on the tire properties, and α_{ij_0} is the tire slip at the ijth corner in a previous sampling time.

3.4 Summary

In this chapter, the basic concepts of the optimal control techniques that are used in the proposed control structure are discussed. According to the design objectives, formulations of the MPC and HCC optimal control algorithms have been presented. As mentioned, modularity of the control structure and CG based error determination in the high-level control module allows for the implementation of the controller on various vehicle configurations equipped with different actuation systems or drivetrain layouts. The design process of the MPC control algorithm that has been employed in a high-level module was illustrated. Using the MPC in a high-level control module provides an optimal model based control law. The low-level control module is HCC based and also provides optimality in control law. Soft-constraints such tire reserve can be treated with an HCC algorithm using an additional term in the cost function. As shown, the original HCC optimization is a single-step based on a model base error. This control algorithm can be developed to consider an actuation system dynamic model without a significant increase in

computational complexities since the actuation model will be only considered in the low-level control for a realistic torque distribution.

Chapter 4

Integrated Longitudinal and Lateral Vehicle Stability Control via Torque Vectoring

4.1 Introduction

In the previous chapter, the background knowledge of the control modules of the proposed structure were discussed. In this chapter, the vehicle stability control problem is studied through Torque Vectoring (TV). The integrated longitudinal and lateral stability of the vehicle can be maintained by adjusting the wheel torque with respect to driver commands by using actuation systems such as electric motors in Electric Vehicles (EVs) or Differential Braking (DB) systems in conventional and hybrid vehicles. First, the proposed control scheme with TV methodology is discussed. The role of the control modules in the proposed structure are highlighted. Second, integrated stability control with an MPC algorithm and optimal torque allocation with the HCC are formulated. Finally, simulation and experimental results are illustrated to evaluate the proposed control structure qualifications.

4.2 General Scheme of Control Structure via Torque Adjustment

The proposed control structure is illustrated schematically in Fig 4.1. As one of the major design objectives is integrated longitudinal and lateral stability control (wheel slip and vehicle chassis control), stability analysis is accomplished using indicators such as lateral velocity, yaw rate, yaw angle, and wheel slip ratios. The desired lateral dynamics (lateral velocity, yaw rate, and yaw angle) is calculated based on driver steering (θ) and torque (T) commands. A yaw rate maximization approach has been used to calculate desired optimal longitudinal dynamics (wheel slip ratios) based on an analytical combined-slip Burkhardt tire model. The control technique used in the high-level module is MPC reference state tracking. A prediction model is utilized to predict future dynamic states based on measured/estimated states and the required control adjustments which are CG longitudinal

force and yaw moment ($\delta F_{X_{CG}}$ and $\delta G_{Z_{CG}}$) over a finite control horizon. The control adjustments are outcomes of solving an MPC optimization problem that minimizes the error between the actual and target courses. At each sampling time, the first set of resultant CG longitudinal force and yaw moment adjustments are employed in the low-level control module, where optimal torque allocation (δT) is accomplished by solving a single-step HCC optimization [44]. As shown in Chapter 3, the HCC optimization cost function is defined based on the CG horizontal forces, yaw moment errors, and corner torque adjustments as control inputs. The all-wheel drive control technology allows independent control of the corner torque for stabilizing the vehicle CG. In the following section, the design procedure of each level of the proposed integrated controller is discussed.

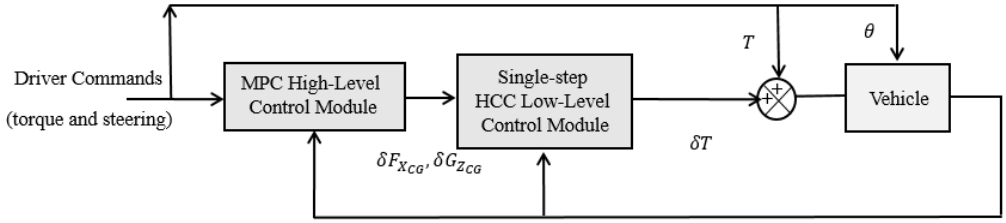

Fig 4.1 Schematic of the proposed modular control structure with torque adjustment

4.3 MPC High-Level Module Design via Torque Adjustment

In this section, first, the prediction model that has been used in the MPC high-level control module is described with consideration of both longitudinal and lateral vehicle dynamics. Then, the desired dynamics is described to form an MPC reference tracking optimization. In order to define the desired longitudinal dynamics, a yaw rate maximization method based on a combined-slip Burkhardt tire model is used. Finally, an MPC based CG error analysis (required adjustments in longitudinal force and yaw moment) is provided to solve an optimization problem.

4.3.1 MPC Prediction Model

The prediction model adopted in the MPC algorithm is a bicycle vehicle model shown in Fig 4.2. This model provides a satisfactory approximation of the vehicle dynamic response with a low computational cost and real-time implementability. According to Fig 4.2, the vehicle CG horizontal forces and yaw moment can be formulated based on corner horizontal forces and road steering as [84]:

$$F_{X_{CG}} = (F_{x_f} + \delta F_{x_f})\cos\theta - F_{y_f}\sin\theta + (F_{x_r} + \delta F_{xr}) \tag{4.1a}$$

$$F_{Y_{CG}} = F_{y_f}\cos\theta + F_{y_r} + (F_{x_f} + \delta F_{x_f})\sin\theta \tag{4.1b}$$

$$G_{Z_{CG}} = L_f F_{y_f}\cos\theta - L_r F_{y_r} + L_f F_{x_f}\sin\theta + L_f \delta F_{x_f}\sin\theta + \delta G_{z_{CG}} \tag{4.1c}$$

where,

$$F_{X_{CG}} = m(\dot{u} - vr) \tag{4.2a}$$

$$F_{Y_{CG}} = m(\dot{v} + ur) \tag{4.2b}$$

$$G_{Z_{CG}} = I_z\dot{r} \tag{4.2c}$$

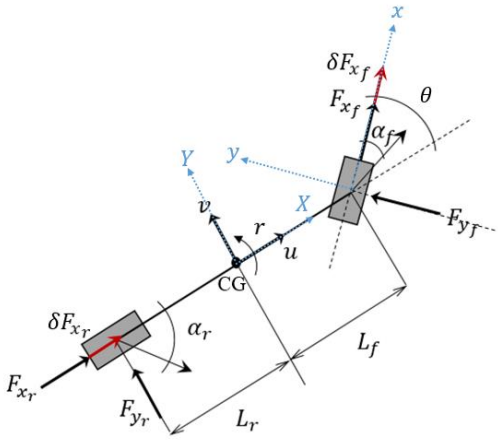

Fig 4.2 Bicycle vehicle model with control torque intervention

In the above equation, m is the vehicle mass and I_z is the vehicle inertia around its vertical axis. Also, the notations v and u refer to the vehicle CG velocities in the longitudinal and lateral directions, and r is vehicle yaw rate. The vehicle yaw angle is considered to be a state to prevent steady-state yaw rate error in the MPC prediction model:

$$\dot{\psi} = r \tag{4.3}$$

In order to get the longitudinal vehicle stability (wheel slip ratio) under control, the wheel dynamics should be considered in the MPC prediction model as:

$$J_\omega\dot{\omega}_{ij} = T_{ij} - R_e(F_{x_{ij}} + \delta F_{x_{ij}}) \quad \text{for } i = \{f, r\} \quad \text{and} \quad j = \{l, r\} \tag{4.4}$$

where, ω_{ij} is the wheel rotational (angular) velocity at the ij[th] corner. Also, J_ω and R_e are the wheel moment of inertia and effective radius, respectively. However, instead of using

the conventional wheel dynamics equation, wheel slip ratios can be employed to quantify wheel longitudinal stability. According to the physical interpretation of wheel slip ratio, stability of the wheel is violated if slip ratio exceeds a certain threshold on a specific road condition. The wheel slip ratio can be obtained in driving and braking conditions as:

$$\lambda_{ij} = 1 - u_{ij}/R_e\omega_{ij} \qquad \textit{driving condition} \qquad (4.5a)$$

$$\lambda_{ij} = 1 - R_e\omega_{ij}/u_{ij} \qquad \textit{braking condition} \qquad (4.5b)$$

Therefore, it can be concluded that:

$$\lambda_{ij} = 1 - \min(R_e\omega_{ij}, u_{ij})/\max(R_e\omega_{ij}, u_{ij}) \qquad (4.6)$$

By considering driving conditions and differentiating Eq. (4.5a):

$$\dot{\lambda_{ij}} = \frac{R_e\omega_{ij}(R_e\dot{\omega_{ij}} - \dot{u_{ij}}) - R_e\dot{\omega_{ij}}(R_e\omega_{ij} - u_{ij})}{(R_e\omega_{ij})^2} \qquad (4.7)$$

One can establish wheel dynamics equations using the wheel slip ratio and Eq. (4.7):

$$\dot{\lambda_{ij}} = \dot{\omega}_{ij}/\omega_{ij}\left(1 - \lambda_{ij}\right) - \dot{u_{ij}}/(R_e\omega_{ij}) \qquad (4.8)$$

where, $\dot{u_{ij}} = a_{x_{ij}}$. In the following notation, $a_{x_{ij}}$ is longitudinal wheel acceleration at the ijth corner and the wheel coordinate system, and it can be found as:

$$a_{x_{ij}} = a_{X_{ij}}\cos\theta_{ij} + a_{Y_{ij}}\sin\theta_{ij} \qquad (4.9)$$

while $\theta_{fl} = \theta_{fr} = \theta_f, = \theta$, and $\theta_{rl} = \theta_{fl} = \theta_r = 0$. The slip ratios of all wheels are evaluated in the high-level module, however, only maximum the slip ratio is considered in the MPC prediction model as a quantified index for longitudinal vehicle dynamics. The reasoning is that the wheel slip ratio can be defined at vehicle corners rather than at the axles. Thus, it is not compatible with the bicycle vehicle model where axle (front and rear) longitudinal force adjustments are considered for vehicle stabilization. Accordingly, it was assumed that all wheels experience the largest possible slip ratio, and the MPC prediction model is augmented with λ_{max} state equation as:

$$\dot{\lambda}_{max} = \max(\dot{\lambda}_{fl}, \dot{\lambda}_{fr}, \dot{\lambda}_{rl}, \dot{\lambda}_{rr}) \qquad (4.10)$$

Using Fig 4.2 and the above equation, Eq. (4.8) can be rewritten in the CG coordinate system as:

$$\dot{\lambda}_{max} = \max\Big(\dot{\omega}_{ij}/\omega_{ij}\left(1-\lambda_{ij}\right) - \left(a_{X_{ij}}\cos\theta_{ij} + a_{Y_{ij}}\sin\theta_{ij}\right)/R_e\omega_{ij}\Big) \tag{4.11}$$

The corner longitudinal and lateral accelerations can be obtained as:

$$a_{X_{fl}} = a_{X_{CG}} - \dot{r}L_w - r^2L_f,\ a_{Y_{fl}} = a_{Y_{CG}} + \dot{r}L_f - r^2L_w \tag{4.12a}$$

$$a_{X_{fr}} = a_{X_{CG}} + \dot{r}L_w - r^2L_f,\ \ a_{Y_{fr}} = a_{Y_{CG}} + \dot{r}L_f + r^2L_w \tag{4.12b}$$

$$a_{X_{rl}} = a_{X_{CG}} - \dot{r}L_w + r^2L_r,\ \ \ a_{Y_{rl}} = a_{Y_{CG}} - \dot{r}L_r - r^2L_w \tag{4.12c}$$

$$a_{X_{rr}} = a_{X_{CG}} + \dot{r}L_w + r^2L_r\ ,\ \ a_{Y_{rr}} = a_{Y_{CG}} - \dot{r}L_r + r^2L_w \tag{4.12d}$$

In the above equations, $a_{X_{ij}}$ and $a_{Y_{ij}}$ are wheel ij longitudinal and lateral accelerations in the CG coordinate system, respectively. According to body dynamics:

$$a_{X_{CG}} = \Big(\left(F_{x_f} + \delta F_{x_f}\right)\cos\theta_f - F_{y_f}\sin\theta_f + F_{x_r} + \delta F_{x_r}\Big)/m \tag{4.13}$$

It should be noted that using the maximum wheel slip ratio as a longitudinal stability indicator may result in a conservative control law. The integration between vehicle longitudinal and lateral dynamics can be realized by a chain of Eqs. (4.1-4.13). This chain can be described by the following compact state space model:

$$\dot{\xi} = \bar{g}(\xi_t, \vartheta_t) \tag{4.14a}$$

$$\eta = \bar{h}(\xi_t) \tag{4.14b}$$

According to Eq. (4.14), the vehicle dynamics shows a nonlinear behavior. An assumption has been made such that forward speed and driver steering command changes are negligible within a few milliseconds of the sampling-time period, and as a result, those were assumed to be constant at each optimization process. Due to this assumption, vehicle longitudinal velocity is not considered as a state variable in this thesis, and the state and input vectors are defined as:

$$\xi = \{v, r, \psi, \lambda_{max}\}^T \tag{4.15a}$$

$$\vartheta = \left\{\delta F_{x_f}, \delta F_{x_r}, \delta G_z\right\}^T \tag{4.15b}$$

Providing an LTV prediction model in the MPC facilitates the real-time implementation of the designed MPC controller and reduces the required computational cost.

A Step Invariant (SI) equivalent model [85] is used to provide a discretized model to handle possible matrix singularities. The following discretized LTV model is considered:

$$\xi_{t+1} = \bar{A}\xi_t + \bar{B}\vartheta_t + \bar{C} \tag{4.16}$$

where, $\bar{A}$, $\bar{B}$, and $\bar{C}$ are discretized system, control, and disturbance matrices at time step t. The system in Eq. (4.16) represents a prediction model over a time horizon $k = t, \ldots, t + N - 1$ where $N \in Z^+$. The lateral force is piecewise linearized around the operating point in Eq. (4.16) as:

$$F_{y_i} = F_{y_{i_0}} + \Delta F_{y_i} \qquad \text{for } i = \{f, r\} \tag{4.17a}$$

$$\Delta F_{y_i} = \bar{C}_{\alpha_i} \Delta\alpha_i \qquad \text{for } i = \{f, r\} \tag{4.17b}$$

where, $F_{y_{i_0}}$ and ΔF_{y_i} are tire lateral force estimations from the last sampling time and the predicted tire lateral force variation, respectively. In addition, $\Delta\alpha$ is the vehicle slip change that can be found as:

$$\Delta\alpha_i = \alpha_i - \alpha_{i_0} \qquad \text{for } i = \{f, r\} \tag{4.18}$$

where previous and current step vehicle slips are shown with α_0 and α. The vehicle slip calculation for the front and rear axles can be formulated as:

$$\alpha_f \approx \theta_f - \frac{v + L_f r}{u} \tag{4.19a}$$

$$\alpha_r \approx -\frac{v - L_r r}{u} \tag{4.19b}$$

By substituting Eq. (4.19) in Eq.(4.18) and using the resultant in Eq.(4.17), the tire lateral force can be written based on the vehicle lateral velocity and yaw rate states, geometry, and driver steering angle. In Eq. (4.17), $\bar{C}_\alpha$ is the tire cornering stiffness that can be calculated based on a combined slip Burkhardt tire model and particular tire properties according to the experimental setup [30]. Therefore, the estimated lateral force at each sampling time as well as possible growth of the lateral force, enables us to study the tire force in the nonlinear region shown in Fig 4.3. This calculation approach is shown in Fig. 4.3 schematically.

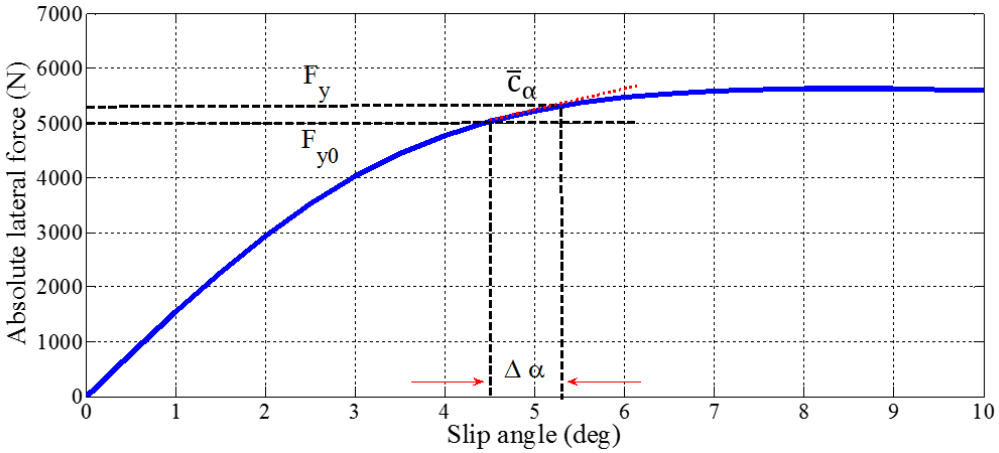

Fig 4.3 Lateral force piecewise linearization around the operating point

4.3.2 Combined Slip Burkhardt Tire Model

According to the previous section, the tire lateral force variation at each sampling time can be computed using the tire slip angle change and tire cornering coefficient as:

$$\bar{C}_{\alpha_i} = {\Delta F_{y_i}}/{\Delta \alpha_i} \qquad \text{for } i = \{f, r\} \tag{4.20}$$

In order to address combined slip situations, a combined slip tire model has to be studied that provides the tire lateral force model with respect to the vehicle slip angle. The tire model that is investigated in this study is a combined-slip Burkhardt tire model. The tire friction force in the lateral and longitudinal directions are generally dependent on the friction coefficient μ of the corresponding direction and normal wheel load F_z:

$$\mu_r = {F_{r\,brk}}/{F_z} \qquad \text{for } r = \{x, y\} \tag{4.21}$$

where, $F_{x_{brk}}$ and $F_{y_{brk}}$ are the Burkhardt model longitudinal and lateral tire forces. Burkhardt illustrates the longitudinal and lateral friction coefficients as:

$$\mu_x = \mu_{res}\, {\lambda}/{S_{res}} \tag{4.22a}$$

$$\mu_y = \mu_{res}\, {\alpha}/{S_{res}} \tag{4.22b}$$

where, μ_{res} is the resultant friction coefficient, and S_{res} is the resultant tire slip, which is directed in the same direction as the resultant friction coefficient. The resultant tire slip for each tire can be described with:

$$S_{res} = \sqrt{\alpha^2 + \lambda^2} \tag{4.23}$$

And, the resultant friction coefficient can be written as:

$$\mu_{Res} = \mu(c_1(1 - e^{-c_2 S_{Res}}) - c_3 S_{Res}) \quad (4.24)$$

where, c_1, c_2, and c_3 are the Burkhardt analytic tire model characteristic coefficients and can be found based on the tire properties in an experiment, and μ is the road-tire adhesion coefficient. According to the experimental setup, the longitudinal and lateral forces for different normal loads are shown in Fig 4.4 (a) and (b). The forces can be measured using load wheel sensors that are attached to the tires. However, the data shown in these figures belong to the pure-slip conditions. Fig 4.4 (a) is based on a lateral slip where there is no longitudinal slip in the tires, and Fig 4.4 (b) is based on a longitudinal slip where there is no lateral slip in the tires.

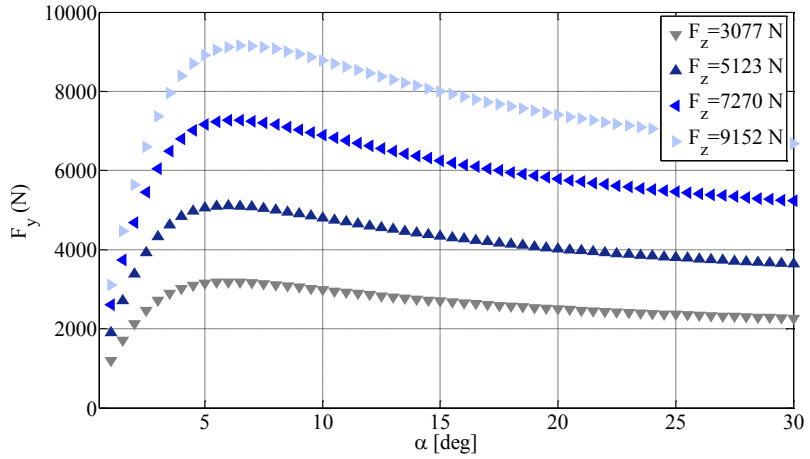

(a)

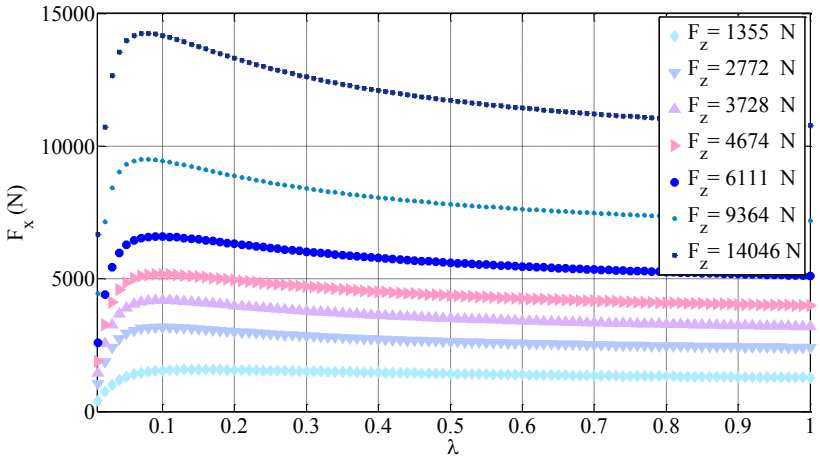

(b)

Fig 4.4 Experimental data (a) Lateral forces versus lateral slip (b) Longitudinal force versus slip ratio

The best fit to pure-slip data is found using optimization, and this is employed for a combined slip force estimation. In this method, a cost function has been considered based on the error between the experimental lateral force and the Burckhardt model lateral force as:

$$J_{Tire\ Model} = \sum_{k=1}^{4} \left\| F_{y_{brk}}(k) - F_{y_{act}}(k) \right\|_2 \tag{4.25}$$

where, $F_{y_{brk}}$ is the lateral force of the Burkhardt tire model and $F_{y_{act}}$ is the actual lateral force. The collected data for four different normal loads is shown in Fig. 4.4. For pure-lateral slip on dry road condition, one can write:

$$J_{Tire\ Model} = \sum_{k=1}^{4} \left\| F_z(k)(c_1(1 - e^{-c_2\alpha}) - c_3\alpha) - F_{y_{act}}(k) \right\|_2 \tag{4.26}$$

Solving the optimization problem in Eq. (4.26) can provide the optimal set of the tire characteristic coefficients that generates the most precise lateral tire forces. For the specific tire data that shown in Fig. 4.4., the tire coefficient can be obtained as shown in Table 4.1.

Table 4.1 Tire characteristic coefficients in an experimental setup

Tire Coefficients	Value
c_1	1.559
c_2	18.579
c_3	3.333

According to the tire characteristic coefficients shown in Table 4.1, the Burkhardt lateral tire force is compared to the actual lateral tire force data for a wide range of lateral slip, and shown in Fig. 4.5. This figure shows that the optimal tire characteristic coefficients provide a satisfactory model of lateral force in the pure-slip condition. For the combined-slip condition, where the longitudinal slip has a range of $\lambda \in [0\ 0.4]$, the Burkhardt tire model has been employed to generate a tire lateral force such that: $F_z \in [307\ 7\ \text{N}, 5123\ \text{N}, 7270\ \text{N}, 9152\ \text{N}]$. Fig. 4.6 (a-d) show the lateral force generated with the Burkhardt tire model.

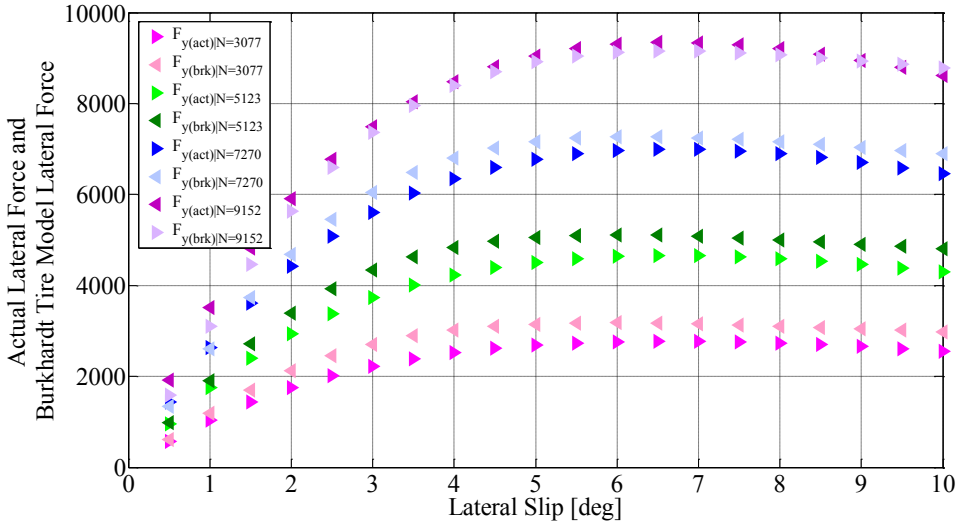

Fig 4.5 Lateral force approximation with the Burkhardt model

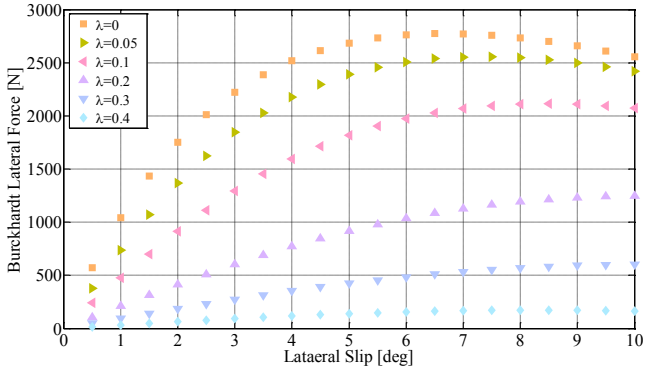

(a)

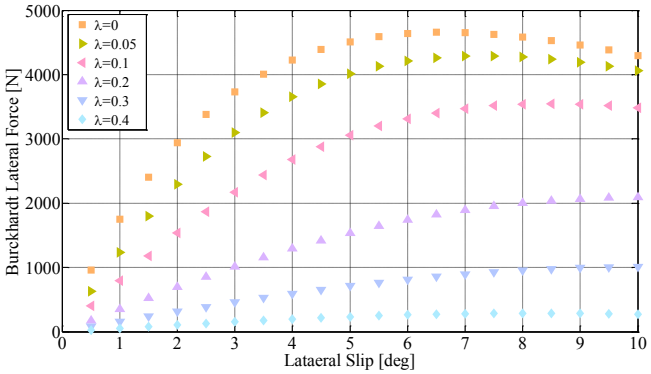

(b)

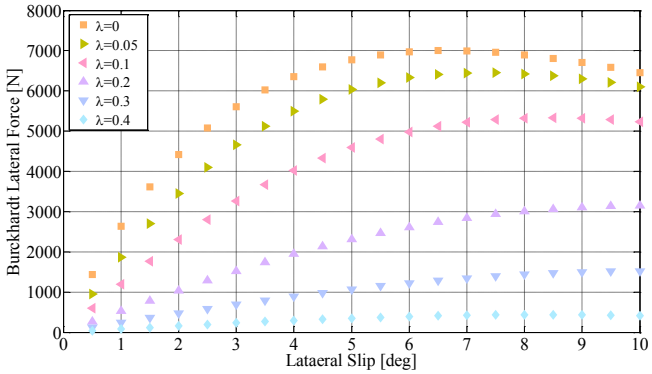

(c)

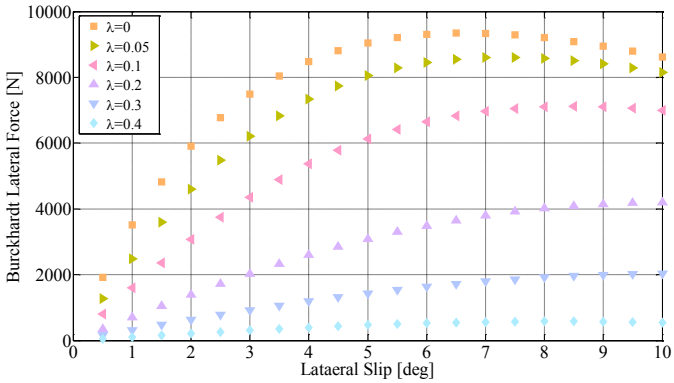

(d)

Fig 4.6 Combined-slip lateral force approximation with the Burkhardt tire model for normal load: (a) F_z = 3077 N, (b) F_z =5123 N, (c) F_z =7270 N, and (d) F_z =9152 N

In order to use the tire cornering coefficient for different sets of longitudinal and lateral slip, look-up tables have been formed, and they have been used in the online MPC optimization process in real-time. The middle points can be found using interpolation techniques.

4.3.3 Reference Vehicle Response

According to the optimization cost function that is shown in Eq. (3.3), a reference set should be defined for the MPC reference tracking problem. Using Eq. (4.15a), the vehicle dynamic states considered in this study are lateral velocity, yaw rate, yaw angle, and maximum longitudinal slip ratio. The desired lateral velocity and yaw rate of the vehicle can be defined based on the vehicle steady-state behavior on dry pavement as [6, 7]:

$$r_{des} = {u\theta_f}/{(L + K_{us}u^2)} \tag{4.27a}$$

$$v_{ydes} = r_{des}(L_r - {mL_f u^2}/{L\bar{C}_\alpha}) \tag{4.27b}$$

where K_{us} is the understeer coefficient and L is the wheelbase. In Eq. (4.27), it is assumed that the vehicle is steerable only at the front axle. Although Eq. (4.27a) provides an insight into the desired yaw rate on a dry road, this equation cannot be used for non-dry road conditions. The reason is that the tire capacity depends to the tire-road adhesion coefficient, and tire saturation occurs with less tire force on slippery road conditions. In order to take the road adhesion coefficient effects into account, the vehicle lateral acceleration is studied:

$$a_{Y_{CG}} = ur + \dot{v} \tag{4.28}$$

According to the definition of sideslip angle, the lateral velocity can be written as follows:

$$v = u \tan\beta \tag{4.29}$$

Derivation of Eq. (4.29), and substituting it in Eq. (4.28) yields:

$$a_{Y_{CG}} = ur + \dot{u} \tan\beta \, {u\dot{\beta}}/{\sqrt{1 + \tan\beta^2}} \tag{4.30}$$

The lateral acceleration on the slippery road condition has an upper limit as:

$$a_{Y_{CG}} \leq \mu g \tag{4.31}$$

where, g is the gravitational acceleration. If the vehicle sideslip angle and its derivative are both assumed to be small, the first term in Eq. (4.30) dominates, and consequently, the upper limit of the desired yaw rate can be derived as:

$$r_{des} \leq {\mu g}/{u} \tag{4.32}$$

Considering Eq. (4.27) and (4.32) yields:

$$r_{des} = \min({u\theta_f}/{(L + K_{us}u^2)}, {\mu g}/{u}) \tag{4.33}$$

It should be mentioned that ξ_{des} in Eq. (4.15a) also contains the desired yaw angle of the vehicle that can be computed based on the desired yaw rate discrete integration as:

$$\psi_{des} = \sum_{k=1}^{D} r_{des}(k)T_s \tag{4.34}$$

where, T_s is the sampling time duration and D is the size of the time window that has been studied to conclude desired yaw angle. In this thesis, a number of 200 samples of the previous desired yaw rate are reviewed. It was assumed that according to the vehicle significant inertia and test setup sampling time of five milliseconds, the heading angle of the vehicle is approximately unchanged within a second. In addition, it was assumed that the driver steering and gas/brake pedal requests would not be changed within a short sampling time duration (0.005 sec), and then the desired values of the dynamic states have been defined on the current time basis and are not modified within the control horizon.

As mentioned, controlling the wheel slip ratio is an essential component of vehicle stability control. The reason is that the longitudinal and lateral tire forces drop drastically right after wheel slip ratio exceeds a certain threshold.

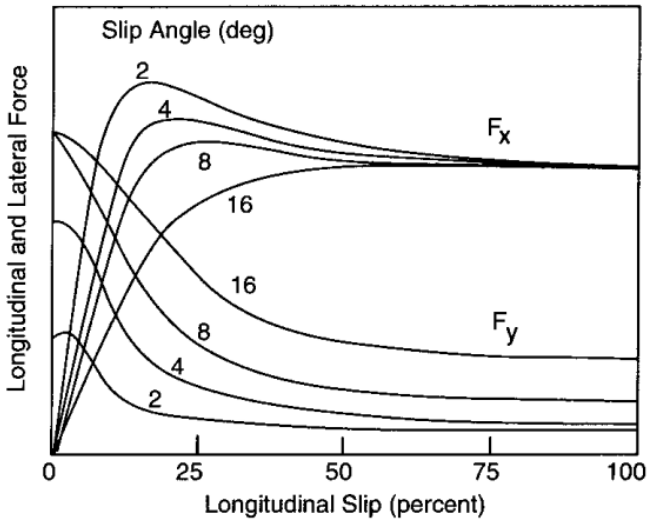

Figure 4.7 Longitudinal and lateral tire forces as a function of slip ratio [86]

Fig 4.7 shows a variation of longitudinal and lateral forces with respect to slip ratio for different slip angles. As shown, the application of the slip ratio after a certain threshold generally decreases tire lateral force capacity. If the front tires exceed this threshold, it results in poor maneuverability and an understeer condition. However, if it takes place on the rear tire, it promotes an oversteer behavior and risk of instability. Consequently, maintaining the slip ratio in a safe region can be considered a crucial task. According to the above discussion, the desired slip ratio can be defined as:

$$\lambda_{des} = \min\left(\lambda_{threshold}, \max(\lambda_{fl}, \lambda_{fr}, \lambda_{rl}, \lambda_{rr})\right) \quad (4.35)$$

where, $\lambda_{threshold}$ is the slip ratio threshold. According to the combined-slip tire models, the slip ratio threshold is a function of the lateral slip and the road condition. Fig 4.8 shows that on a dry road condition, this threshold can be considered at its maximum value and as road surface adhesion decreases, this value decreases.

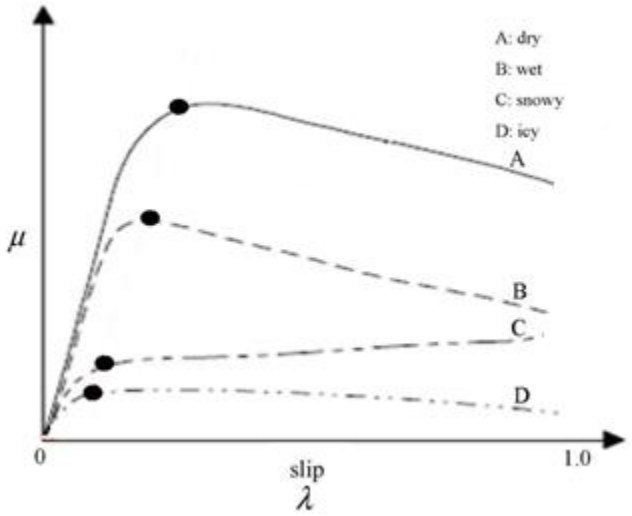

Figure 4.8 Longitudinal tire force as a function of slip ratio and road condition [87]

In order to find an optimal value for the desired slip ratio, and to address the situation where the tire capacity should be optimally devoted between lateral and longitudinal directions, a similar approach to the one presented in [53] could also be used. A desired (optimal) tire slip ratio can be considered in such a way that the yaw moment is maximized for the prime vehicle steerability, however, the maximum steerability effect was not considered in this thesis.

4.4 HCC Low-Level Optimal Torque Distributor Design via Torque Adjustment

According to the general modular control structure that is proposed and illustrated in Chapter 3, the optimal longitudinal force and yaw moment adjustments generated by the high-level MPC control module are fed in to a low-level control module for optimal torque allocation. The optimal torque allocation is accomplished based on the HCC strategy discussed in previous chapter, which considers the discrepancies between the desired and actual vehicle CG forces and yaw moment and generates a control sequence that minimizes these discrepancies. The longitudinal and lateral components of the horizontal tire forces

can be considered as a set of control sequences in the HCC distribution strategy. In this strategy, a tire model does not need to be included in the formulation since horizontal tire force adjustments are determined directly based on CG error analysis.

As discussed before, the vehicle CG forces and yaw moment are functions of horizontal tire forces. The direct control of the lateral tire forces needs an active steering actuation system. Since no active steering system is available in the following experimental test setup in this section, lateral tire forces as control inputs should be eliminated. However, the longitudinal tire force adjustment is available using electric motor equipment. According to Eq. (3.18) and (3.19), the CG horizontal force and yaw moment error vector can be shown with the following equation at the vehicle's CG coordinate system:

$$E = \left\{F_{X_{des}} - F_X(\mathcal{F}), F_{Y_{des}} - F_Y(\mathcal{F}), G_{Z_{des}} - G_Z(\mathcal{F})\right\}^T \tag{4.36}$$

Using Eq. (4.36) and Fig. (4.2), one can conclude that the error vector defined in Eq. (3.27) becomes:

$$E = \left\{\delta F_{x_f} \cos\theta_f + \delta F_{x_r}, \quad \delta F_{x_f} \sin\theta_f, \quad \delta G_z\right\}^T \tag{4.37}$$

And since MPC high-level control module computes $\vartheta = \left\{\delta F_{x_f}, \delta F_{x_r}, \delta G_z\right\}^T$, the error vector can be obtained using MPC outputs. In order to minimize the aforementioned error with minimum control effort, the cost function in Eq. (3.30) is used with the corresponding constraints on the control inputs at each vehicle corner [44]:

$$J^*_{HCC} = \min_{d\mathcal{F}} \|E - A_{\mathcal{F}}\delta\mathcal{F}\|^2_{W_E} + \|\delta\mathcal{F}\|^2_{W_{d\mathcal{F}}} \tag{4.38}$$

$$s.t. \qquad {}^{T_{lb}}/_{R_e} \leq \delta\mathcal{F} \leq {}^{T_{ub}}/_{R_e}$$

where, $\mathcal{F} = \left\{F_{x_{fl}}, F_{x_{fr}}, F_{x_{rl}}, F_{x_{rr}}\right\}^T$. Moreover, T_{lb} and T_{ub} are the lower and upper limits of the electric motor torque actuation system. The solution to the HCC optimization problem in Eq. (4.38) can be found using Eq. (3.33) in Chapter 3.

4.5 Experimental Results via Torque Adjustment

In order to show the capabilities of the proposed controller, experimental results are presented in this section. Typical benchmark driving test scenarios that are usually used by the automotive industry are investigated in this study by the proposed controller. The vehicle used for the experimental studies can be seen in Fig 4.9(a) with specifications listed in Table 4.2. The studied vehicle is an electric 4WD Chevrolet Equinox. The electric

motors used at each vehicle corner are shown in Fig 4.9 (b) where each has a torque generation limit of up to ± 1600 N.m. In addition, an ABS is available on this vehicle.

Table 4.2 Vehicle model properties

Parameter	Value
Vehicle mass	2270 kg
Distance between the front axle and C.G.	1.42033 m
Distance between the rear axle and C.G.	1.43767 m
Tire effective radius	0.351 m
Vehicle wheel track	1.6 m
Moment of inertia about Z axis	4600 kg. m^2
Vehicle understeer gradient	0.006

Capturing the vehicle system dynamics with the MPC control module requires that the control horizon be of sufficient length. However, the control horizon is not typically chosen to be large for two major reasons. First, the resultant computational burden and non- real-time implementation, and second, the non-predictable driver steering command. The simulations and experimental results that were performed during the tuning phase of the controller indicated that the control horizon and sampling time presented below produce a satisfactory prediction of the vehicle's dynamic response resulting in proper performance of the controller:

- *Control system sample time:* $T_s = 0.005$
- *Number of points in MPC control/prediction horizon:* $N = 4$

In addition, weights of MPC and HCC optimizations are shown in Table 4.3. According to Eq. (3.7), the weight matrices $\bar{L}$ and $\bar{R}$ are formed by L and R matrices defined as weights on vehicle dynamic states and control inputs in the MPC optimization problem. In this chapter, L and R can be shown as:

$$L = diag(L_v, L_r, L_\psi, L_{\lambda_{max}}) \tag{4.39a}$$

$$R = diag(R_{F_{x_f}}, R_{F_{x_r}}, R_{G_z}) \tag{4.39b}$$

Table 4.3 Tuned weights of the proposed control system via torque adjustment

High and low level control weights	Parameter	Value
Weight on lateral velocity control in MPC	L_v	5
Weight on yaw rate tracking control in MPC	L_r	120
Weight on yaw angle control in MPC	L_ψ	1000
Weight on maximum slip ration control in MPC	$L_{\lambda_{max}}$	200
Weight on front axle longitudinal force adjustment in MPC	$R_{F_{x_f}}$	1e-8
Weight on rear axle longitudinal force adjustment in MPC	$R_{F_{xr}}$	1e-8
Weight on yaw moment adjustment in MPC	R_{G_z}	4e-8
Weight on longitudinal CG force adjustment in HCC	W_{F_X}	1
Weight on lateral CG force adjustment in HCC	W_{F_Y}	1
Weight on CG yaw moment adjustment in HCC	W_{G_Z}	1

The tuning values shown in Table 4.3 provide satisfactory results for the used testing scenarios, and are achieved through trial and error. As some parameters such as vehicle mass may change, the tuning values shown in Table 4.3 may also need to be changed for the most competent control performance. However, minor changes may not affect the control performance significantly and are assumed to be negligible [85]. The full controller was implemented using a dSPACE Auto-box on the electric vehicle. The yaw rate of the vehicle can be measured using the IMU system. The lateral and longitudinal velocities that were used to compute the sideslip angle and slip ratio were obtained using the GPS system shown in Fig 4.9(c).

(a)

(b) **(c)**

Fig 4.9 Testing facilities (a) full-electric GM Chevrolet Equinox platform (b) Electric motors used for torque vectoring (c) GPS mechanism

The control objective is to preserve the integrated longitudinal and lateral vehicle stability and minimize the deviation of the actual longitudinal and lateral dynamics (wheel slip ratio, lateral velocity, yaw rate, and yaw angle) from the desired courses with torque adjustments. The control inputs are the required torque adjustments at each wheel that compensates for the CG longitudinal force and yaw moment errors. Three types of maneuvers that may violate the vehicle stability are designed. Double lane change (DLC) that may excite the vehicle stability in the lateral direction, a full-throttle launch that may excite the vehicle stability in the longitudinal direction, and an acceleration in turn that may excite the vehicle stability in both longitudinal and lateral directions and easily push the tire capacity to saturation. Low traction road conditions were obtained by using a wet sealer (darker patch of asphalt in Fig 4.9(a)). The road friction coefficient of the wet sealer can be calculated by continuous brake with ABS to avoid wheel longitudinal slip on straight line and then measuring the maximum longitudinal braking acceleration on the surface. According to the definition of the road friction coefficient, one can write:

$$\mu g = \max(\sqrt{{a_x}^2 + {a_y}^2}) \tag{4.40}$$

Assuming negligible lateral acceleration on a straight-line braking maneuver and using the experimental test data from Fig 4.10, maximum acceleration can be substituted with 4 $^{m}/_{s^2}$ approximately, and according to Eq. (4.40), it can be concluded that the road friction coefficient on wet sealer is approximately equal to 0.4.

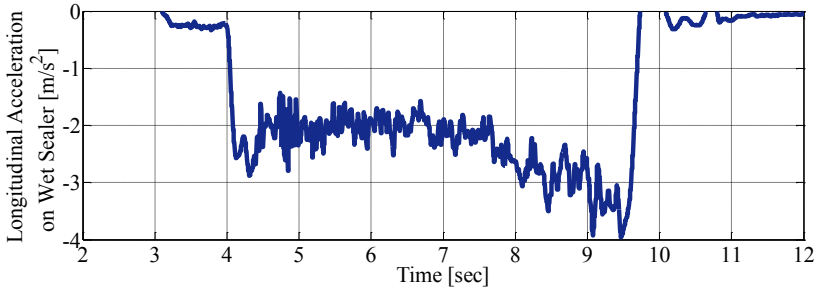

Fig 4.10 Straight-line braking with ABS on wet sealer

In the following figures in this thesis, subscripts *des* and *act* stands for the desired and actual quantities of their respective parameters.

I. Scenario: A double lane change maneuver on dry road

As mentioned in Chapter 3, a model based control structure provides a reduced control process settling time, increases control performance consistency and quality with a smoother control sequence, and operates closer to vehicle system specifications. In order to investigate the effect of the MPC prediction model that has been used in the high-level control module, the yaw moment adjustment of the proposed MPC high-level control module is compared to a simple state-feedback controller. A double lane change maneuver has been performed on a dry surface where Fig 4.11 and Fig 4.12 show the vehicle's forward speed and driver steering command. As seen in Fig 4.11, the vehicle speed is approximately constant during the driving scenario and throttle has not been involved.

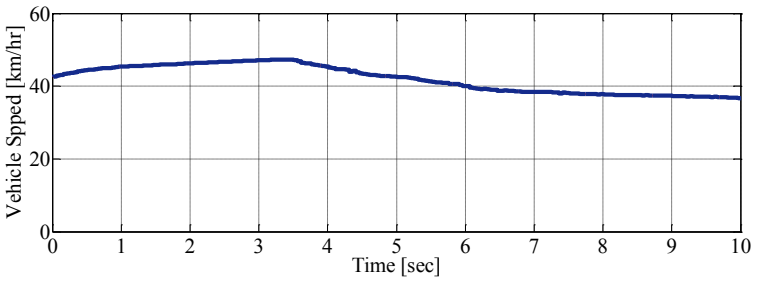

Fig 4.11 Vehicle speed in a DLC maneuver on dry surface (controlled via torque adjustment)

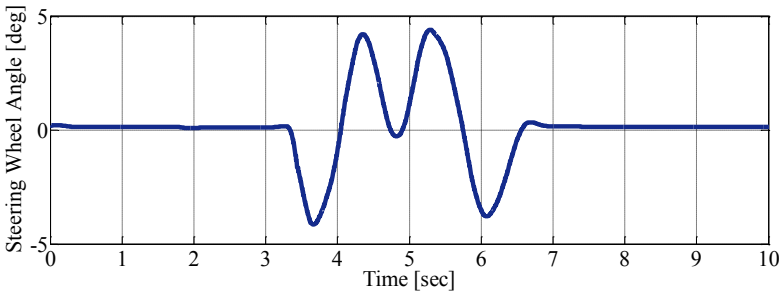

Fig 4.12 Driver steering command in a DLC maneuver on dry surface (controlled via torque adjustment)

The vehicle sideslip angle and yaw rate responses are shown in Fig 4.13 and Fig 4.14, respectively. The vehicle sideslip response shows that the vehicle was stable since the sideslip angle was less than 4 degrees on a dry road condition. The yaw rate tracking response is also desirable as it could track the desired signal. The vehicle lateral response is enhanced due to the torque adjustment shown in Fig 4.15, where *fl*, *fr*, *rl*, and *rr* indicate torque adjustments in the front left, front rear, rear left, and rear right wheel, respectively. The actuation system that has been used to generate the required yaw moment is a differential braking system. The proposed control structure works properly with the differential braking system as well as electric motors. The main goal of this driving scenario was to illustrate how using the MPC control theory provides a model based control signal that is predictive and consequently, faster and smoother than a simple state-feedback control signal. In order to study this issue, the yaw moment adjustment of the MPC high-level control module is compared to a state-feedback control signal shown with subscript SFB in Fig 4.16. In this test, the control signal that is used in a low-level control module belongs to the MPC control module, but for comparison purposes, the control signal of the state-feedback controller is also recoded on the memory. According to this figure, the MPC shows its capability of providing a control signal with less lag as the control signal peaks

in faster response to the vehicle dynamic error compared to the state feedback controller. Since the tuned weights can be different in two different controllers, the state-feedback controller requests a larger yaw moment compensation, however, the satisfactory lateral stability response of the vehicle shows that the desired vehicle states are trackable with less yaw moment compensation and energy consumption.

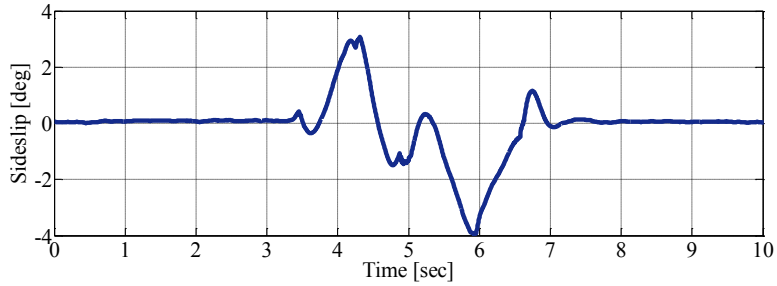

Fig 4.13 Sideslip response in a DLC maneuver on dry surface (controlled via torque adjustment)

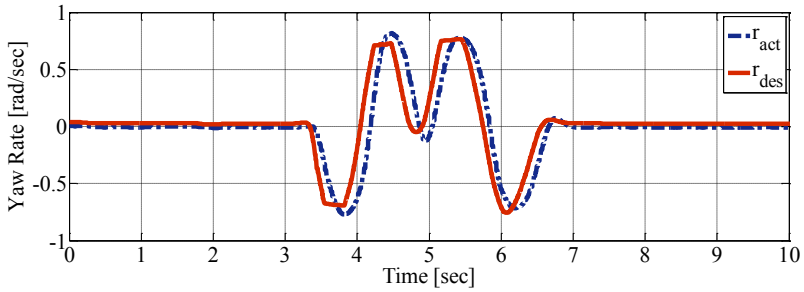

Fig4.14 Yaw rate response in a DLC maneuver on dry surface (controlled via torque adjustment)

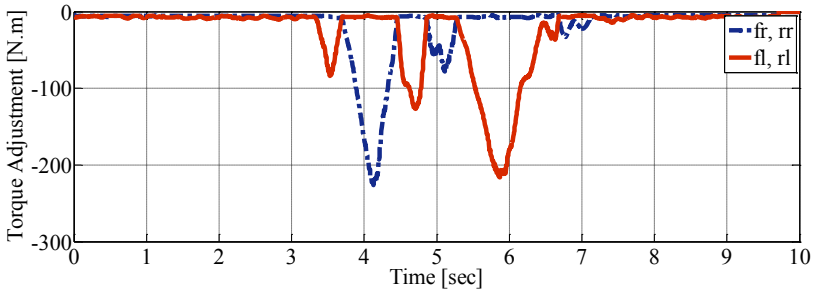

Fig 4.15 Wheel torque adjustment in a DLC maneuver on dry surface

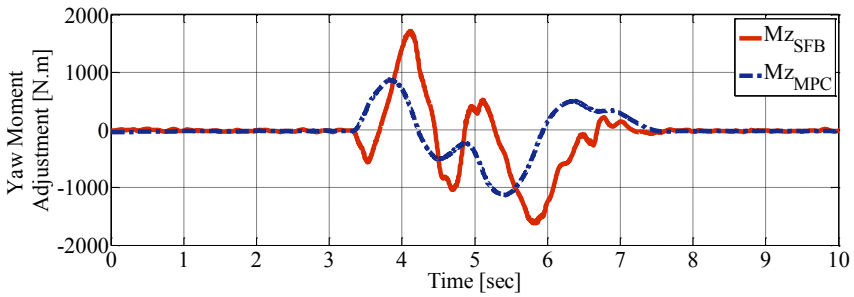

Fig 4.16 Yaw moment adjustment in a DLC maneuver on dry surface

II. Scenario: A double lane change maneuver on wet sealer

In this scenario, the control structure is tested using a double lane change, where the maneuver took place on a slippery road condition with an approximate friction coefficient of 0.4 at a speed of 40 km/h as seen in Fig 4.17. The steering angle was applied after six seconds of driving with an approximate amplitude of 4 radians as shown in Fig 4.18. The vehicle sideslip angle is less than 3 degrees during this driving scenario, and the vehicle remains in a stable region as illustrated in Fig 4.19. The yaw rate response also shows success in tracking the desired signal in Fig 4.20. The torque adjustments at each wheel, are shown in Fig 4.21, where electric motors are used as actuators. The distribution of the torque is symmetric when the wheel slip ratio is not considerable and the control scheme only aims to generate a corrective yaw moment with torque vectoring for better stability and steerability purposes.

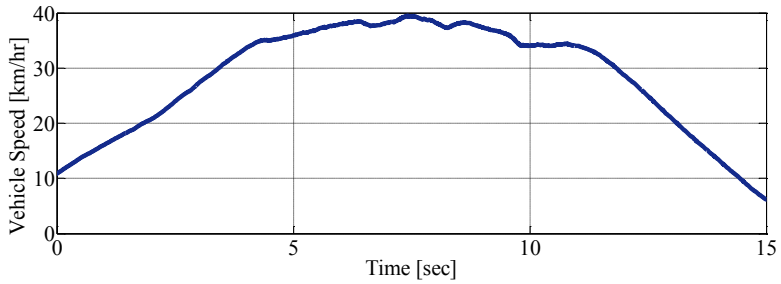

Fig 4.17 Vehicle speed in a DLC maneuver on wet surface (controlled via torque adjustment)

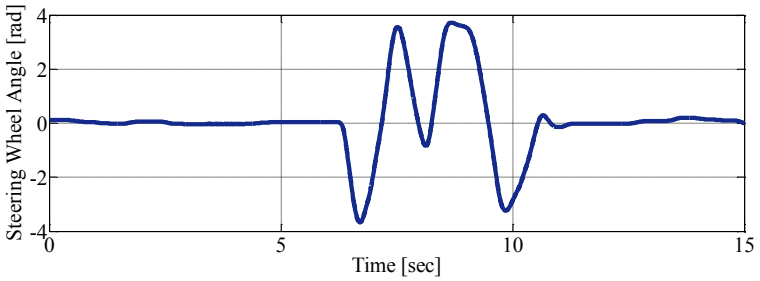

Fig 4.18 Driver steering angle command in a DLC maneuver on wet surface (controlled via torque adjustment)

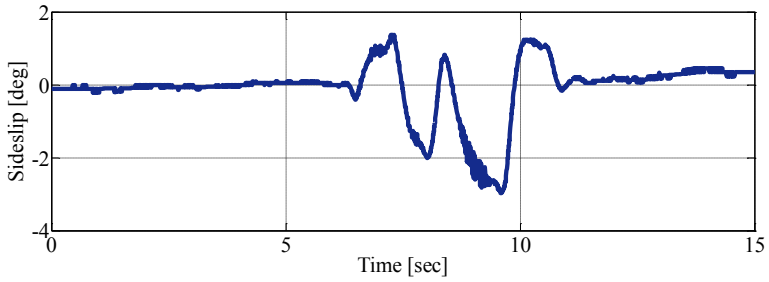

Fig 4.19 Sideslip angle response in a DLC maneuver on wet surface (controlled via torque adjustment)

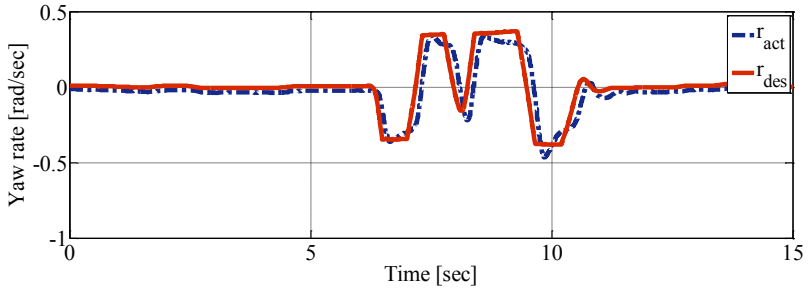

Fig 4.20 Yaw rate response in a DLC maneuver on wet surface (controlled via torque adjustment)

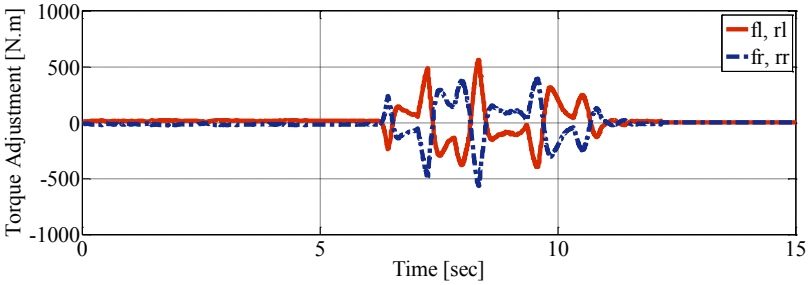

Fig 4.21 Wheel torque adjustment in a DLC maneuver on wet surface

A similar driving scenario was performed without active control on the vehicle. Fig 4.22 and Fig 4.23 show the speed change and driver steering command that is very similar to the previous driving scenario for a fair comparison of the vehicle's controlled and uncontrolled responses. As seen in Fig 4.24 and Fig 4.25, the vehicle is unstable due to harsh maneuvering. This resulted in a loss of yaw rate tracking and sideslip control and vehicle lateral skidding.

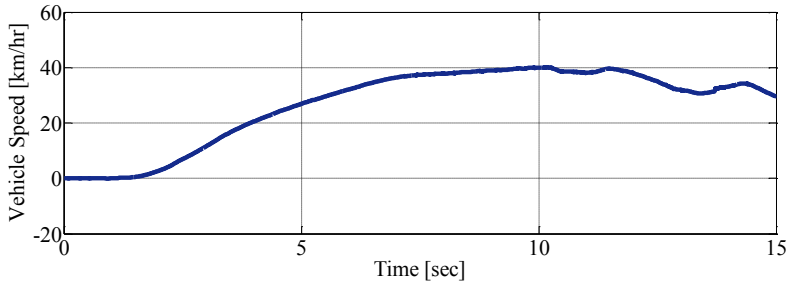

Fig 4.22 Vehicle Speed in a DLC maneuver on wet surface (uncontrolled)

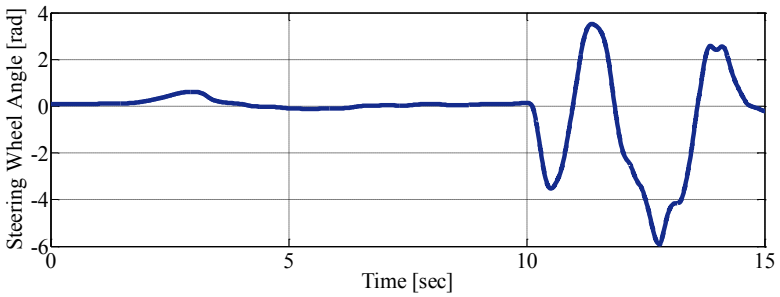

Fig 4.23 Driver steering command in a DLC maneuver on wet surface (uncontrolled)

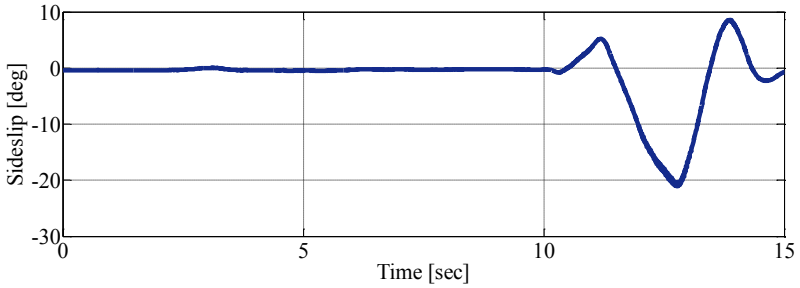

Fig 4.24 Sideslip response in a DLC maneuver on wet surface (uncontrolled)

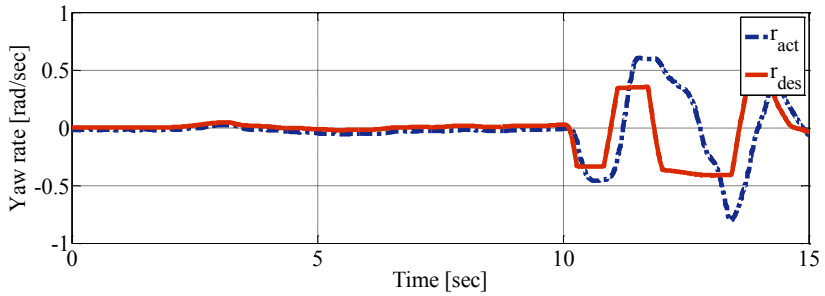

Fig 4.25 Yaw rate response in a DLC maneuver on wet surface (uncontrolled)

III. Scenario: A full-throttle launch

In order to evaluate the capability of the control system in maintaining wheel slip ratios less than a certain threshold, a launch maneuver with full throttle starting from rest on a low friction surface of an approximate coefficient of 0.4 was performed. The gas pedal is pressed by the driver after the first second of driving to investigate the launch effect on longitudinal vehicle stability and wheel slip ratios. During such a harsh maneuver, the controller should generate a negative torque to reduce the requested driver torque and prevent wheel instability. Note that driving torque reduction does not necessarily mean braking but could simply be easing the throttle input. Achieving the target course with the maximum admissible wheel slip ratio in a few seconds could be considered as a success. The driver torque request during this maneuver is shown in Fig 4.26, and the maximum wheel slip ratio due to this request is shown in Fig 4.27. As this figure demonstrates, the maximum wheel slip ratio was brought under control in less than 2 seconds. The optimally distributed torque is illustrated in Fig 4.28. As seen, if the maximum slip ratio is distancing from the desired value, a feedback negative torque is generated to decrease the total wheel torque and generally compensate for the error between the threshold and the actual maximum slip ratio signal.

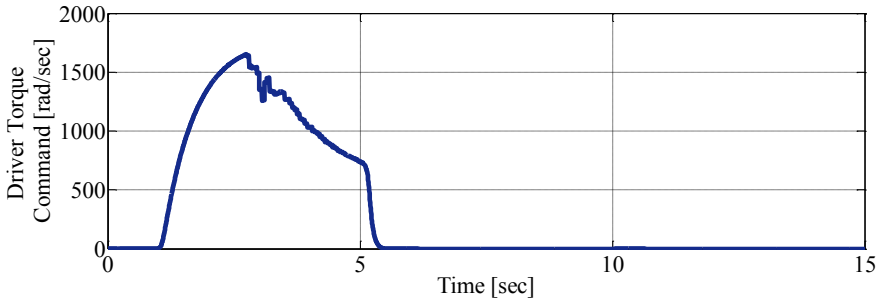

Fig 4.26 Driver torque command in a full throttle launch on wet surface (controlled via torque adjustment)

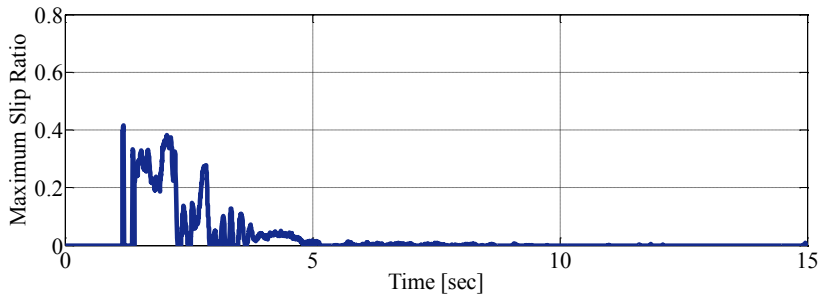

Fig 4.27 Wheel longitudinal slip ratios in a full throttle launch on wet surface (controlled via torque adjustment)

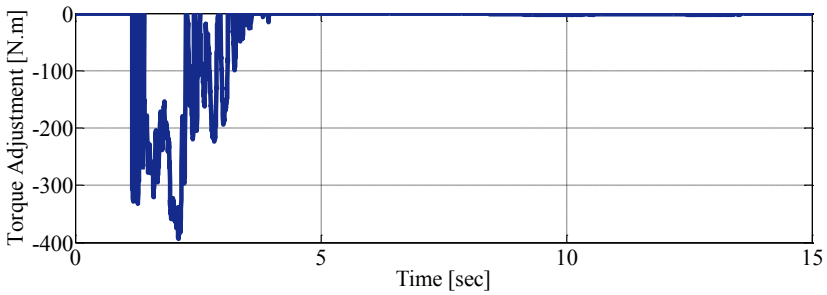

Fig 4.28 Wheel torque adjustment in a full throttle launch on wet surface

A similar driving scenario was performed on the vehicle without a controller for comparison purposes. As seen in Fig 4.29, the maximum wheel slip ratio indicates the instability of at least one of the wheels due to harsh acceleration and a large driver torque request on a wet surface. As soon as the vehicle body inertia becomes synchronized with the rapid wheel dynamics, the slip ratios are naturally decreased.

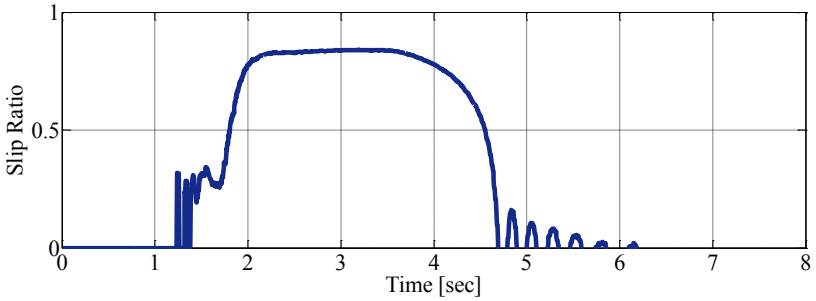

Fig 4.29 Wheel maximum longitudinal slip ratio in a full throttle launch on wet surface (uncontrolled)

IV. Scenario: Full-throttle launch on dry surface and then single lane change on wet surface

In order to demonstrate some of the performance qualifications of an integrated longitudinal and lateral stability control system, a driving scenario has been designed to

invoke both wheel slip and vehicle yaw instability. In this scenario, the driver attempts to start the maneuver from rest on a dry surface with an approximate road friction coefficient of 0.9, and then, the driver performs a single lane change maneuver on wet sealer with an approximate road friction coefficient of 0.4. The vehicle speed and steering command during the first 10 seconds of the maneuver are recorded as shown in Fig 4.30 and Fig 4.31. Additionally, the driver torque request in this scenario is shown in Fig 4.32.

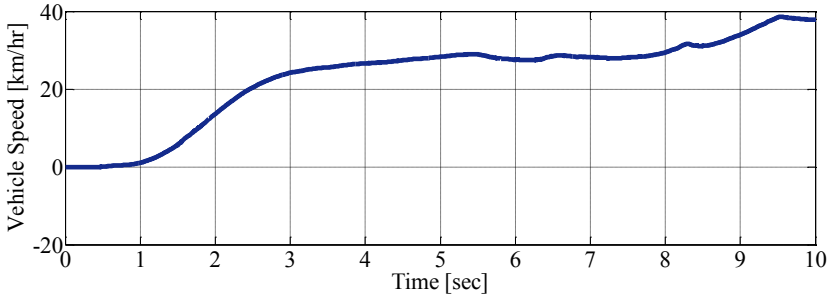

Fig 4.30 Vehicle Speed in a full throttle launch on dry surface and then single lane on wet surface (controlled via torque adjustment)

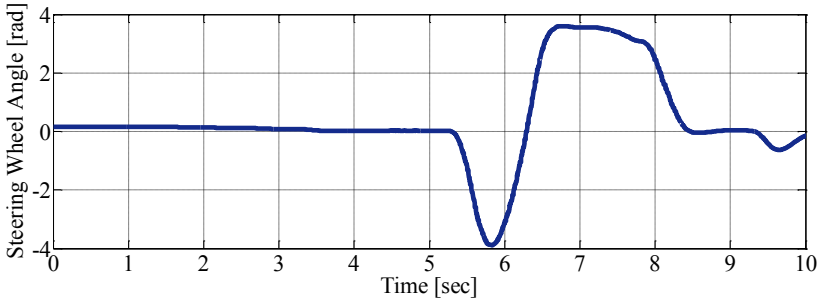

Fig 4.31 Driver steering command in a full throttle launch on dry surface and then single lane on wet surface (controlled via torque adjustment)

At the beginning of this driving scenario, as shown in Fig 4.33, large wheel slip ratios owing to the driver's high torque demand and low vehicle body inertia (starting from the rest condition) occurred. Since the control objective is to provide integrated longitudinal and lateral stability control, the controller requested a negative torque in these initial seconds to decrease the transferred torque to the wheels and stabilize the vehicle in the longitudinal direction as seen in Fig 4.36. As mentioned, electric motors have been utilized to generate the required positive/negative torque adjustments. It can be perceived that the distributed torque could bring the wheel slip ratios under control in less than a second. Fig 4.34 and Fig 4.35 report success in lateral stability and maneuverability during a single lane change on a low traction surface. As Fig 4.36 illustrates, while the driver steers to

change the lane, the control system decides on a torque adjustment such that a corrective yaw moment is generated to enable the vehicle to follow the desired yaw trajectory. In addition, it can be seen that the adjusted torques are symmetric on left and right sides of the vehicle. This is due to the fact that the wheels did not experience significant longitudinal slip, and all the control effort was devoted to enhancing the handling performance.

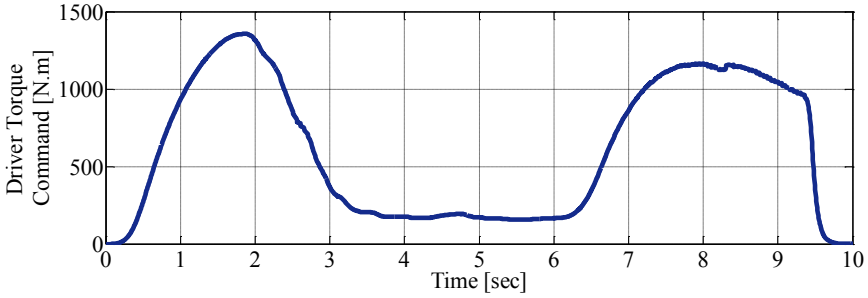

Fig4.32 Driver torque request in a full throttle launch on dry surface and then single lane change on wet surface (controlled via torque adjustment)

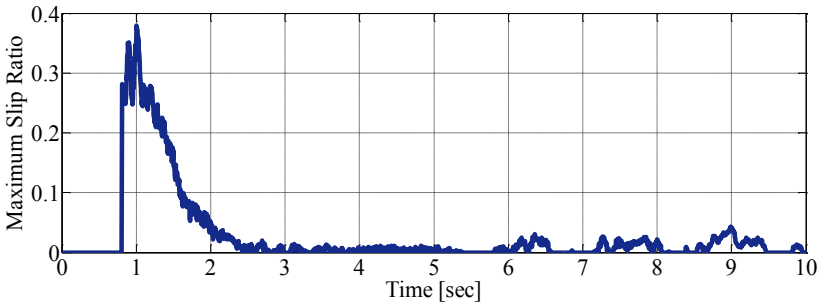

Fig 4.33 Wheel maximum longitudinal slip ratio in a full throttle launch on dry surface and then single lane change on wet surface (controlled via torque adjustment)

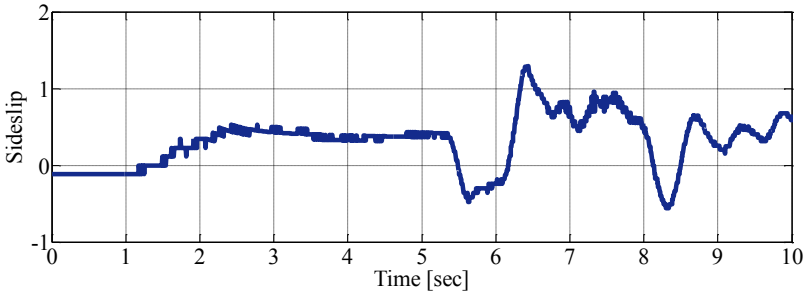

Fig 4.34 Sideslip angle response in a full throttle launch on dry surface and then single lane on wet surface

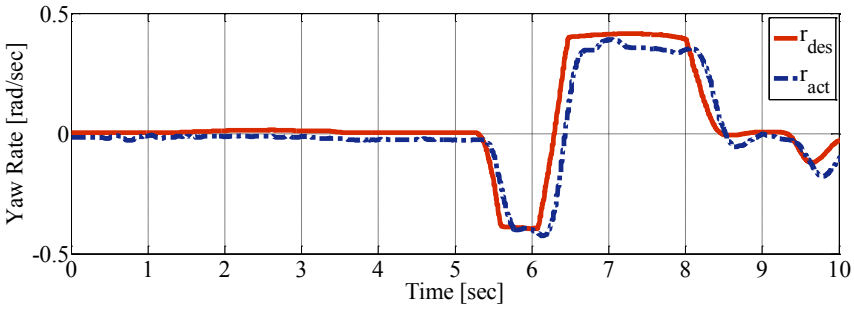

Fig 4.35 Yaw rate response in full throttle launch on dry surface and then single lane on wet surface (controlled via torque adjustment)

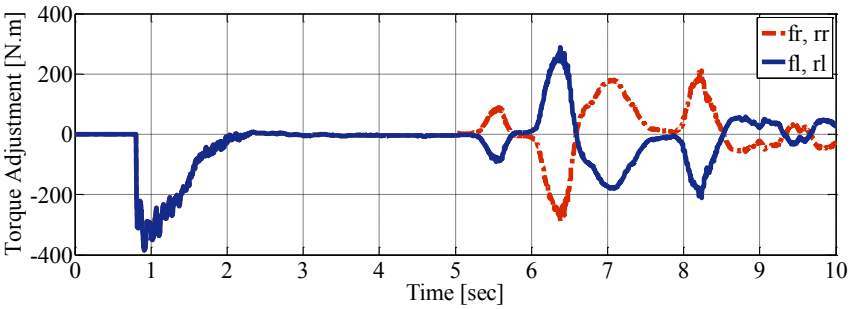

Fig 4.36 Wheel torque adjustments in a full throttle launch on dry surface and then single lane change on wet surface (controlled via torque adjustment)

V. Scenario: Acceleration in a mild turn on wet surface

The capability of the proposed control structure can be shown perfectly in critical driving situations where both directional instabilities of a planar motion are prone to occur. In this designed scenario, the driver attempts to accomplish a mild turn on wet sealer while pushing the gas pedal down harshly between the seconds of 7 to 11. The vehicle's forward speed and steering road angle are shown in Fig 4.37 and Fig 4.38, respectively. Furthermore, the driver torque request is shown in Fig 4.39 in this scenario.

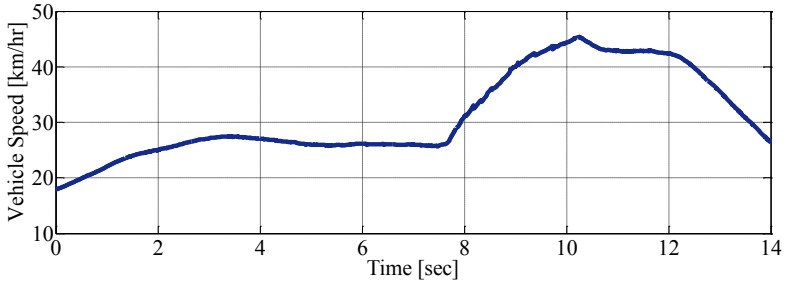

Fig 4.37 Vehicle Speed in an acceleration in turn on wet surface (controlled via torque adjustment)

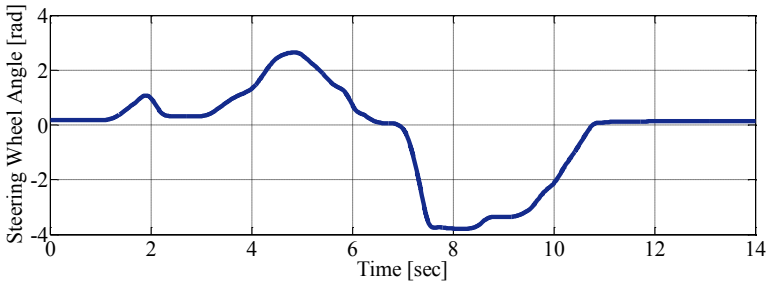

Fig 4.38 Driver steering angle command in acceleration in turn on a wet surface

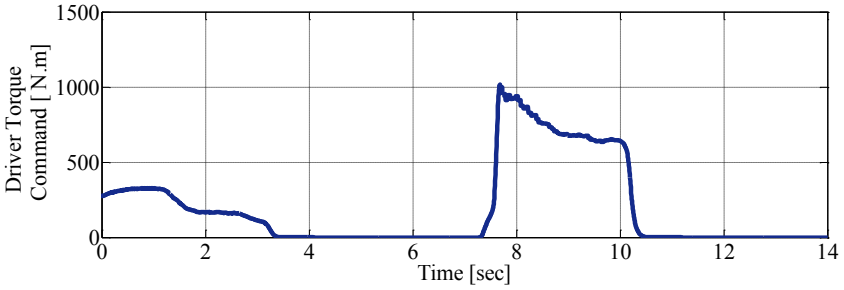

Fig 4.39 Driver torque request while acceleration in turn on a wet surface

The vehicle lateral stability has been preserved since the vehicle sideslip is under control and is less than 4 degrees during the turning period as seen in Fig 4.40, and the yaw rate tracking response is adequate as reported in Fig 4.41. The maximum wheel slip ratio as an indicator of vehicle longitudinal stability is also shown in Fig 4.42. As illustrated in Fig 4.43, integrated vehicle chassis and wheel slip ratio stability is maintained by the generation of differential negative torque adjustments to decrease the maximum wheel slip ratio as well as perform a safe turn. The negativity can be correlated to driver torque reduction and wheel stability preservation while differentiation can be correlated to the required yaw moment correction. This figure also shows that as soon as the wheel slip ratios become insignificant after the 10^{th} second, the torque adjustment is generated only to improve vehicle handling, so it follows a symmetric trend.

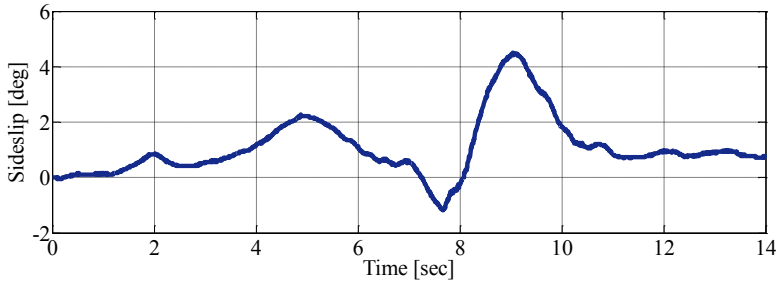

Fig 4.40 Sideslip response in an acceleration in turn on wet surface (controlled via torque adjustment)

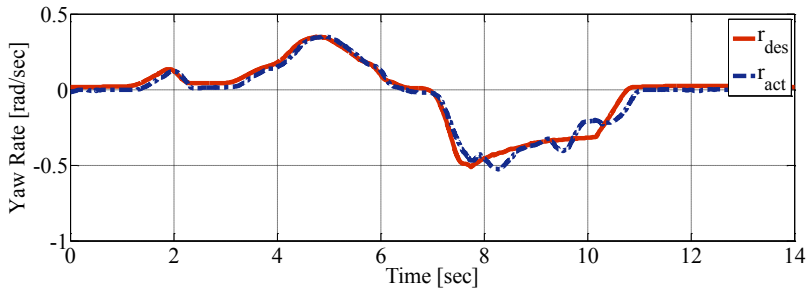

Fig 4.41 Yaw rate response in an acceleration in turn on wet surface (controlled via torque adjustment)

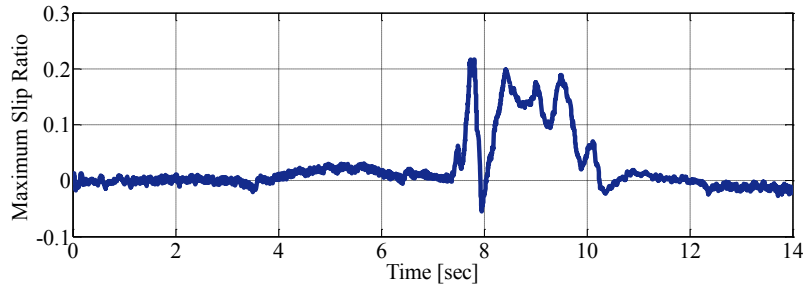

Fig 4.42 Wheel maximum longitudinal slip ratio in an acceleration in turn on wet surface (controlled via torque adjustment)

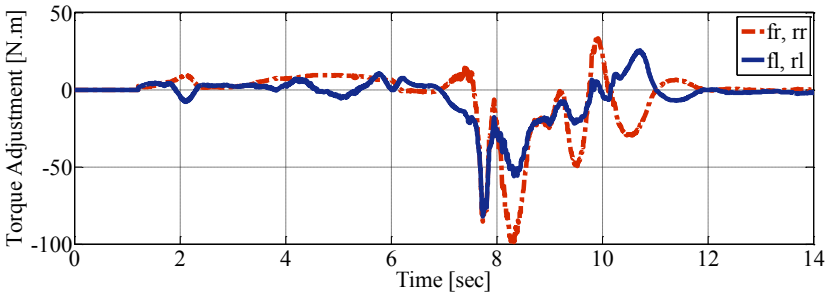

Fig4.43 Wheel torque adjustments in an acceleration in turn on wet surface (controlled via torque adjustment)

VI. Scenario: Acceleration in a harsh turn on wet surface

In this challenging driving scenario, an acceleration in a harsh turn maneuver has been performed on wet sealer where the tires are more subject saturation in both longitudinal and lateral directions. The actuation system that has been used to generate the required yaw moment and longitudinal force adjustments is a differential braking system. The control algorithm used in low-level module allows for the use of different actuators (electric motors and ABS). The vehicle's forward speed and the steering road angle are shown in Fig 4.44

and Fig 4.45, respectively. The driver accelerates between 3 to 6 seconds while turning as illustrated in Fig 4.46.

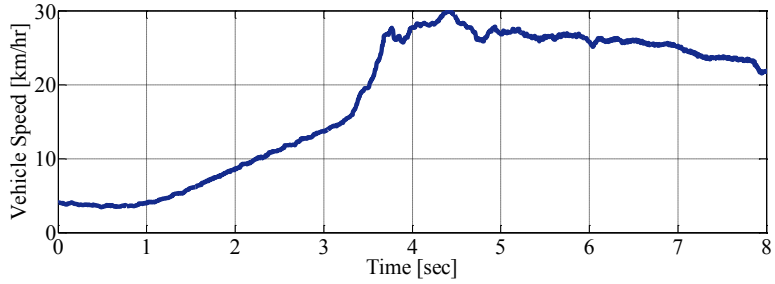

Fig 4.44 Vehicle Speed in a harsh acceleration in turn on wet surface (controlled via torque adjustment)

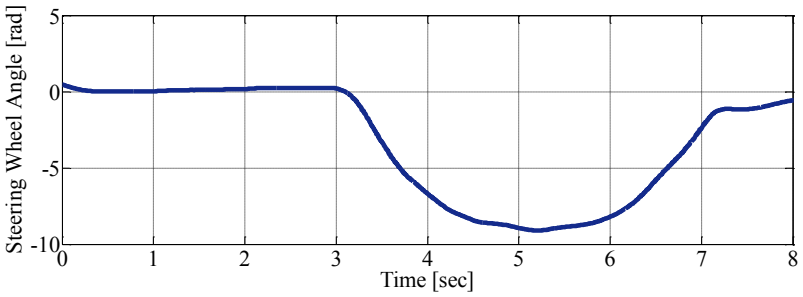

Fig 4.45 Driver steering command in a harsh acceleration in turn on wet surface (controlled via torque adjustment)

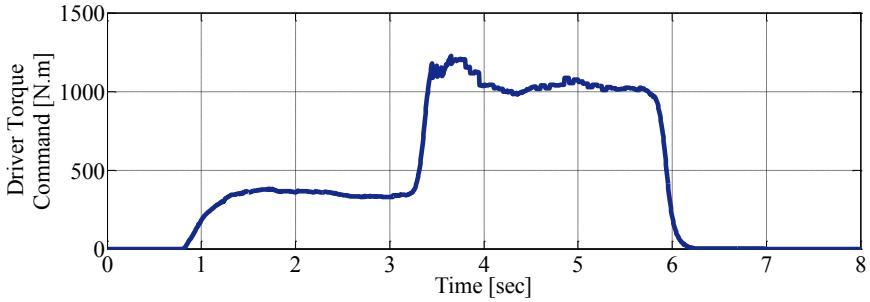

Fig 4.46 Driver torque request in a hash acceleration in turn on wet surface (controlled via torque adjustment)

The lateral stability has been maintained since the vehicle sideslip was taken under control and it reported less than 2 degrees in turn, as shown in Fig 4.47. The yaw rate tracking response shows a proper reference following shown in Fig 4.48. The maximum wheel slip ratio was studied to analyze longitudinal stability and reported in Fig 4.49. The amount of the negative torque adjustment is proportional to the maximum wheel slip ratio and lateral dynamics (sideslip and yaw rate) errors shown in Fig 4.50. As the maximum wheel slip

ratio increases, the negative torque at both left and right sides increase equally. However, after a longitudinal slip drop, torque adjustment is mainly devoted to lateral dynamics maintenance.

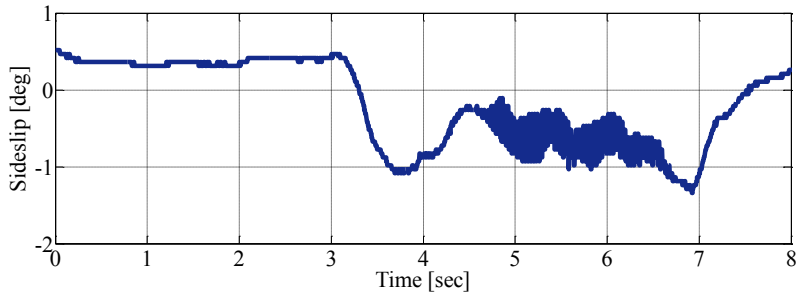

Fig 4.47 Sideslip response in a harsh acceleration in turn on wet surface (controlled via torque adjustment)

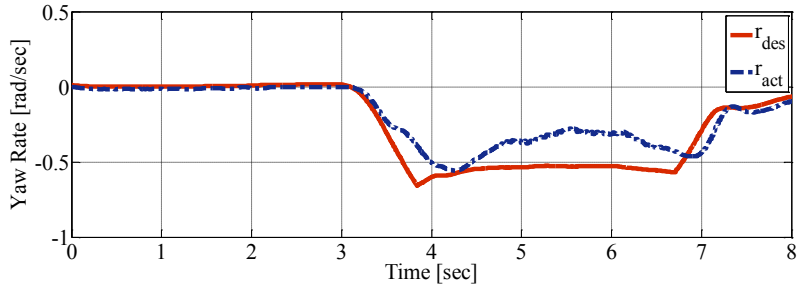

Fig 4.48 Yaw rate response in a harsh acceleration in turn on wet surface (controlled via torque adjustment)

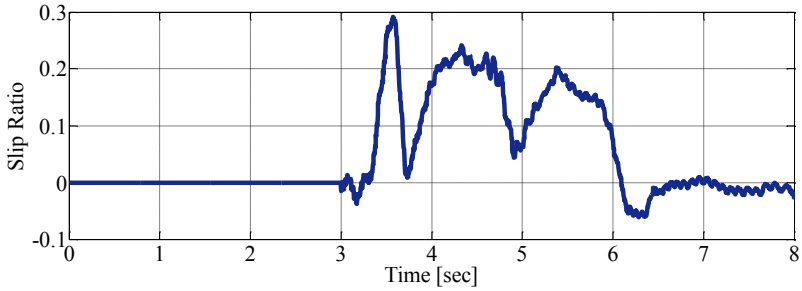

Fig 4.49 Wheel maximum longitudinal slip ratio in a harsh acceleration in turn on wet surface (controlled via torque adjustment)

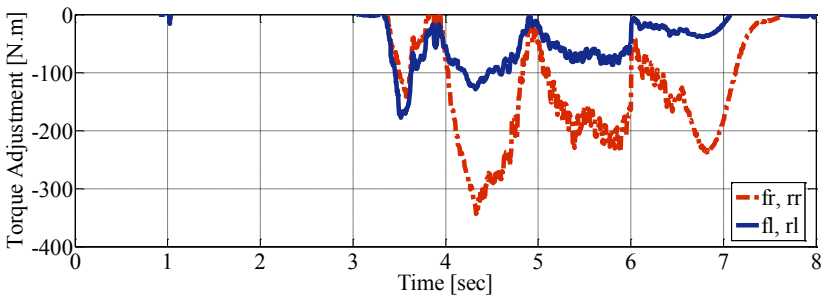

Fig 4.50 Wheel torque adjustments in a harsh acceleration in turn on wet surface (controlled via torque adjustment)

4.6 Summary

In this chapter, the design process of the proposed modular control structure for an integrated vehicle longitudinal and lateral stability control (wheel slip ratio and vehicle chassis control) was discussed with torque vectoring control methodology. According to CG horizontal forces and yaw moment error analysis in the high-level control module, a control intervention was designed in the low-level module to minimize this error. In fact, the low-level module was responsible for the optimal torque allocation considering actuation functionality bandwidth. The performance of the controller was evaluated using an electric vehicle equipped with electric motors and a differential braking system. Experimental results show success in integrated control in several challenging maneuvers. The driving scenarios were designed to push the tire forces into a nonlinear region where the uncontrolled vehicle was unstable. As shown, the control structure was working properly with different actuation systems such as electric motors and differential braking system. The collected data from the test track in different scenarios such as double lane change, full-throttle launch, and acceleration in turn on slippery road conditions illustrated the performance qualifications of such a controller in vehicle integrated stability maintenance.

Chapter 5

Vehicle Stability Control via Combined Torque Vectoring and Active Steering

5.1 Introduction

In the previous chapter, an integrated longitudinal and lateral vehicle stability control is discussed with torque vectoring actuators such as electric motors and differential braking. In this technique, the longitudinal tire force is adjusted such that it provides the required CG longitudinal force and yaw moment corrections for vehicle stability. As mentioned before, implementation of the proposed control structure on various vehicle configurations with different actuator and drivetrain layouts is a feasible task due to the specific design features of the control structure. As vehicle CG stability can be maintained with control interventions at corners, any actuation system that can adjust corner forces could perform well. In this chapter, the vehicle stabilization is studied with combined torque vectoring and active steering techniques. In addition to the longitudinal tire force, the lateral tire force is also adjustable with the available multi-actuation system. In this chapter, first, the general control structure design with the coordinated TV and AS technique is discussed. Second, MPC high-level and HCC low-level module designs for the new multi-actuator case are discussed. Finally, simulation and experimental test results are provided to evaluate the competency of the combined TV and AS methodology.

5.2 General Scheme of Control Structure via Torque and Steering Adjustments

The proposed control structure is illustrated schematically in Fig 5.1. In addition to integrated vehicle stability control, another major design objective of the proposed control structure is re-configurability and proper coordination with various actuators and drivetrain layouts. The integrated longitudinal and lateral stability control (wheel slip and vehicle chassis control) stability analysis is accomplished using indicators such as lateral velocity, yaw rate, yaw angle, and wheel slip ratios. The desired lateral dynamics (lateral velocity,

yaw rate, and yaw angle) is calculated based on driver steering (θ) and torque (T) commands. The desired longitudinal dynamics (optimal wheel slip ratio) is also calculated based on driver steering command and road surface. As mentioned before, the control technique used in the high-level module is an MPC reference state tracking. A prediction model is utilized to predict future dynamic states based on measured/estimated states and required control adjustments which are CG longitudinal and lateral forces and yaw moment ($\delta F_{X_{CG}}$, $\delta F_{Y_{CG}}$ and $\delta G_{Z_{CG}}$) over a finite control horizon. The control adjustments are outcomes of solving an MPC optimization problem that basically minimizes the error between actual and target courses. The lateral force adjustment is calculated based on steering adjustment $\delta\theta$ and a combined-slip Burkhardt tire model. At each sampling time, the first set of resultant CG horizontal forces and yaw moment adjustments are employed in the low-level control module, where optimal torque allocation (δT) is accomplished by solving a single-step HCC optimization. As shown in Chapter 3, the HCC optimization cost function is defined based on CG horizontal forces, yaw moment errors, and corner torque adjustments as control inputs. In the following section, the design procedure of each level of the proposed integrated controller is discussed for the combined TV and AS actuators.

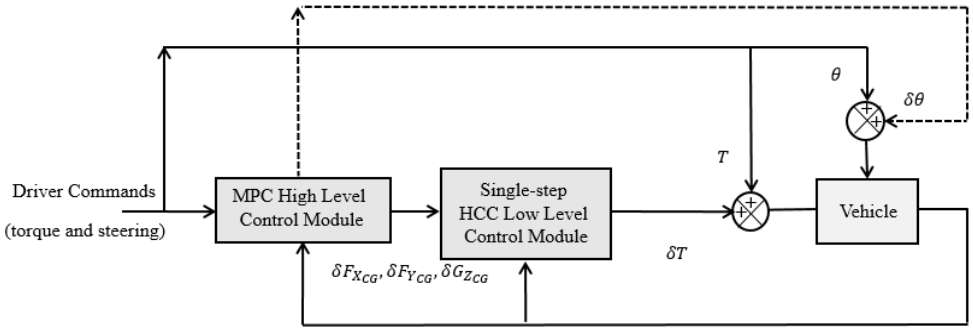

Fig 5.1 Schematic of the proposed modular control structure with torque and steering adjustments

5.3 MPC High-Level Control Module Design via Torque and Steering Adjustments

In this section, the prediction model that has been utilized in the MPC high-level control module is described for an integrated vehicle stability control via combined torque and steering adjustments. The control objective is following the desired longitudinal and lateral

dynamics and maintaining plane motion stability. As discussed in Chapter 4, the prediction model adopted in the MPC algorithm is a bicycle vehicle model shown in Fig 5.2. This model provides a satisfactory approximation of the vehicle dynamic response with a low computational cost and real-time implementability. According to Fig 5.2, the vehicle CG horizontal forces and yaw moment can be formulated based on corner horizontal forces and road steering as:

$$F_{X_{CG}} = F_{x_f}\cos(\theta + \delta\theta) - F_{y_f}\sin(\theta + \delta\theta) + F_{x_r} \tag{5.1a}$$

$$F_{Y_{CG}} = F_{y_f}\cos(\theta + \delta\theta) + F_{y_r} + F_{x_f}\sin(\theta + \delta\theta) \tag{5.1b}$$

$$G_{Z_{CG}} = L_f F_{y_f}\cos(\theta + \delta\theta) - L_r F_{y_r} + L_f F_{x_f}\sin(\theta + \delta\theta) + \delta G_{z_{CG}} \tag{5.1c}$$

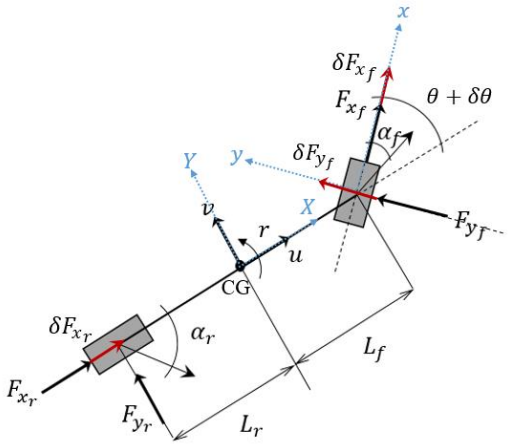

Fig 5.2 Bicycle vehicle model with torque and steering interventions

In the above equation, *m* is the vehicle mass and I_z is the vehicle inertia around the vertical axis. Also, the notations v and u are the vehicle CG velocities in the longitudinal and lateral directions, r is the vehicle yaw rate. The axle longitudinal force in Eq. (5.1) is estimated at each sampling, and the lateral force is calculated with a piecewise linearized model as:

$$F_{y_i} = \hat{F}_{y_i} + \delta F_{y_i} \qquad \text{for } i = \{f, r\} \tag{5.2a}$$

$$\delta F_{y_i} = \bar{C}_{\alpha_i}\Delta\alpha_i \tag{5.2b}$$

where the first term $\hat{F}_{y_i}$ is the estimated axle lateral force at each sampling time, and the second term is the possible change of the lateral force at time t due to road steering adjustments. This term can be computed using a combined-slip tire cornering coefficient

and vehicle lateral slip change. The lateral slip change can be calculated using Eq. (4.18), where front and rear lateral slips can be obtained as:

$$\alpha_f \approx \theta + \delta\theta - \frac{v + L_f r}{u} \tag{5.3a}$$

$$\alpha_r \approx -\frac{v - L_r r}{u} \tag{5.3b}$$

According to the steering adjustment at the front axle, Eq. (4.11) is updated as:

$$\begin{aligned} &\dot{\lambda}_{fl} \\ &= \dot{\omega}_{fl}/\omega_{fl}\left(1 - \lambda_{fl}\right) \\ &- \left(a_{X_{fl}}\cos(\theta + \delta\theta) + a_{Y_{fl}}\sin(\theta + \delta\theta)/R_e\omega_{fl}\right. \end{aligned} \tag{5.4a}$$

$$\begin{aligned} &\dot{\lambda}_{fr} \\ &= \dot{\omega}_{fr}/\omega_{fr}\left(1 - \lambda_{fr}\right) \\ &- \left(a_{X_{fr}}\cos(\theta + \delta\theta) + a_{Y_{fr}}\sin(\theta + \delta\theta)/R_e\omega_{fr}\right. \end{aligned} \tag{5.4b}$$

$$\dot{\lambda}_{rl} = \dot{\omega}_{rl}/\omega_{rl}\,(1 - \lambda_{rl}) - a_{X_{rl}}/R_e\omega_{rl} \tag{5.4c}$$

$$\dot{\lambda}_{rr} = \dot{\omega}_{rr}/\omega_{rr}\,(1 - \lambda_{rr}) - a_{X_{rr}}/R_e\omega_{rr} \tag{5.4d}$$

where, $a_{X_{ij}}$ and $a_{Y_{ij}}$ can be computed as shown in Eq. (4.12). The MPC prediction model in Chapter 4 is revised with Eq. (5.1) - (5.4) to consider the effect of steering adjustment at the front axle. The vehicle integrated stability model that considers steering and torque adjustments can be described by the following compact state-space model:

$$\dot{\xi} = \bar{g}(\xi_t, \vartheta_t) \tag{5.5a}$$

$$\eta = \bar{h}(\xi_t) \tag{5.5b}$$

According to Eq. (5.5), the vehicle dynamics shows a nonlinear behavior. An assumption has been made in Chapter 4 where the forward speed and driver steering command changes are negligible within a few milliseconds of the sampling-time period, and as a result, those were assumed to be constant at each optimization process. Due to this assumption, the vehicle's longitudinal velocity was not considered to be a state variable in this thesis. In addition, another assumption has been made that the steering adjustment $\delta\theta$ is a small value at each sampling time that yields:

$$\sin(\theta + \delta\theta) \approx \sin\theta + \delta\theta\cos\theta \tag{5.6a}$$

$$\cos(\theta + \delta\theta) \approx \cos\theta - \delta\theta \sin\theta \tag{5.6b}$$

In the following prediction model, $\delta\theta$ is substituted with a previous step steering adjustment, which means that the steering adjustment is assumed unchanged during a unit sampling time duration. These assumptions have been made to avoid dealing with the nonlinear prediction model that often cannot be considered for real-time implementations or has a high computational cost. Finally, the state and control input vectors can be defined as:

$$\xi = \{v, r, \psi, \lambda_{max}\}^T \tag{5.7a}$$

$$\vartheta = \left\{\delta F_{x_f}, \delta F_{x_r}, \delta G_z, \delta\theta\right\}^T \tag{5.7b}$$

The prediction model for integrated vehicle stabilization through combined steering and torque adjustments has more complications compared to the one presented in Chapter 4. For clarification purposes, an explicit form of system, input, and known disturbance matrices shown in Chapter 3, are provided as:

$$A_t = \begin{bmatrix} a_{t_{11}} & a_{t_{12}} & a_{t_{13}} & a_{t_{14}} \\ a_{t_{21}} & a_{t_{22}} & a_{t_{23}} & a_{t_{24}} \\ a_{t_{31}} & a_{t_{32}} & a_{t_{33}} & a_{t_{34}} \\ a_{t_{41}} & a_{t_{42}} & a_{t_{43}} & a_{t_{44}} \end{bmatrix} \tag{5.8a}$$

$$B_t = \begin{bmatrix} b_{t_{11}} & b_{t_{12}} & b_{t_{13}} & b_{t_{14}} \\ b_{t_{21}} & b_{t_{22}} & b_{t_{23}} & b_{t_{24}} \\ b_{t_{31}} & b_{t_{32}} & b_{t_{33}} & b_{t_{34}} \\ b_{t_{41}} & b_{t_{42}} & b_{t_{43}} & b_{t_{44}} \end{bmatrix} \tag{5.8b}$$

$$C_t = \begin{bmatrix} c_{t_{11}} \\ c_{t_{21}} \\ c_{t_{31}} \\ c_{t_{41}} \end{bmatrix} \tag{5.8c}$$

By substitution of Eqs. (5.2) in Eq. (5.1) and using Eq. (5.3), (5.4), and (5.6), the elements of the system matrix are found as:

$$a_{t_{11}} = -\bar{C}_{\alpha_r}/_{mu} - \bar{C}_{\alpha_f}\cos(\theta + \delta\theta)/_{mu} \quad ,$$

$$a_{t_{12}} = \bar{C}_{\alpha_r} L_r/_{mu} - \bar{C}_{\alpha_f}\cos(\theta + \delta\theta)\, L_f/_{mu}$$

$$a_{t_{13}} = 0 \quad , \quad a_{t_{14}} = 0$$

$$a_{t_{21}} = {\bar{C}_{\alpha_r} L_r}/{I_z u} - {\bar{C}_{\alpha_f} \cos(\theta + \delta\theta)\, L_f}/{I_z u},$$

$$a_{t_{22}} = {\bar{C}_{\alpha_r} {L_r}^2}/{I_z u} - {\bar{C}_{\alpha_f} \cos(\theta + \delta\theta)\, {L_f}^2}/{I_z u}$$

$$a_{t_{23}} = 0 \quad , \quad a_{t_{24}} = 0$$

$$a_{t_{31}} = 0 \quad , \quad a_{t_{32}} = 0$$

$$a_{t_{33}} = 1 \quad , \quad a_{t_{34}} = 0$$

$$a_{t_{41}} = 0 \quad , \quad a_{t_{42}} = 0$$

$$a_{t_{43}} = 0 \quad , \quad a_{t_{44}} = -({\dot{\omega}_{ij}}/{\omega_{ij}})_{max} \quad \text{for } i = \{f, r\}, j = \{l, r\}$$

The elements of the control input matrix can be obtained as:

$$b_{t_{11}} = {\sin(\theta + \delta\theta)}/{m} \quad , \quad b_{t_{12}} = 0$$

$$b_{t_{13}} = 0 \quad , \quad b_{t_{14}} = {-\hat{F}_{y_f} \sin\delta\theta + \bar{C}_{\alpha_f} \bar{\alpha}_f \sin\delta\theta + \hat{F}_{y_f} \cos\delta\theta}/{m}$$

$$b_{t_{21}} = {L_f \sin(\theta + \delta\theta)}/{I_z} \quad , \quad b_{t_{22}} = 0$$

$$b_{t_{23}} = {1}/{I_z} \quad ,$$

$$b_{t_{24}} = {-L_f \hat{F}_{y_f} \sin\delta\theta - L_f \bar{C}_{\alpha_f} \bar{\alpha}_f \sin\delta\theta + L_f \hat{F}_{y_f} \cos\delta\theta}/{I_z}$$

$$b_{t_{31}} = 0 \quad , \quad b_{t_{32}} = 0$$

$$b_{t_{33}} = 0 \quad , \quad b_{t_{34}} = 0$$

$$b_{t_{41}} = {\cos(\theta + \delta\theta)^2}/{mR_e\omega_{fl}}$$

$$b_{t_{41}} = {\cos(\theta + \delta\theta)^2}/{mR_e\omega_{fr}}$$

$$b_{t_{41}} = {\cos(\theta + \delta\theta)}/{mR_e\omega_{rl}}$$

$$b_{t_{41}} = {\cos(\theta + \delta\theta)}/{mR_e\omega_{rr}}$$

$$b_{t_{42}} = {\cos(\theta + \delta\theta)}/{mR_e\omega_{fl}}$$

$$b_{t_{42}} = {\cos(\theta + \delta\theta)}/{mR_e\omega_{fr}}$$

$$b_{t_{42}} = {1}/{mR_e\omega_{rl}}$$

$$b_{t_{42}} = {1}/{mR_e\omega_{rr}}$$

$$b_{t_{43}} = 0 \qquad , \qquad b_{t_{44}} = 0$$

The known disturbance elements can be obtained as:

$$c_{t_{11}} = {\hat{F}_{y_r} - \bar{C}_{\alpha_r}\bar{\alpha}_r + \hat{F}_{y_f}\cos\theta + \bar{C}_{\alpha_f}(\theta + \delta\theta)\cos(\theta + \delta\theta) - \bar{C}_{\alpha_f}\bar{\alpha}_f\cos\theta + \hat{F}_{x_f}\sin\theta}/{m}$$

$$c_{t_{21}} = {-L_r\hat{F}_{y_r} + L_r\bar{C}_{\alpha_r}\bar{\alpha}_r + L_f\,\hat{F}_{y_f}\cos\theta + \bar{C}_{\alpha_f}(\theta + \delta\theta)\cos(\theta + \delta\theta) - \bar{C}_{\alpha_f}\bar{\alpha}_f\cos\theta + \hat{F}_{x_f}\sin\theta}/{m}$$

$$c_{t_{31}} = 0$$

$$c_{t_{41}} = {\dot{\omega}_{fr}}/{\omega_{fr}} + {(\hat{F}_{x_f}\cos(\theta + \delta\theta) - \hat{F}_{y_f}\sin(\theta + \delta\theta) + \hat{F}_{x_r})\cos(\theta + \delta\theta)}/{mR_e\omega_{fl}} + {(-\dot{r}L_w - r^2L_f)\cos(\theta + \delta\theta)}/{R_e\omega_{fl}} - {(a_{Y_{CG}} + \dot{r}L_f - r^2L_w)\sin(\theta + \delta\theta)}/{R_e\omega_{fl}}$$

$$c_{t_{41}} = {\dot{\omega}_{fr}}/{\omega_{fr}} + {(\hat{F}_{x_f}\cos(\theta + \delta\theta) - \hat{F}_{y_f}\sin(\theta + \delta\theta) + \hat{F}_{x_r})\cos(\theta + \delta\theta)}/{mR_e\omega_{fr}} + {(\dot{r}L_w - r^2L_f)\cos(\theta + \delta\theta)}/{R_e\omega_{fr}} - {(a_{Y_{CG}} + \dot{r}L_f + r^2L_w)\sin(\theta + \delta\theta)}/{R_e\omega_{fr}}$$

$$c_{t_{41}} = {\dot{\omega}_{rl}}/{\omega_{rl}} + {(\hat{F}_{x_f}\cos(\theta + \delta\theta) - \hat{F}_{y_f}\sin(\theta + \delta\theta) + \hat{F}_{x_r})}/{mR_e\omega_{rl}} + {(-\dot{r}L_w + r^2L_r)}/{R_e\omega_{rl}} - {(a_{Y_{CG}} - \dot{r}L_r - r^2L_w)}/{R_e\omega_{rl}}$$

$$c_{t_{41}} = {\dot{\omega}_{rr}}/{\omega_{rr}} + {(\hat{F}_{x_f}\cos(\theta + \delta\theta) - \hat{F}_{y_f}\sin(\theta + \delta\theta) + \hat{F}_{x_r})}/{mR_e\omega_{rr}} + {(\dot{r}L_w + r^2L_r)}/{R_e\omega_{rr}} - {(a_{Y_{CG}} - \dot{r}L_r + r^2L_w)}/{R_e\omega_{rl}}$$

A Step Invariant (SI) equivalent model [86] is used to provide a discretized model to handle possible matrix singularities. Finally, a discretized LTV model is obtained and based on the desired lateral and longitudinal dynamics definitions in Chapter 4 (see Eq. (4.27) - (4.34) and Eq. (5.41)), and MPC optimization problem shown in Eq. (3.3) is formed for the integrated vehicle stability control through torque and steering adjustments.

5.4 HCC Low-Level Optimal Torque Distributor Design via Torque and Steering Adjustments

According to the general modular control structure that is proposed and illustrated in Chapter 3, the optimal longitudinal force and yaw moment adjustments generated by the MPC high-level module are fed in to the low-level control algorithm for optimal torque distribution. The optimal torque distribution is conducted based on the HCC strategy discussed in Chapter 3 and Chapter 4, which generally considers the discrepancies between the target and actual vehicle CG horizontal forces and yaw moment and generates a control sequence that minimizes these discrepancies. The HCC chassis control theory can be expanded to control the wheel dynamics. The wheel torque error as well as vehicle CG horizontal forces and yaw moment errors can be considered as:

$$F_{X_{des}} - F_X(\mathcal{F} + d\mathcal{F}) = F_{X_{des}} - \left\{F_X(\mathcal{F}) + \frac{dF_X(\mathcal{F} + d\mathcal{F})}{d\mathcal{F}}\delta\mathcal{F}\right\} \tag{5.9a}$$

$$F_{Y_{des}} - F_Y(\mathcal{F} + d\mathcal{F}) = F_{Y_{des}} - \left\{F_Y(\mathcal{F}) + \frac{dF_Y(\mathcal{F} + d\mathcal{F})}{d\mathcal{F}}\delta\mathcal{F}\right\} \tag{5.9b}$$

$$G_{Z_{des}} - G_Z(\mathcal{F} + d\mathcal{F}) = G_{Z_{des}} - \left\{G_Z(\mathcal{F}) + \frac{dG_Z(\mathcal{F} + d\mathcal{F})}{d\mathcal{F}}\delta\mathcal{F}\right\} \tag{5.9c}$$

$$G_{W_{ij}{}_{des}} - G_{W_{ij}}(\mathcal{F} + d\mathcal{F}) = G_{W_{ij}{}_{des}} - \left\{G_{W_{ij}}(\mathcal{F}) + \frac{dG_{W_{ij}}(\mathcal{F} + d\mathcal{F})}{d\mathcal{F}}\delta\mathcal{F}\right\} \tag{5.9d}$$

where, $i = \{f, r\}$ and $j = \{l, r\}$. As mentioned in Chapter 4, the horizontal tire forces are considered to be control sequences in the HCC torque allocation algorithm. However,

in the previous chapter, it was assumed that the vehicle is controllable through torque adjustment only. In this chapter, the vehicle is considered to be equipped with an active front steering actuation system as well as electric motors. It can be assumed that both longitudinal and lateral tire forces are adjustable using two different types of actuation systems. Rewriting Eq. (5.9) using Eq. (3.24) yields:

$$\begin{Bmatrix} F_{X_{des}} - F_X(\mathcal{F}+d\mathcal{F}) \\ F_{Y_{des}} - F_Y(\mathcal{F}+d\mathcal{F}) \\ G_{Z_{des}} - G_Z(\mathcal{F}+d\mathcal{F}) \\ G_{W_{fl}{}_{des}} - G_{W_{fl}}(\mathcal{F}+d\mathcal{F}) \\ G_{W_{fr}{}_{des}} - G_{W_{fr}}(\mathcal{F}+d\mathcal{F}) \\ G_{W_{rl}{}_{des}} - G_{W_{rl}}(\mathcal{F}+d\mathcal{F}) \\ G_{W_{rr}{}_{des}} - G_{W_{rr}}(\mathcal{F}+d\mathcal{F}) \end{Bmatrix} = E - A_{\mathcal{F}}\delta\mathcal{F} \tag{5.10}$$

where, $\mathcal{F} = \left\{F_{y_{fl}}, F_{y_{fr}}, F_{x_{rl}}, F_{x_{rr}}\right\}^T$. The Jacobian matrix $A_{\mathcal{F}}$ should be revised to consider wheel dynamics as well as vehicle chassis dynamics. According to Eqs. (3.21) and (4.4), the Jacobian matrix components for an RWD vehicle drivetrain configuration can be shown as:

$$A_{\mathcal{F}} = \begin{bmatrix} A_{\mathcal{F}_{Vehicle}} \\ A_{\mathcal{F}_{Wheel}} \end{bmatrix} \tag{5.11a}$$

$$A_{\mathcal{F}_{Vehicle}} = \tag{5.11b}$$

$$\begin{bmatrix} -\sin\theta_f & -\sin\theta_f \\ \cos\theta_f & \cos\theta_f \\ L_w\sin\theta_f + L_f\cos\theta_f & -L_w\sin\theta_f + L_f\cos\theta_f \end{bmatrix}$$

$$\begin{bmatrix} \cos\theta_r & \cos\theta_r \\ \sin\theta_r & \sin\theta_r \\ -L_w\cos\theta_r - L_r\sin\theta_r & L_w\cos\theta_r - L_r\sin\theta_r \end{bmatrix}$$

$$A_{\mathcal{F}_{Wheel}} = \begin{bmatrix} 0 & 0 & 0 & 0 \\ 0 & 0 & 0 & 0 \\ 0 & 0 & -R_e & 0 \\ 0 & 0 & 0 & -R_e \end{bmatrix} \tag{5.11c}$$

According to Fig 5.2, one can conclude that the error vector defined in Eq. (3.27) becomes:

$$E = \left\{\delta F_{x_f}\cos\theta_f + \delta F_{x_r} - \delta F_{y_f}\sin\theta_f,\ \delta F_{y_f}\cos\theta_f,\ \delta G_z,\right. \tag{5.12}$$
$$\left.\delta G_{W_{fl}},\ \delta G_{W_{fr}},\ \delta G_{W_{rl}},\ \delta G_{W_{rr}}\right\}^T$$

In above equation, δF_{x_f}, δF_{x_r}, δF_{y_f}, and δG_z error terms can be directly obtained from the MPC high-level control module, and $\delta G_{W_{fl}}$, $\delta G_{W_{fr}}$, $\delta G_{W_{rl}}$, and $\delta G_{W_{rr}}$ error terms are found using a similar approach to [89]. With the updated error and Jacobian matrix, the cost function shown in Eq. (4.44) can be minimized to find the required torque adjustments for an RWD drivetrain configuration.

5.5 Simulation and Experimental Results via Torque and Steering Adjustments

In order to show the performance qualifications of the proposed controller, simulation and experimental test results are presented in this section. An electric 4WD Chevrolet Equinox equipped with four electric motors and active front steering actuators is used for the experimental evaluations. The electric motors can be inactivated in the front or rear axles to provide different drivetrain layout configurations such as FWD and RWD. In this chapter, instead of an AWD drivetrain configuration, an RWD configuration has been selected to study since compatibility with all drivetrain configurations was promised with proposed control structure. Fig 4.9 illustrated the electric vehicle platform where the main mass, inertia, and geometrical properties were listed in Table 4.2. According to the available actuators, torque adjustment as well as the steering adjustment can be accomplished to stabilize the vehicle. Fig 5.3 depicts the active steering pump and wiring in the vehicle's front axle. The control structure was implemented using dSPACE Auto-box on the electric vehicle. As mentioned, the yaw rate of the vehicle can be measured using the IMU system. The lateral and longitudinal velocities that are used to calculate the sideslip angle and slip ratio are obtained using GPS, as shown in Fig 4.9. Performing severe maneuvers in experimental studies are considered risky, so these maneuvers are simulated. The simulations have been conducted using a high-fidelity CarSim [90] model provided by GM car company to represent the vehicle response to closed-loop control system. The control structure has been implemented in the MATLAB/Simulink [91] environment. Required feedback signals in control structure such as yaw rate, vehicle longitudinal and lateral velocities, and wheel rotational speeds can be obtained from CarSim.

Fig 5.3 AFS actuation system on electric GM Chevrolet Equinox

The MPC prediction/control horizon and sampling time that have been utilized in the following simulation and experimental evaluations are considered to be:

- *Control system sample time:* $T_s = 0.005$
- *Number of points in MPC control/prediction horizon:* $N = 4$

The simulations and experimental results that were performed during the tuning phase of the controller indicated that the control/prediction horizon and sampling time presented above produce a satisfactory dynamic anticipation prediction of vehicle response. The proper tuned weights of the MPC high-level and HCC low-level modules are illustrated in Table 5.1. According to Eq. (3.7), the weight matrices $\bar{L}$ and $\bar{R}$ are formed by L and R matrices defined as weights on vehicle dynamic states and control input in the MPC reference tracking optimization problem. In this chapter, L and R can be presented as:

$$L = diag(L_v, L_r, L_\psi, L_{\lambda_{max}}) \tag{5.13a}$$

$$R = diag(R_{F_{x_f}}, R_{F_{x_r}}, R_{G_z}, R_\theta) \tag{5.13b}$$

Table 5.1 Tuned weights of proposed control system via combined torque and steering adjustments

High and low level control weights	Parameter	Value
Weight on lateral velocity control in MPC	L_v	5
Weight on yaw rate tracking control in MPC	L_r	50
Weight on yaw angle control in MPC	L_ψ	1000
Weight on maximum slip ration control in MPC	$L_{\lambda_{max}}$	300
Weight on front axle longitudinal force adjustment in MPC	$R_{F_{x_f}}$	1e-5
Weight on rear axle longitudinal force adjustment in MPC	$R_{F_{x_r}}$	1e-5
Weight on yaw moment adjustment in MPC	R_{G_z}	8e-8
Weight on steering adjustment in MPC	R_θ	15
Weight on longitudinal CG force adjustment in HCC	W_{F_X}	1
Weight on lateral CG force adjustment in HCC	W_{F_Y}	1
Weight on CG yaw moment adjustment in HCC	W_{G_Z}	1

The control objective is to preserve the integrated longitudinal and lateral vehicle stability and minimize the deviation of the actual longitudinal and lateral dynamics (wheel slip ratio, lateral velocity, yaw rate, and yaw angle) from desired courses with a combination of front active steering and rear torque vectoring. The control inputs are the required torque adjustments to compensate for CG longitudinal force and yaw moment errors as well as steering adjustment at the front axle to compensate for the lateral force adjustment. In order to examine the performance of the proposed control structure with single or multiple actuation systems, controllers A and B are introduced. Controller A adjusts the front steering and wheel torques using differential braking or rear axle electric motors. A schematic of controller A is shown in Fig 5.1. Controller B adjusts only wheel torques

using differential braking or rear axle electric motors, and a schematic of this controller is shown in Fig 4.1. The tuned weights of controllers A and B are shown in Table 5. 1 and Table 4.3, respectively. It should be noted that in the following figures, subscripts *des*, *A*, *B* stand for desired course, with controller *A* and *B* of the respective signal. In addition, scripts *fl, fr, rl,* and *rr* indicate that the signal is generated at front left, front rear, rear left, and rear right wheels, respectively. Low traction road conditions were obtained naturally by a snow-covered test track during the winter time or with a wet sealer. An approximation of the road surface friction coefficient can be obtained using a straight-line braking maneuver with ABS as discussed in Chapter 4.

5.5.1 Simulation Results via Torque and Steering Adjustments

The presented simulation results in this section are designed to investigate the stability enhancement using combined torque and steering actuation systems. The vehicle response with combined actuators is compared to the single actuator case where only torque adjustments can be considered as a control intervention. In the following simulations, first, an RWD drivetrain layout with an electric motor, and second, an AWD vehicle drivetrain layout with an ABS, are considered.

I. Scenario: A double lane change maneuver on slippery road with constant speed of 60 km/hr

In order to compare the capabilities of controllers A and B in stabilizing the vehicle in the lateral direction, a DLC maneuver is simulated on a slippery road condition with a road friction coefficient of 0.4. The vehicle speed is 60 km/hr initially throughout the driving scenario. The driver steering command in Fig 5.4 shows a harsh DLC maneuver with an amplitude of 3 radians starting from the 1^{st} to 5^{th} second. As stated before, an RWD drivetrain configuration is considered where only rear torque adjustment is practical with controllers A and B. The required torque is generated with two electric motors, each at one corner of the rear axle with the capability of generating ± 1600 N.m.

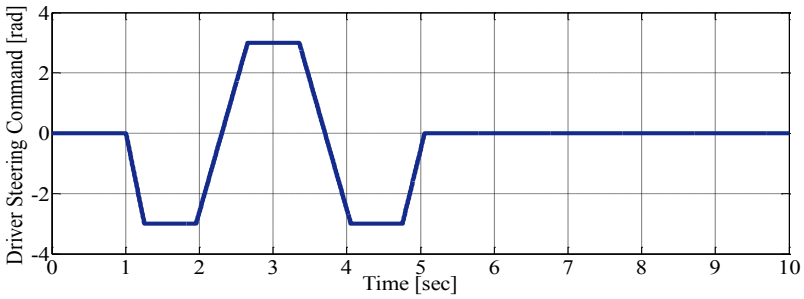

Fig 5.4 Driver steering in a DLC maneuver on wet surface

The vehicle sideslip angle and yaw rate responses are demonstrated in Fig 5.5 and Fig 5.6 for both controllers, respectively. The vehicle sideslip response with controller A is satisfactory as maintained less than approximately 2 degrees on slippery road condition. However, the vehicle sideslip exceeds large values with controller B, which subsequently fails at instability prevention. The yaw rate response is also favorable with controller A as it could follow the desired state. In contrast, the desired yaw rate following is lost after the 3rd second of simulation time with controller B. According to this observation, the vehicle lateral response is enhanced with controller A due to direct lateral slip control. The steering adjustment at the front axle moderates the driver steering command as shown in Fig 5.7. In addition to steering adjustment, rear torque adjustments shown in Fig 5.8 also compensate for CG yaw moment error. According to Fig 5.9, although controller B generated more amount of yaw moment to correct the vehicle lateral response, it was not successful in vehicle stabilization. As shown, control structure modularity, CG based error analysis in the high-level module, and control allocation in the low-level module allow for the proper working of the proposed structure in various configurations with few modifications.

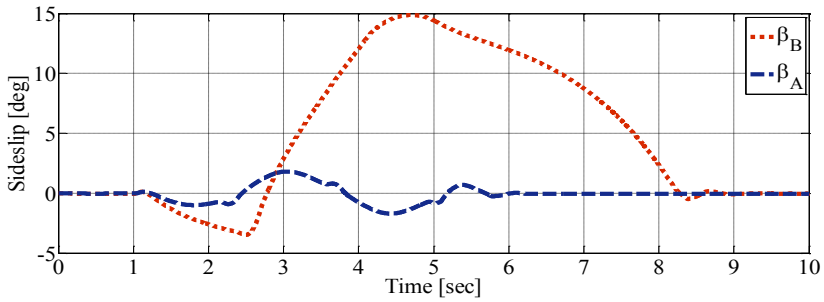

Fig 5.5 Sideslip response comparison of controllers A and B in a DLC maneuver on wet surface

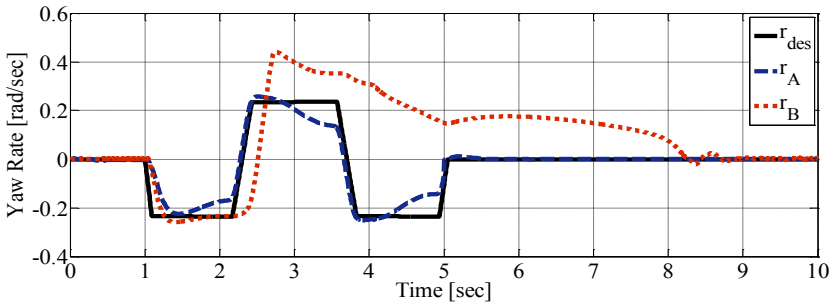

Fig 5.6 Yaw rate response comparison of controllers A and B in a DLC maneuver on wet surface

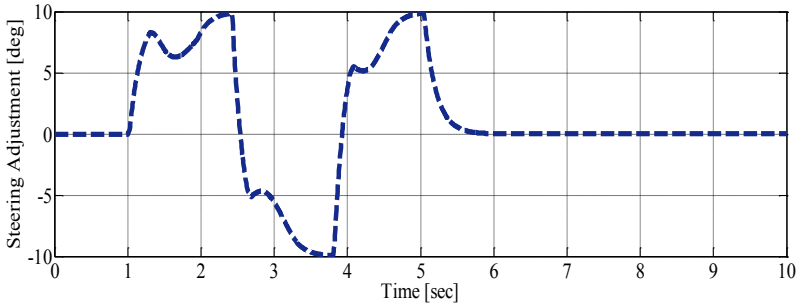

Fig 5.7 Steering adjustment with controller A in a DLC maneuver on wet surface

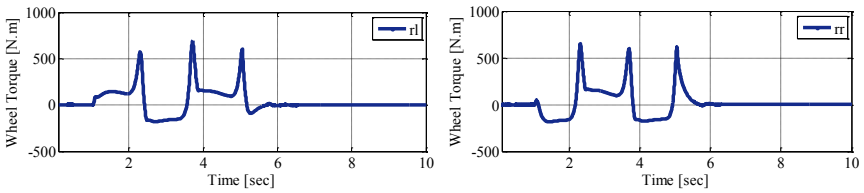

Fig 5.8 Wheel torque adjustment in a DLC maneuver on wet surface with controller A

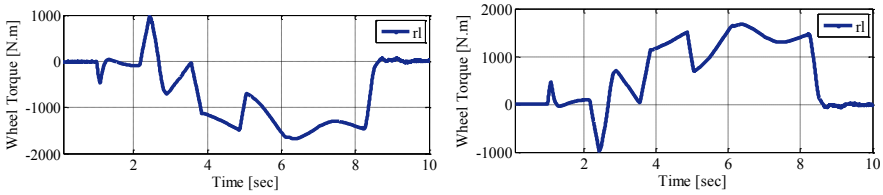

Fig 5.9 Wheel torque adjustment in a DLC maneuver on wet surface with controller B

II. Scenario: A double lane change maneuver on icy road with constant speed of 80 km/hr

Another driving scenario is designed to compare the performance of controllers A and B in lateral vehicle stabilization using a DLC maneuver on an icy road condition with a road friction coefficient of 0.2. The initial vehicle speed is 80 km/hr, which can be considered a relatively high speed. The forward speed is maintained constant during the driving scenario. The driver steering command in Fig 5.8 indicates a DLC maneuver with an amplitude of 1 radian starting from the 1st to 5th second. The steering command in this scenario is not as harsh as the first scenario, however, the scenario is still considered to be severe. This is due to the vehicle performing such a high-speed maneuver on a road with a very low friction coefficient. As stated before, an AWD drivetrain configuration is considered where both front and rear torque adjustment is practical with controllers A and B. The required torque is generated with the ABS.

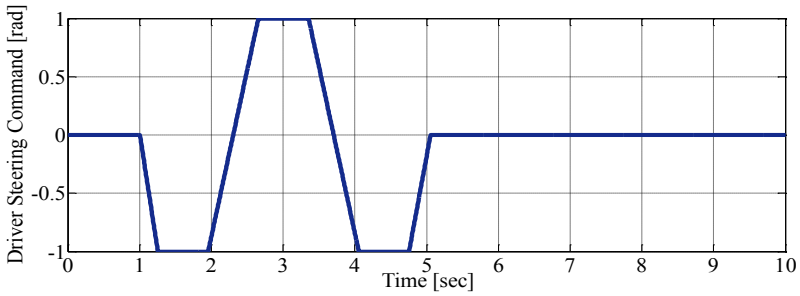

Fig 5.10 Driver steering command in a DLC maneuver on icy surface

The vehicle sideslip angle and yaw rate responses are depicted in Fig 5.11 and Fig 5.12 for both controllers, respectively. The vehicle sideslip response with controllers A and B is satisfactory since it remains within an acceptable range for both (less than 1 degree with controller A and less than 2 degrees with controller B). Although both controllers could maintain lateral dynamics in a safe region, using controller A results in less lateral skidding. The yaw rate responses with both of the controllers illustrate a favorable tracking of the desired state. However, controller A provides less error in the desired maneuverability achievement. Generally, the vehicle's lateral dynamic (sideslip and yaw rate) response is enhanced with steering adjustment. The steering adjustment at the front axle moderates the driver steering command as shown in Fig 5.13. In addition to steering adjustment, differential negative torque adjustments shown in Fig 5.14 also compensate for the CG yaw moment error. A similar trend of torque distribution on the left/right sides does not hold, as the front axle is equipped with an active steering actuator. Fig 5.15 shows more control

intervention with the ABS as the only actuator, which is evidently due to the lack of a steering moderator.

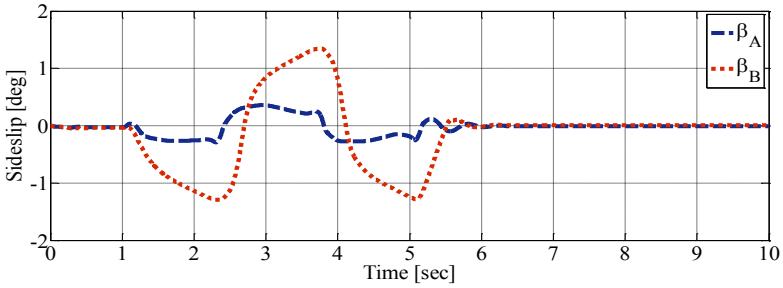

Fig 5.11 Sideslip angle response comparison of controllers A and B in a DLC maneuver on icy surface

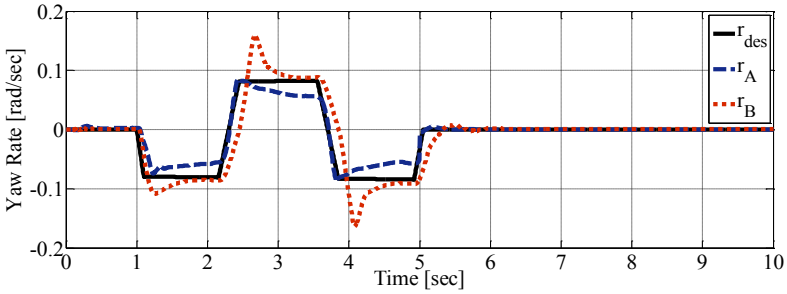

Fig 5.12 Yaw rate response comparison of controllers A and B in a DLC maneuver on icy surface

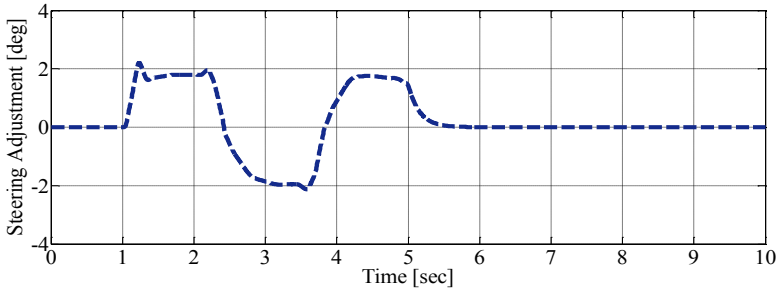

Fig 5.13 Steering adjustment in a DLC maneuver on icy surface with controller A

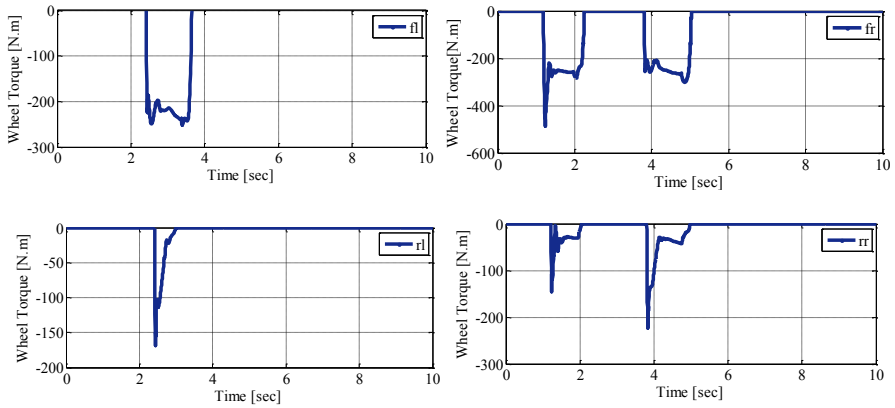

Fig 5.14 Wheel torque adjustment with differential braking in a DLC maneuver on icy surface with controller A

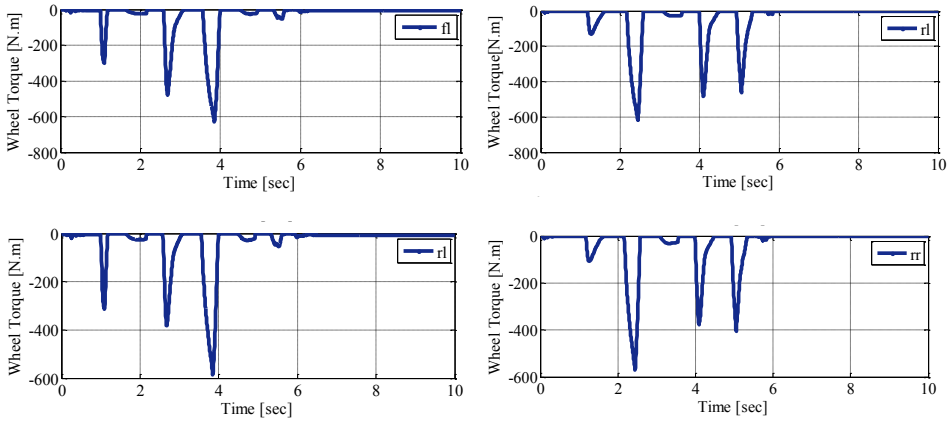

Fig 5.15 Wheel torque adjustment with differential braking in a DLC maneuver on icy surface with controller B

5.5.2 Experimantal Results via Torque and Steering Adjustments

In order to investigate the effect of combined torque vectoring and active steering on vehicle stability control and to validate the competency of an active steering actuator in the experimental setup, two driving scenarios were performed. The maneuvers were executed on different road surfaces (dry and wet). Next, two other driving scenarios will be studied to evaluate the performance of control structure through combined active steering and torque vectoring.

I. Scenario: A slalom maneuver on dry road with initial speed of 40-45 km/hr

A slalom maneuver is designed to investigate the response of an active front steering control system with respect to vehicle lateral dynamic (sideslip and yaw rate) error. In this experiment, the vehicle is only equipped with active front steering control system, and no

other control system is ON. The driving scenario is performed on a dry road condition with an approximate road friction coefficient of 0.9. The initial vehicle speed is 40-45 km/hr as shown in Fig 5.16 and is preserved to be almost constant during the 10 seconds of driving. The driver steering command in Fig 5.17 illustrates a slalom maneuver with an approximate amplitude of 2-3 radians starting from the 1st to 10th second. As the driver turns steering wheel more rapidly, the risk of lateral instability increases.

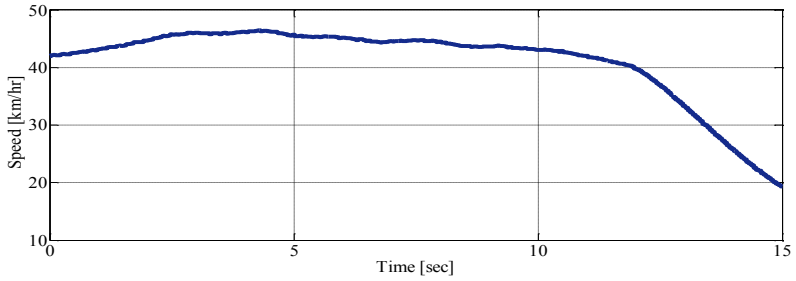

Fig 5.16 Vehicle speed in a slalom maneuver on dry surface

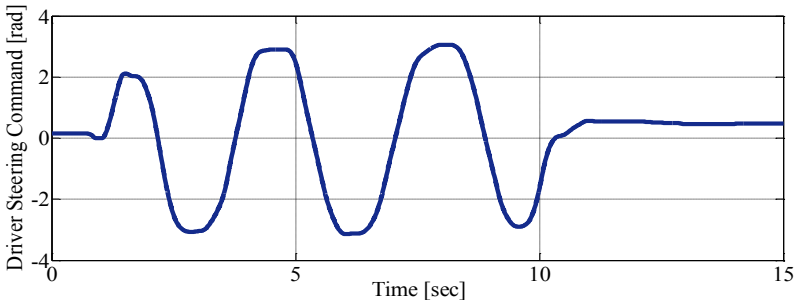

Fig 5.17 Driver steering command in a slalom maneuver on dry surface

The vehicle sideslip and yaw rate responses are reported in Fig 5.18 and Fig 5.19 with an active front steering actuator. The active steering control system provides a satisfactory vehicle sideslip response since it remains less than 2 degrees on a dry road condition. In addition, the actual yaw rate of the vehicle could follow the desired signal properly with only a negligible lag due to the vehicle's enormous body inertia. The error between the actual and desired yaw rate signals resulted in steering adjustment for better reference tracking. According to Fig 5.20, since the lateral plane is less of a concern in such a maneuver on a dry road condition, steering adjustment is devoted to improve steerability and yaw rate error minimization. As soon as the measured yaw rate departed from the desired course, the control system generated a control law to compensate for the error. According to this experiment, the performance of the active front steering actuation system is highly adequate on a dry road condition.

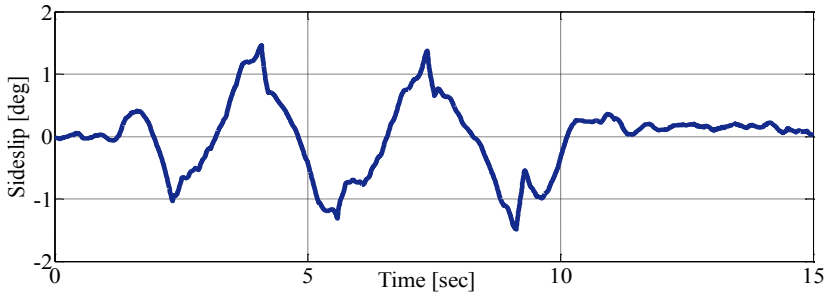

Fig 5.18 Vehicle sideslip response in a slalom maneuver on dry surface (via steering adjustment)

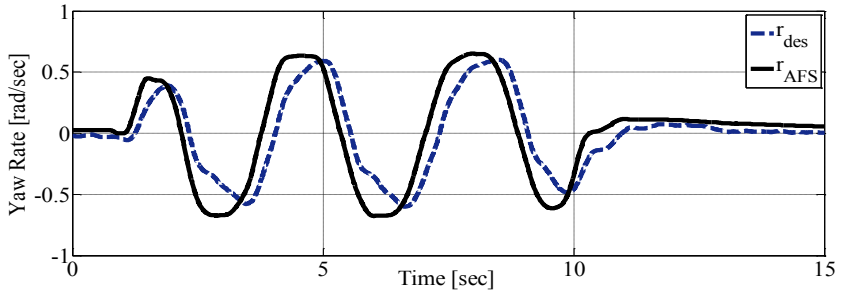

Fig 5.19 Vehicle yaw rate response in a slalom maneuver on dry surface (via steering adjustment)

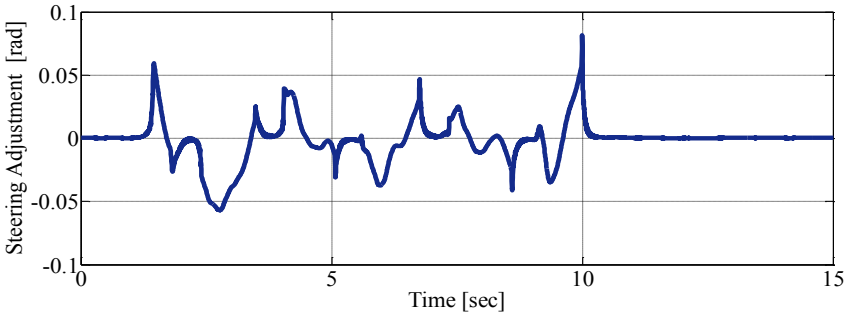

Fig 5.20 Steering adjustment in a slalom maneuver on dry surface

II. Scenario: A double lane change maneuver on slippery road with initial speed of 50 km/hr

In another experiment, a DLC maneuver is designed to investigate the response of an active front steering control system with respect to the vehicle's lateral dynamic (sideslip and yaw rate) error. In this experiment, the vehicle is only equipped with the active front steering control system, and no other control system is ON. The driving scenario is performed on a slippery road condition with an approximate road friction coefficient of 0.4 on wet sealer. The vehicle forward speed at the beginning of the lane change maneuver is approximately

50 km/hr as shown in Fig 5.21. The driver steering command in Fig 5.22 shows a DLC maneuver with an approximate amplitude of 6 radians starting from the 4th to 10th second. This maneuver is considered more challenging from a stability maintenance perspective due to the severity of the lane change and the slippery road surface.

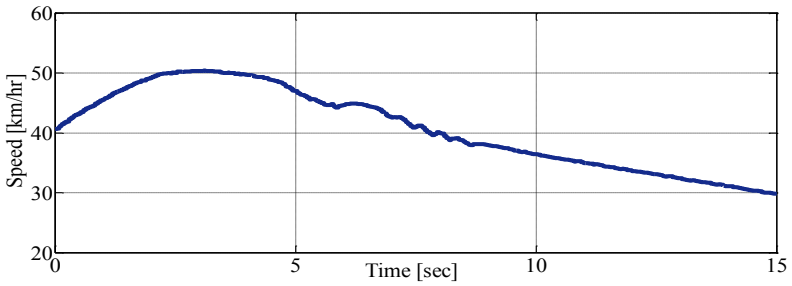

Fig 5.21 Vehicle speed in a DLC maneuver on wet surface

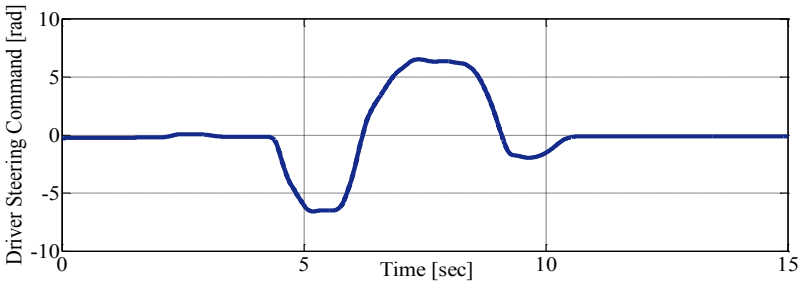

Fig 5.22 Vehicle steering command in a DLC maneuver on wet surface

The vehicle sideslip angle and yaw rate responses are shown in Fig 5. 23 and Fig 5.24 with an active front steering actuator. As the vehicle sideslip was less than 2 degrees on the slippery road condition, it can be concluded that controller was successful in directional control. The actual yaw rate of the vehicle is tracking the desired yaw rate properly with only an insignificant understeer error. As seen in Fig 5.25, the largest interventions occurred when driver turned the steering wheel in the opposite direction to change the lane. According to these test results, it can be concluded that the active front steering actuator can also perform well on a slippery road condition. As the competency of the active front steering actuator is individually proven in the experimental setup, combined steering and torque adjustments are expected to provide a better stability and maneuverability.

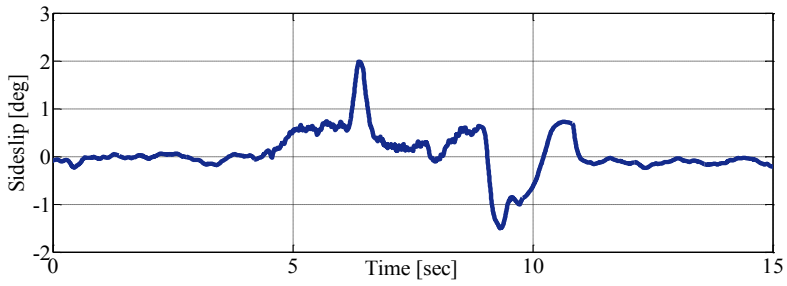

Fig 5.23 Vehicle sideslip response in a DLC maneuver on wet surface (via steering adjustment)

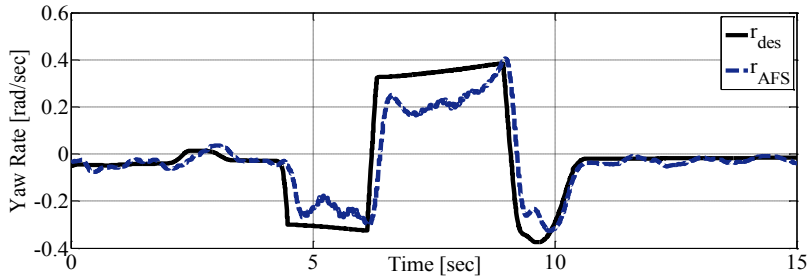

Fig 5.24 Vehicle yaw rate response in a DLC maneuver on wet surface (via steering adjustment)

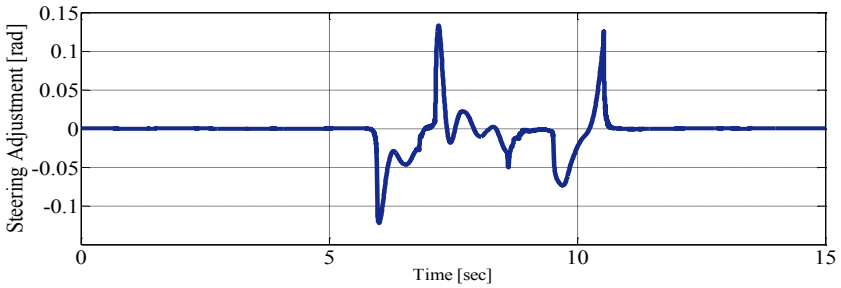

Fig5.25 Steering adjustment in a DLC maneuver on wet sealer

III. Scenario: A slalom maneuver on snowy road with initial speed 40 km/hr

In order to evaluate the performance qualifications of the proposed integrated stability controller using the combined torque vectoring and active front steering on a snowy road with an approximate friction coefficient of 0.3, the vehicle directional response is investigated in a slalom maneuver. In this maneuver, a driver performs multiple lane changes to avoid hypothetical obstacles where the steering command is demonstrated in Fig 5.27. The vehicle speed in this scenario decreases slightly from 40 to 30 km/hr as shown

in Fig 5.26. The drive torque request in Fig 5.28 indicates acceleration at the beginning, and a non-zero (almost) constant throttle input for the rest of the maneuver.

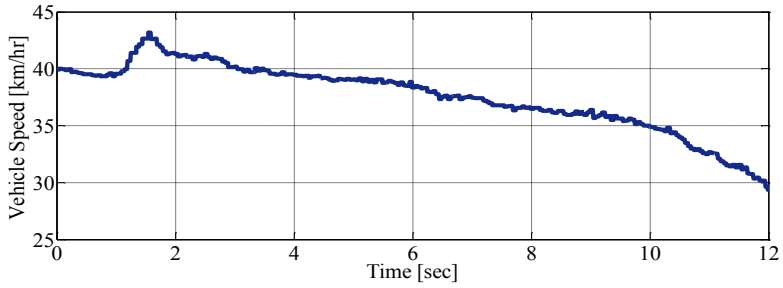

Fig 5.26 Vehicle speed in a slalom maneuver on snowy surface with controller A

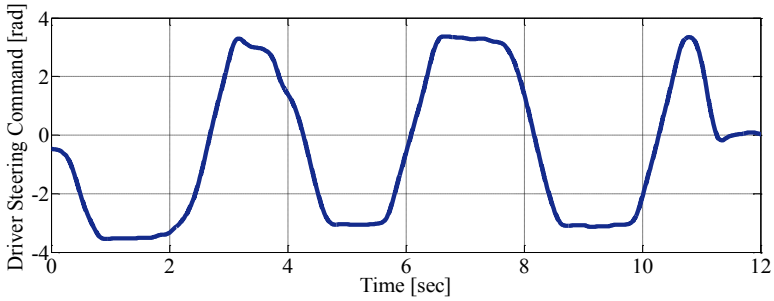

Fig 5.27 Driver steering command in a slalom maneuver on snowy surface with controller A

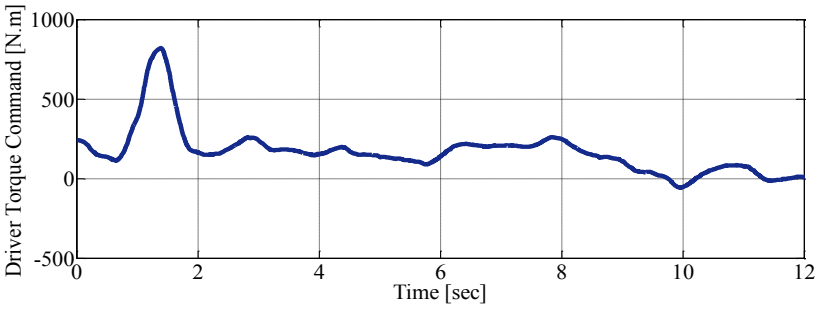

Fig 5.28 Driver torque command in a slalom maneuver on snowy surface with controller A

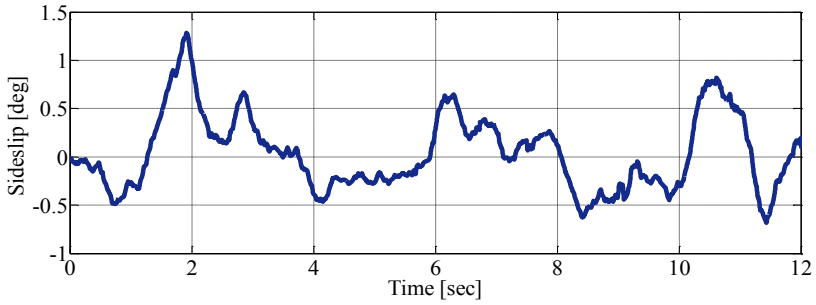

Fig 5.29 Vehicle sideslip response in a slalom maneuver on snowy surface with controller A

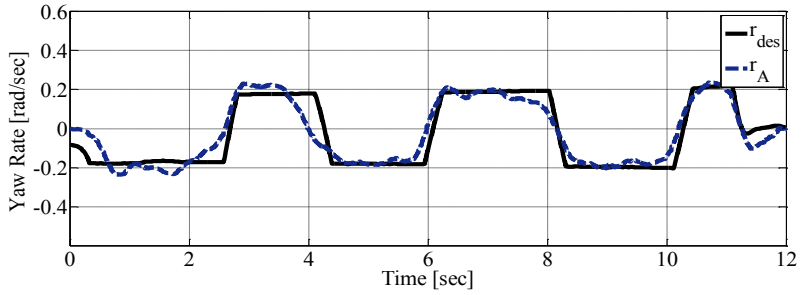

Fig 5.30 Vehicle yaw rate response in a slalom maneuver on snowy road with controller A

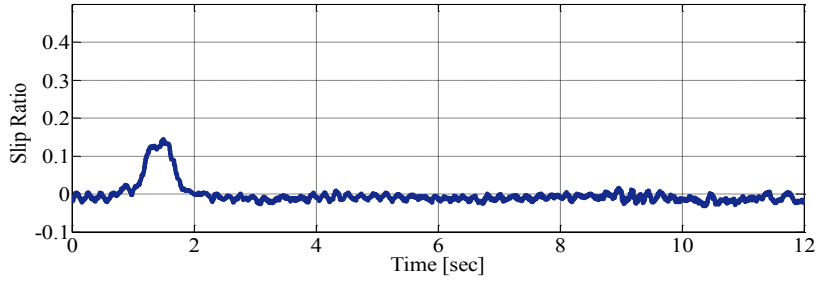

Fig 5.31 Wheel slip ratio in a slalom maneuver on snowy surface with controller A

The vehicle sideslip response shown in the Fig 5.29 reports that the vehicle was under control with a maximum lateral skid of 1.5 degrees. Small amounts of sideslip angle are inevitable since it can be considered necessary for good handling performance and steerability. Fig 5.30 illustrates the vehicle yaw tracking response as a proof of satisfactory maneuverability on a snow-covered road with controller A. The maximum slip ratio in Fig 5.31 shows that the vehicle is stable longitudinally and only at the first second of driving when the driver pushed the gas pedal harshly did the longitudinal slip reach approximately 0.1. The control inputs of such a proposed controller are shown in Fig 5.32 and Fig 5.33.

An RWD drivetrain configuration is considered where only the rear torque adjustment is practical. According to Fig 5.32, a steering adjustment has to be conducted to reduce the driver steering command and minimize the error between the vehicle's actual and desired lateral dynamics. Integrated vehicle stability control resulted in a negative torque adjustment at the first second of driving in the rear right as well as the rear left tires. This is due to is due to acceleration at that moment on the snow-covered road that increases the risk of longitudinal instability and loss of vehicle control. In the rest of the driving scenarios, since the throttle input was not remarkable, and there was no significant slip in the longitudinal direction, the torque adjustments at the left and right sides of the vehicle follow a more symmetric trend. It can be seen that with approximately 200 N.m of yaw moment correction and 0.15 radians of steering correction, the vehicle is maintained stable on a snow-covered road.

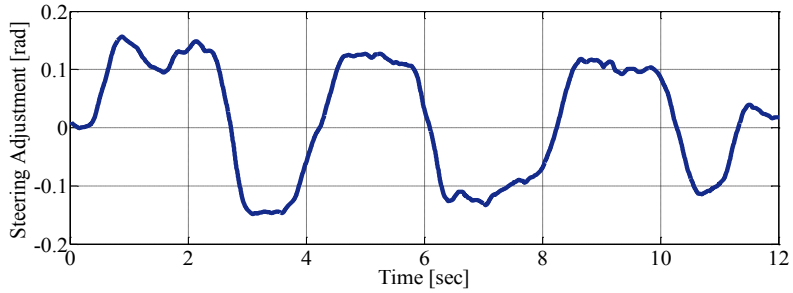

Fig 5.32 Steering adjustment in a slalom maneuver on snowy surface with controller A

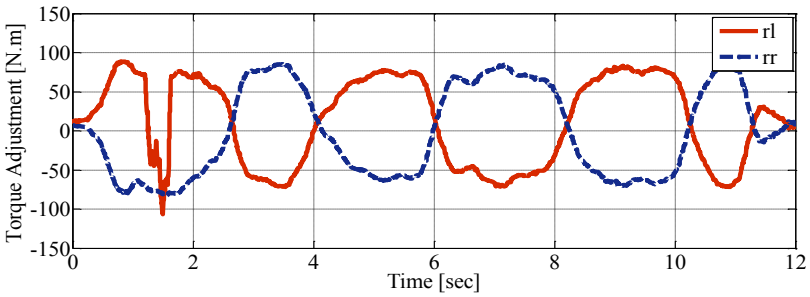

Fig 5.33 Torque adjustment in a slalom maneuver on snowy surface with controller A

In a similar driving scenario, the performance of controller A is compared to controller B where the control technique was rear torque vectoring. The examination has been performed with an approximate initial speed of 40 km/hr as illustrated in Fig 5.34. For a fair comparison, the vehicle speed is maintained between 30 to 40 km/hr until the 8th second

of driving, and then, due to risk of instability, it was decreased drastically. The driver steering command is shown in Figure 5.35, which is similar to the previous driving scenario of the testing of controller A, however, there are slight differences. First, in the second lane change (between the seconds 2-5), the driver steered less rapidly so the vehicle body could synchronize with driver lane-shift command. Second, as the vehicle was not stable after the 7th second of driving, the last lane change could not be completed properly. The driver torque command during this scenario is shown in Fig 5.36, and this indicates gas pedal involvement.

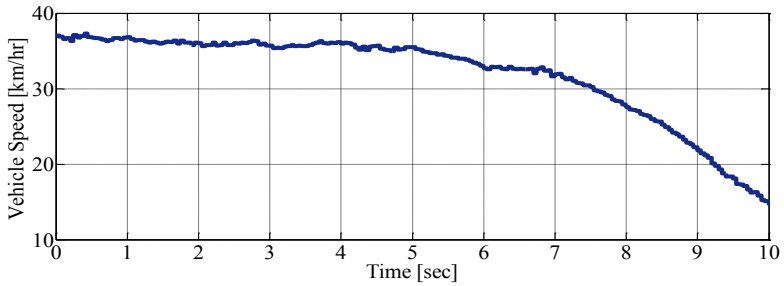

Fig 5.34 Vehicle speed in a slalom maneuver on snowy surface with controller B

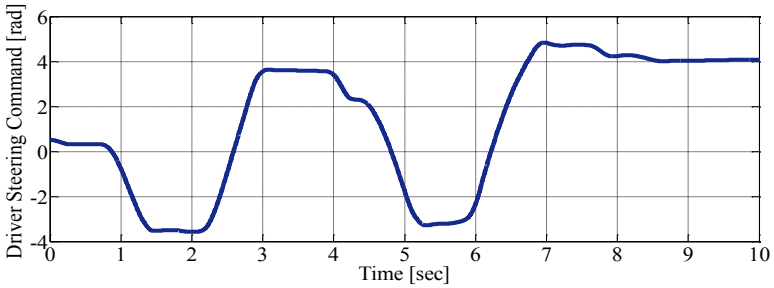

Fig 5.35 Driver steering command in a slalom maneuver on snowy surface with controller B

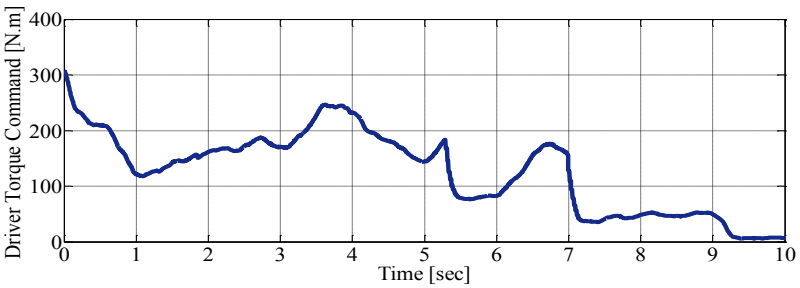

Fig 5.36 Driver torque command in a slalom maneuver on snowy surface with controller B

As depicted in Fig 5.37 and Fig 5.38, the vehicle as not stable laterally in this driving scenario. The vehicle sideslip response depicts that the vehicle skids unfavorably in the lateral direction after 6 seconds on a snow-covered road. The vehicle yaw rate response also shows that the controller was not capable of tracking the desired yaw rate signal after the 5th second of driving. The instability of the vehicle resulted in an oversteer situation and the driver could not complete the last lane change. The torque adjustment with controller B is shown in Fig 5.39. An RWD drivetrain configuration is considered where only a rear torque adjustment is practical. Although the controller generates a larger amount of yaw moment at the rear axle to follow the desired value compared to controller A in a similar maneuver, it was not prosperous enough to stabilize the vehicle.

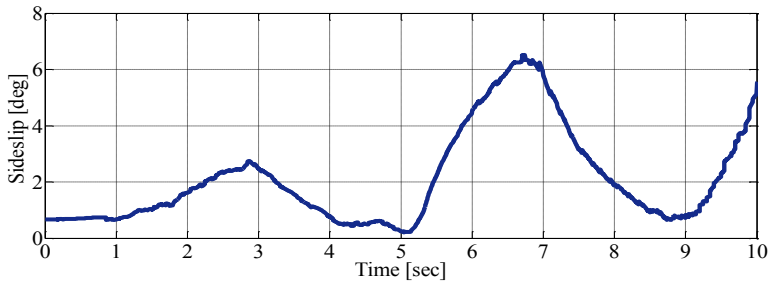

Fig 5.37 Vehicle sideslip response in a slalom maneuver on snowy surface with controller B

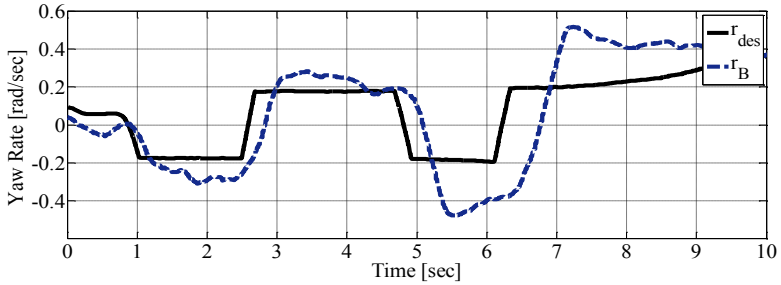

Fig 5.38 Vehicle yaw rate response in a slalom maneuver on snowy road with controller B

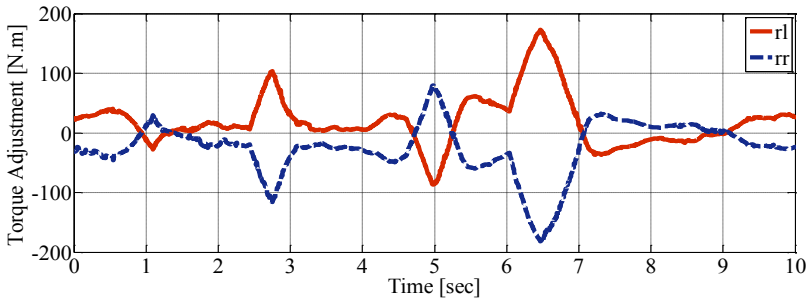

Fig 5.39 Wheel torque adjustment in a slalom maneuver on snowy road with controller B

5.6 Summary

In this chapter, integrated stability control through combined torque vectoring and active steering was studied. A modular control structure was developed with MPC high-level and HCC low-level control modules. The high-level module was responsible of the CG horizontal forces and yaw moment analysis. According to this analysis, required steering and torque adjustments were generated for handling and stability improvement. The low-level control module optimally distributed torque between the corners based on the drivetrain configuration. The real-time performance of the proposed control structure was evaluated in severe critical maneuvers such as the double lane change and slalom on slippery road conditions such as snow/ice covered road. The effect of steering as well as torque moderations with a multi-actuator handling technique was investigated in simulation and experiments. In all of the cases, the closed-loop vehicle performance was compared to the control structure developed in Chapter 4 where only torque adjustments were allowed. Two different methods were used to generate the required torque as differential braking and driving/braking torque vectoring. The results depicted excellent vehicle stability and steerability with the proposed control system in all of the attempted maneuvers. A minor change was made to the control structure and parameters to move from the all-wheel-drive vehicle in Chapter 4 to the rear-wheel-drive vehicle in this chapter.

Chapter 6

Actuation Dynamics Modelling in Low-Level Control Module

6.1 Introduction

Chapters 4 and 5 investigated the integrated (longitudinal and lateral) vehicle stability control, first, through torque adjustment, and second, through coordinated torque and steering adjustments in various actuator and drivetrain configurations. In this chapter, in order to consider the effect of actuation system dynamics on vehicle stability control, the distribution algorithm in the low-level control module is modified with actuator evolution model. Instead of a single-step optimization in the HCC low-level module, a multi-step optimization is proposed to be conducted considering the dynamic development trend of the control action. The proposed multi-step control approach employs a CG based error analysis by the MPC high-level control module. This chapter is organized as follows. Firstly, the novel formulation of the HCC multi-step optimization is discussed. Then, a general methodology that can be used to consider the effect of the actuation system dynamics is discussed and the actuation modelling is shown for a braking system. Finally, simulation and experimental results are illustrated to inquire into the importance of the actuation dynamic effect on vehicle stability control, particularly when the actuation system has a slow dynamics in generation or distribution of the required control intervention.

6.2 General Concept of Multi-Step HCC

A vehicle could not be able to follow the desired dynamics due to many reasons such as the driver's severe steering at high-speeds on a slippery road condition. The error between vehicle's actual and desired dynamics is a result of the discrepancy between the desired and actual CG horizontal forces and yaw moment. In the previous chapters, a high-level control module was designed that provides a CG based error analysis, and a low-level control module was designed to generate and optimally distribute torque between the corners such that the CG error is minimized. The essentials of the corner based HCC

strategy concept that were employed in the low-level control module design was discussed extensively in Chapter 3 and 4. The original HCC that contemplates only vehicle dynamics in distribution of control action has been developed to consider wheel dynamics in Chapter 5. As one of the main objectives of the proposed control structure is coordinating with different actuation systems, the actuator dynamics should be modelled and considered in the optimization process of the low-level control module. If the actuator dynamic is fast enough, the impact of the modelling is less significant, however, for a slow dynamic actuator, the modelling compensates for any delay. The original HCC strategy does not allow for the consideration of such an effect since the optimization process is conducted in a single-step without any knowledge of the evolution trend of the control input. Therefore, a novel multi-step approach is proposed that includes an actuation system dynamics model into consideration during the optimization process. Fig 6.1 shows the proposed modular control structure where the general structure of the controller is almost unchanged and only one additional change has been made to advance the low-level module control algorithm.

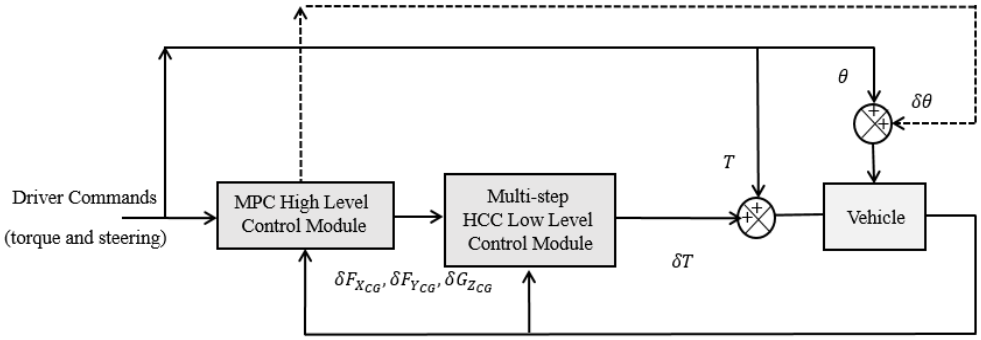

Fig 6.1 Schematic of the proposed control structure with multi-step HCC low-level module

6.3 Multi-Step HCC Formulation

According to HCC method, the stability of vehicle CG can be maintained by adjusting the corner horizontal forces. In order to consider the effect of the actuation system dynamics on the requested control action, instead of a single-step optimization process, a multi-step optimization process can be conducted, which is inspired by the MPC theory that is model-based and takes the dynamic future behavior of the system into account while deciding on the current control action. If the error between the actual and desired CG horizontal forces and yaw moments is considered generally as:

$$E = \{E_{F_X}, E_{F_Y}, E_{G_Z}\} \tag{6.1}$$

then, the actual CG horizontal forces and yaw moment can be considered as a function of $\{\delta\mathcal{F}_1, \delta\mathcal{F}_2, \dots, \delta\mathcal{F}_N\}$ in a control horizon with a length of N:

$$E_{F_X} = F_{X_{des}} - F_X(\mathcal{F} + \delta\mathcal{F}_1 + \delta\mathcal{F}_2 + \cdots + \delta\mathcal{F}_N) \tag{6.2a}$$

$$E_{F_Y} = F_{Y_{des}} - F_Y(\mathcal{F} + \delta\mathcal{F}_1 + \delta\mathcal{F}_2 + \cdots + \delta\mathcal{F}_N) \tag{6.2b}$$

$$E_{G_Z} = G_{Z_{des}} - G_Z(\mathcal{F} + \delta\mathcal{F}_1 + \delta\mathcal{F}_2 + \cdots + \delta\mathcal{F}_N) \tag{6.2c}$$

Using a Taylor series expansion similar to Eq. (3.28), one can conclude that the left hand-side of Eq. (6.2) yields:

$$F_{X_{des}} - F_X(\mathcal{F} + \delta\mathcal{F}_1 + \delta\mathcal{F}_2 + \cdots + \delta\mathcal{F}_N) = F_{X_{des}} - \tag{6.3a}$$
$$\left\{F_X(\mathcal{F}) + \frac{dF_X(\mathcal{F})}{d\mathcal{F}}\delta\mathcal{F}_1 + \frac{dF_X(\mathcal{F})}{d\mathcal{F}}\delta\mathcal{F}_2 + \cdots + \frac{dF_X(\mathcal{F})}{d\mathcal{F}}\delta\mathcal{F}_N\right\}$$

$$F_{Y_{des}} - F_Y(\mathcal{F} + \delta\mathcal{F}_1 + \delta\mathcal{F}_2 + \cdots + \delta\mathcal{F}_N) = F_{Y_{des}} - \tag{6.3b}$$
$$\left\{F_Y(\mathcal{F}) + \frac{dF_Y(\mathcal{F})}{d\mathcal{F}}\delta\mathcal{F}_1 + \frac{dF_Y(\mathcal{F})}{d\mathcal{F}}\delta\mathcal{F}_2 + \cdots + \frac{dF_Y(\mathcal{F})}{d\mathcal{F}}\delta\mathcal{F}_N\right\}$$

$$G_{Z_{des}} - G_Z(\mathcal{F} + \delta\mathcal{F}_1 + \delta\mathcal{F}_2 + \cdots + \delta\mathcal{F}_N) = G_{Z_{des}} - \tag{6.3c}$$
$$\left\{G_Z(\mathcal{F}) + \frac{dG_Z(\mathcal{F})}{d\mathcal{F}}\delta\mathcal{F}_1 + \frac{dG_Z(\mathcal{F})}{d\mathcal{F}}\delta\mathcal{F}_2 + \cdots + \frac{dG_Z(\mathcal{F})}{d\mathcal{F}}\delta\mathcal{F}_N\right\}$$

According to the definition of Jacobian matrix $A_{\mathcal{F}}$ in Eq. (3.25), Eq. (6.3) can be rewritten as:

$$\begin{Bmatrix} F_{X_{des}} - F_X(\mathcal{F} + \delta\mathcal{F}_1 + \delta\mathcal{F}_2 + \cdots + \delta\mathcal{F}_N) \\ F_{Y_{des}} - F_Y(\mathcal{F} + \delta\mathcal{F}_1 + \delta\mathcal{F}_2 + \cdots + \delta\mathcal{F}_N) \\ G_{Z_{des}} - G_Z(\mathcal{F} + \delta\mathcal{F}_1 + \delta\mathcal{F}_2 + \cdots + \delta\mathcal{F}_N) \end{Bmatrix} \tag{6.4}$$
$$= E - A_{\mathcal{F}}\delta\mathcal{F}_1 - A_{\mathcal{F}}\delta\mathcal{F}_2 - \cdots - A_{\mathcal{F}}\delta\mathcal{F}_N$$

Now, in order to minimize the aforementioned CG error with the minimum control effort, the following cost function in Eq. (3.30) is revised to conduct a multi-step optimization process:

$$
\begin{aligned}
J^*_{MHCC} = \min_{\delta\mathcal{F}} \; & (E - A_{\mathcal{F}}\delta\mathcal{F}_1)^T W_E (E - A_{\mathcal{F}}\delta\mathcal{F}_1) \\
& + {\delta\mathcal{F}_1}^T W_{d\mathcal{F}} \delta\mathcal{F}_1 \\
& + (E - A_{\mathcal{F}}\delta\mathcal{F}_1 - A_{\mathcal{F}}\delta\mathcal{F}_2)^T W_E (E - A_{\mathcal{F}}\delta\mathcal{F}_1 \\
& - A_{\mathcal{F}}\delta\mathcal{F}_2) + {\delta\mathcal{F}_2}^T W_{d\mathcal{F}} \delta\mathcal{F}_2 + \cdots \\
& + (E - A_{\mathcal{F}}\delta\mathcal{F}_1 - A_{\mathcal{F}}\delta\mathcal{F}_2 - \cdots \\
& - A_{\mathcal{F}}\delta\mathcal{F}_N)^T W_E \big(E - A_{\mathcal{F}}\delta\mathcal{F}_1 - A_f\delta\mathcal{F}_2 - \cdots \\
& - A_{\mathcal{F}}\delta\mathcal{F}_N\big) + {\delta\mathcal{F}_N}^T W_{d\mathcal{F}} \delta\mathcal{F}_N \\
s.t. \quad & LB \le \delta\mathcal{F} \le UB
\end{aligned}
\tag{6.5}
$$

where LB and UB determine the lower and upper bounds for the control action vector in control horizon N. And W_E and $W_{d\mathcal{F}}$ are weight matrices corresponding to the CG error and control input minimizations and can be defined as Eq. (3.31) in Chapter 3. The cost function of the multi-step HCC shown in Eq. (6.5) can be shortened as:

$$
\begin{aligned}
J^*_{MHCC} = \min_{\delta\mathcal{F}} \; & \sum_{k=1}^{N} \left\| E - \sum_{k-1}^{k} A_{\mathcal{F}}\delta\mathcal{F}_k \right\|^2_{W_E} + \|\delta\mathcal{F}_k\|^2_{W_{d\mathcal{F}}} \\
s.t. \quad & \delta\mathcal{F}_{min} \le \delta\mathcal{F} \le \delta\mathcal{F}_{max}
\end{aligned}
\tag{6.6}
$$

Therefore, solving the optimization problem in Eq. (6.6) will result in:

$$
\delta\bar{\mathcal{F}}^* = \{{\delta\mathcal{F}^*}_1, {\delta\mathcal{F}^*}_2, \dots, {\delta\mathcal{F}^*}_N\}^T \tag{6.7}
$$

Similar to the MPC algorithm, at each time step, once the solution to optimizing Eq. (6.6) is found, the first sample of the control input vector is applied to the system and the rest are discarded. In the next time step, the optimization process is repeated for the updated measurements and estimations of the system states and CG error analysis obtained from the high-level control module.

6.4 Solution to Multi-Step HCC Optimization Problem

In order to consider the evolution trend of the control action, the requested or desired control action vector $\delta\mathcal{F}$ should be substituted with actual control action. Assuming that the correlation between the actual and desired control action can be expressed with $\mathcal{G}$ as:

$$
\delta\mathcal{F}_k = \mathcal{G}_k \delta\mathcal{F}_{act_k} \qquad \text{for } k = 1, 2, \dots, \text{N} \tag{6.8}
$$

Then, the optimal control action in Eq. (6.7) can be written as:

$$\delta\bar{\mathcal{F}}^* = \left\{\mathcal{G}_1\delta\mathcal{F}_{act_1}^*, \mathcal{G}_2\delta\mathcal{F}_{act_2}^*, \dots, \mathcal{G}_N\delta\mathcal{F}_{act_N}^*\right\}^T \tag{6.9}$$

Substituting Eq. (6.8) for the control horizon N in Eq. (6.5) will result in:

$$\begin{aligned} J_{MHCC}^* = \min_{\delta\mathcal{F}} & \left(E - A_{\mathcal{F}}\mathcal{G}_1\delta\mathcal{F}_{act_1}\right)^T W_E\left(E - A_{\mathcal{F}}\mathcal{G}_1\delta\mathcal{F}_{act_1}\right) \\ & + \delta\mathcal{F}_{act_1}{}^T\mathcal{G}_1{}^T W_{d\mathcal{F}}\mathcal{G}_1\delta\mathcal{F}_{act_1} \\ & + \left(E - A_{\mathcal{F}}\mathcal{G}_1\delta\mathcal{F}_{act_1} - A_{\mathcal{F}}\mathcal{G}_2\delta\mathcal{F}_{act_2}\right)^T W_E\left(E\right. \\ & \left. - A_{\mathcal{F}}\mathcal{G}_1\delta\mathcal{F}_{act_1} - A_{\mathcal{F}}\mathcal{G}_2\delta\mathcal{F}_{act_2}\right) \\ & + \delta\mathcal{F}_{act_2}{}^T\mathcal{G}_2{}^T W_{d\mathcal{F}}\mathcal{G}_2\delta\mathcal{F}_{act_2} + \cdots \\ & + \left(E - A_{\mathcal{F}}\mathcal{G}_1\delta\mathcal{F}_{act_1} - A_{\mathcal{F}}\mathcal{G}_2\delta\mathcal{F}_{act_2} - \cdots\right. \\ & \left. - A_{\mathcal{F}}\mathcal{G}_N\delta\mathcal{F}_{act_N}\right)^T W_E\left(E - A_{\mathcal{F}}\mathcal{G}_1\delta\mathcal{F}_{act_1}\right. \\ & \left. - A_f\mathcal{G}_2\delta\mathcal{F}_{act_2} - \cdots - A_{\mathcal{F}}\mathcal{G}_N\delta\mathcal{F}_{act_N}\right) \\ & + \delta\mathcal{F}_{act_N}{}^T\mathcal{G}_N{}^T W_{d\mathcal{F}}\delta\mathcal{F}_{act_N}\mathcal{G}_N \end{aligned} \tag{6.10}$$

In order to provide an analytical solution to the multi-step HCC optimization problem in Eq. (6.10), the cost function should be reformed as:

$$J_{MHCC}^* = \min_{\delta\bar{\mathcal{F}}_{act}} \delta\bar{\mathcal{F}}_{act}{}^T\mathcal{H}\,\delta\mathcal{F}_{act} + \mathcal{g}\delta\bar{\mathcal{F}}_{act} \tag{6.11}$$

where, $\delta\bar{\mathcal{F}}_{act} = \left\{\delta\mathcal{F}_{act_1}, \delta\mathcal{F}_{act_2}, \dots, \delta\mathcal{F}_{act_N}\right\}^T$. Eq. (6.10) can be written in a form shown in Eq. (6.11) for control horizon N. To explain the process, an example of a control horizon of N=3 is illustrated as follows:

$$\begin{aligned} J_{MHCC}^* = \min_{\delta\bar{\mathcal{F}}_{act}} & \left\{\delta\mathcal{F}_{act_1}, \delta\mathcal{F}_{act_2}, \delta\mathcal{F}_{act_3}\right\}^T\mathcal{H}\left\{\delta\mathcal{F}_{act_1}, \delta\mathcal{F}_{act_2}, \delta\mathcal{F}_{act_3}\right\} \\ & + \mathcal{g}\left\{\delta\mathcal{F}_{act_1}, \delta\mathcal{F}_{act_2}, \delta\mathcal{F}_{act_3}\right\} \end{aligned} \tag{6.12}$$

where, in the above equation, $\mathcal{H}$ and $\mathcal{g}$ can be defined as:

$$\mathcal{H} = \begin{bmatrix} \mathcal{H}_{11} & \mathcal{H}_{12} & \mathcal{H}_{13} \\ \mathcal{H}_{21} & \mathcal{H}_{22} & \mathcal{H}_{23} \\ \mathcal{H}_{31} & \mathcal{H}_{32} & \mathcal{H}_{33} \end{bmatrix} \tag{6.13}$$

And,

$$\mathcal{H}_{11} = \mathcal{G}_3{}^T A_{\mathcal{F}}^T W_E A_{\mathcal{F}}\mathcal{G}_3 + \mathcal{G}_2{}^T A_{\mathcal{F}}^T W_E A_{\mathcal{F}}\mathcal{G}_2 + \mathcal{G}_1{}^T A_{\mathcal{F}}^T W_E A_{\mathcal{F}}\mathcal{G}_1 + W_{\delta\mathcal{F}}$$

$$\mathcal{H}_{12} = \mathcal{G}_3{}^T A_{\mathcal{F}}^T W_E A_{\mathcal{F}}\mathcal{G}_2 + \mathcal{G}_2{}^T A_{\mathcal{F}}^T W_E A_{\mathcal{F}}\mathcal{G}_1$$

$$\mathcal{H}_{13} = \mathcal{G}_3{}^T A_{\mathcal{F}}^T W_E A_v\mathcal{G}_1$$

$$\mathcal{H}_{21} = \mathcal{G}_2{}^T A_{\mathcal{F}}^T W_E A_{\mathcal{F}} \mathcal{G}_3 + \mathcal{G}_1{}^T A_{\mathcal{F}}^T W_E A_{\mathcal{F}} \mathcal{G}_2$$

$$\mathcal{H}_{22} = \mathcal{G}_1{}^T A_{\mathcal{F}}^T W_E A_{\mathcal{F}} \mathcal{G}_1 + \mathcal{G}_2{}^T A_{\mathcal{F}}^T W_E A_{\mathcal{F}} \mathcal{G}_2 + W_{\delta\mathcal{F}}$$

$$\mathcal{H}_{23} = \mathcal{G}_2{}^T A_{\mathcal{F}}^T W_E A_{\mathcal{F}} \mathcal{G}_1$$

$$\mathcal{H}_{31} = \mathcal{G}_1{}^T A_{\mathcal{F}}^T W_E A_{\mathcal{F}} \mathcal{G}_3$$

$$\mathcal{H}_{32} = \mathcal{G}_1{}^T A_{\mathcal{F}}^T W_E A_{\mathcal{F}} \mathcal{G}_2$$

$$\mathcal{H}_{33} = \mathcal{G}_1{}^T A_{\mathcal{F}}^T W_E A_{\mathcal{F}} \mathcal{G}_1 + W_{\delta\mathcal{F}}$$

$$\mathcal{g} = -\{\mathcal{g}_1, \mathcal{g}_2, \mathcal{g}_3\} \tag{6.14}$$

Furthermore,

$$\mathcal{g}_1 = E^T W_E A_{\mathcal{F}} \mathcal{G}_3 + E^T W_E A_{\mathcal{F}} \mathcal{G}_2 + E^T W_E A_{\mathcal{F}} \mathcal{G}_1$$

$$\mathcal{g}_2 = E^T W_E A_{\mathcal{F}} \mathcal{G}_2 + E^T W_E A_{\mathcal{F}} \mathcal{G}_1$$

$$\mathcal{g}_3 = E^T W_E A_{\mathcal{F}} \mathcal{G}_1$$

The general algorithm to find $\mathcal{H}$ for a control horizon of N can be written in a compact form as:

$$\mathcal{H} = \bar{\mathcal{H}} + \bar{W}_{d\mathcal{F}_{act}} \tag{6.15a}$$

$$\bar{W}_{d\mathcal{F}_{act}} = diag(W_{d\mathcal{F}_{act}}) \tag{6.15b}$$

where elements of $\bar{\mathcal{H}}$ can be obtained from:

$$\bar{\mathcal{H}}(l,n) = \sum_{k=\mathcal{O}(l,n)}^{k=1} \mathcal{G}_k{}^T A_{\mathcal{F}}^T W_E A_{\mathcal{F}} \, \mathcal{G}_{k+|l-n|} \tag{6.16}$$

where $\mathcal{O}$ is a matrix with the definition:

$$\mathcal{O} = \begin{bmatrix} N & N-1 & N-2 & \dots & 1 \\ N-1 & N-1 & N-2 & \dots & 1 \\ N-2 & N-2 & N-2 & \dots & 1 \\ \vdots & \vdots & \vdots & \ddots & \vdots \\ 1 & 1 & 1 & \dots & 1 \end{bmatrix}_{N \times N} \tag{6.17}$$

that is used in the lower bound of the summation in Eq. (6.17). The general algorithm to find $\mathcal{g}$ for a control horizon of N can be written in a compact form as:

$$\mathcal{g} = -\{\mathcal{g}_1, \mathcal{g}_2, \dots, \mathcal{g}_N\} \tag{6.18}$$

where the elements of the above vector can be found as:

$$\mathcal{g}_l = \sum_{k=N-l+1}^{k=1} E^T W_E A_{\mathcal{F}} \mathcal{G}_k \tag{6.19}$$

where l is a counter in the above equation. Therefore, an analytical solution to Eq. (6.11) can be found as:

$$\delta\mathcal{F}^* = -\frac{1}{2}\mathcal{H}^{-1}\mathcal{g} \tag{6.20}$$

6.5 Actuation System Dynamic Modelling

According to Eq. (6.11), the effect of the actuation dynamics and its evolution trend can be considered in the optimal allocation algorithm. In order to consider such an effect, the dynamic behavior of the actuation system should be predicted for a finite control horizon. Prediction of the actuation dynamic behavior is possible by employing a mathematical description of the system. Consider a force actuation system described with a first-order difference equation as:

$$\delta\mathcal{F}_{act_{k+1}} = \Gamma(\delta\mathcal{F}_{act_k}, \delta\mathcal{F}_k) \tag{6.21}$$

The difference Eq. (6.21) with $\delta\mathcal{F}_{act}(0) = \delta\mathcal{F}_{act_0}$ has a unique solution for $k \geq 0$. The solution can be easily found using successive substitution. Assume that we know $\delta\mathcal{F}_{act_k}$ and $\delta\mathcal{F}_k$at time k, so we can calculate $\delta\mathcal{F}_{act_{k+1}}$ using Eq. (6.21). The model in Eq. (6.21) is said to be linear if $\Gamma(\delta\mathcal{F}_{act_k}, \delta\mathcal{F}_k)$ is a linear function of $\delta\mathcal{F}_{act_k}$ and $\delta\mathcal{F}_k$ as:

$$\delta\mathcal{F}_{act_{k+1}} = \bar{A}\delta\mathcal{F}_{act_k} + \bar{A}\delta\mathcal{F}_k \tag{6.22a}$$

$$Y = \delta\mathcal{F}_{act_k} \tag{6.22b}$$

where $\bar{A}$ and $\bar{B}$ are discretized system matrices at time step k, respectively. Also, Y is the output equal to the actual generated by actuator. This equation allows us to anticipate the linear dynamic response of any actuation system in the future such as braking, steering, or limited slip differentials with a dynamic delay. The time-domain solution of Eq. (6.22) can be presented as:

$$\delta\mathcal{F}_{act_k} = \bar{A}^k \delta\mathcal{F}_{act_0} + \sum_{l=0}^{l=k-1} \bar{A}^{k-l-1}\bar{B}\delta\mathcal{F}_l \quad \text{for } k = 1, \dots, N \tag{6.23}$$

where $\delta\mathcal{F}_{act_0}$ is measured/estimated at each sampling time. The correlation between the actual and desired control action of actuation in Eq. (6.8) can be written at each sampling time k as:

$$\mathcal{G}_k = (ZI - A_k)^{-1}B_k \tag{6.24}$$

6.6 Electrohydraulic Brake System Modelling

In order to illustrate the impact of the actuation system modelling on the performance of the HCC optimal distributor, an electrohydraulic braking actuator as the ABS-6 is utilized. This type of system adds valves and small displacement pumps in-line with the existing brake hoses such that the pressure to the wheels can be altered. Fig 6.2 shows an example of a typical ABS layout. The brake booster and master cylinder in this figure are combined with the ABS modulator, which centralizes all components in one unit. During normal operation, the force and displacement on the pedal, exerted by the driver, lead to brake pressure in the brake lines in the same way as the conventional brake system. Particular interferences are performed when the wheel locks under braking. At that moment, the ABS control module sends a control signal to the relevant valve to reduce the brake pressure slightly to let the wheel rotate, and then conveys brake pressure as much as possible without locking.

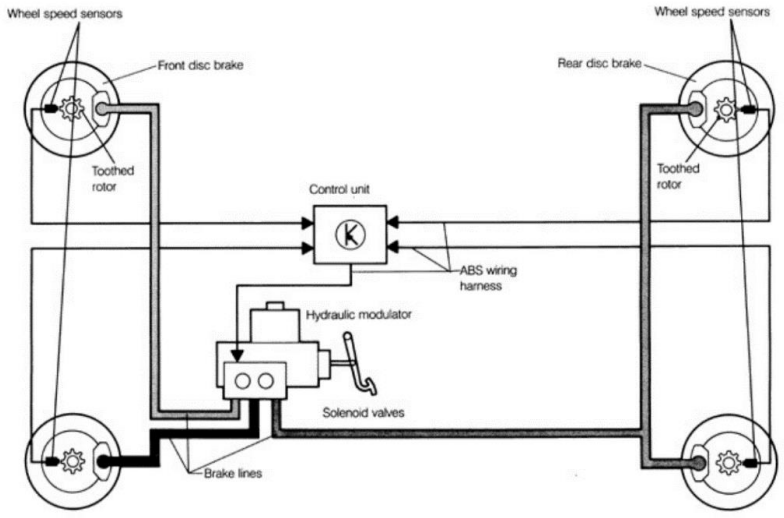

Fig 6.2 Global overview of an ABS system with key components [92]

The corresponding electrohydraulic brake system response to the step input used in our experimental and simulation studies is shown in Fig 6.3. The brake pressure reaches 98%

of the (desired) final pressure in approximately 300 milliseconds. The actuator dynamics are represented by a Zero-Order-Hold (ZOH) discrete transfer function as below [93]:

$$\mathcal{G}_k = \frac{1 - e^{T_s/\tau}}{Z - e^{T_s/\tau}} \tag{6.25}$$

where T_s and τ are the sampling time duration and time-constant of the brake system, respectively. As the signal reaches 98% of the final desired value, a reasonable estimate of the response time equal to four time-constants can be assumed.

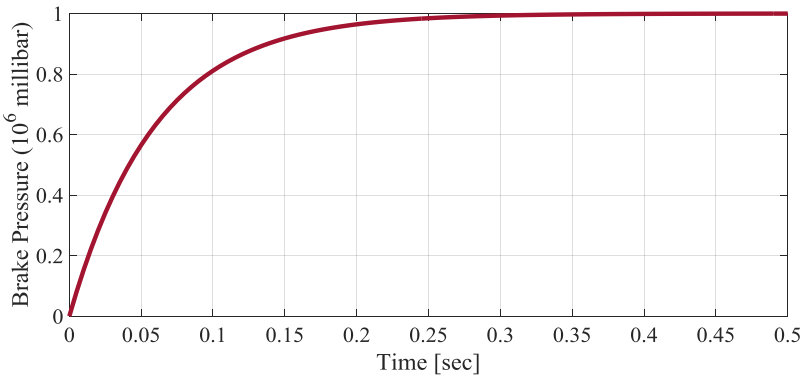

Fig 6.3 Electrohydraulic brake system response to step input

6.7 Simulation and Experimental Results with Actuator Delay Consideration

In order to illustrate the impact of the actuation system modelling on the performance of the HCC optimal distributor, a GM RWD Equinox equipped with an electrohydraulic ABS-6 is utilized. In this section, the performance of the single-step HCC optimal distributor is compared to the modified multi-step one. The simulation and experimental tests evaluate the performance of the proposed control algorithm and compare it to the original algorithm that neglects the actuation dynamic effect. Step steering, double lane change, and slalom maneuvers are performed on slippery road conditions that are discussed in detail in the following sections. The actuation modelling parameters are shown in Table 6. 1.

Table 6.1 Actuation Modelling Parameters

Parameter	Value
Actuator response sampling time	20 ms
Optimization sampling time	5 ms
Optimization control horizon	15
Actuation time constant	75 ms

In order to capture the actuation dynamics effect on the control action, the control horizon should be long enough, however, for an optimization problem such as the one studied in this research, the control horizon is typically chosen to be computationally feasible for real-time implementation. Simulations that were performed during the tuning phase of the controller indicated that the presented control horizon in Table 6.1 produces a proper observation of actuator behavior that results in an adequate controller performance. The implementation of this controller is feasible using an embedded software platform such as dSPACE, which has been proven to work with systems of similar scale and sample time. The vehicle main properties are listed in Table 4.2 in Chapter 4. The HCC optimal distributor presented in Chapter 3 is used here as a baseline. The error in HCC optimal distributor cost function illustrated in Eq. (3.27) only considers yaw moment adjustment in the following tests as:

$$E = \begin{Bmatrix} 0 \\ 0 \\ \delta G_Z \end{Bmatrix}_{CG} \tag{6.26}$$

The yaw moment error is a function of the vehicle's dynamic state errors, and more specifically, lateral velocity and yaw rate errors at each sampling time as:

$$\delta G_Z = \varphi_r e_r + \varphi_v e_v \tag{6.27}$$

where φ_r and φ_v are gains on a defined state error (deviation of a particular dynamic state from its desired value). The yaw rate and lateral velocity errors can be written as:

$$e_r(k) = r_{des}(k) - r(k) \tag{6.28a}$$

$$e_v(k) = v_{des}(k) - v(k) \tag{6.28b}$$

where φ_r =2000 and $\varphi_v = 10$ are tuned weights in the following tests. The reason behind using a simple proportional error instead of an MPC based one is to evaluate the

effectiveness of the MHCC controller on the overall control performance with a delayed actuator. The error in the MHCC optimal distributor cost function is also considered to be the same as in Eq. (6.27) to provide a fair ground for comparison of multi-step versus single-step optimization. In the following tests, the HCC and MHCC optimal distributors are called controllers A and B for simplicity, respectively.

6.7.1 Simulation Results with Actuator Dynamics Consideration

The proposed MHCC algorithm is evaluated using simulations in a MATLAB/Simulink environment. The simulations have been performed using a high-fidelity CarSim [90] model provided by GM car company to represent the response of a GM RWD Equinox vehicle equipped with a hydraulic brake system to a closed-loop control system. Required feedback signals in control structure such as yaw rate, vehicle longitudinal and lateral velocities, and wheel rotational speeds can be obtained from CarSim.

I. Scenario: A step steer on packed snow with initial speed of 80 km/hr

The system is first tested in a step steering maneuver using a CarSim RWD GM Equinox vehicle model that is equipped with a hydraulic brake system with a time-constant of 75 milliseconds. The driving scenario has been performed on packed snow with an approximate road friction coefficient of 0.3. The driver steering command with a maximum amplitude of 1 rad is shown in Fig 6.4. The driving scenario started with a forward speed of 80 km/hr, as shown in Fig 6.5, and does not change remarkably during the driving scenario.

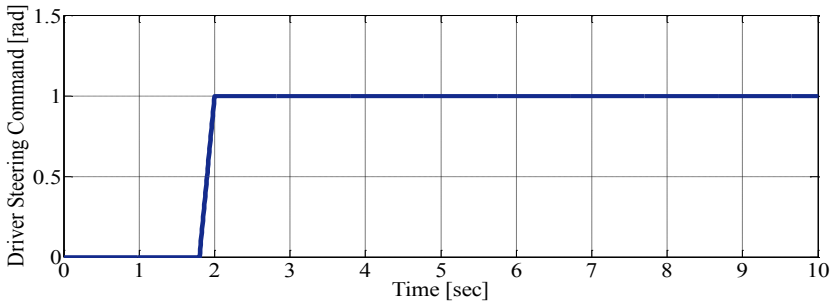

Fig 6.4 Driver steering command in a step steer maneuver on snowy surface

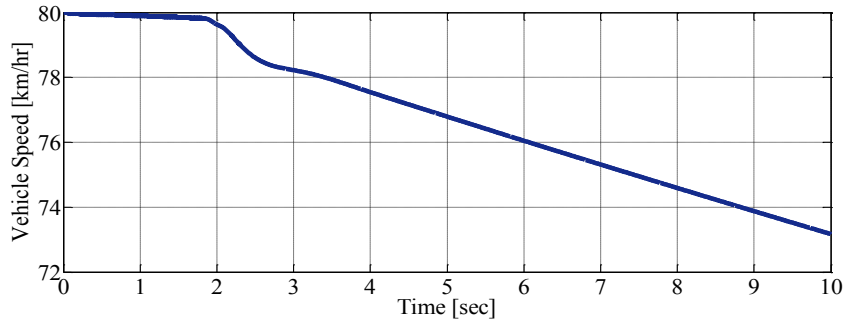

Fig 6.5 Vehicle Speed in a step steer maneuver on snowy surface

The performance of controllers A and B are compared to each other in terms of yaw rate and sideslip dynamic responses. The yaw rate response of the vehicle in Fig 6.6 shows that the vehicle could not follow the desired yaw rate in the uncontrolled case. However, both of the controllers could enable the vehicle to follow the desired maneuverability with some errors. According to this figure, the yaw rate response of the vehicle with controller B that takes actuation dynamics into account while deciding on control action provides less yaw tracking error. Fig 6.7 reports that the vehicle was not laterally stable in the uncontrolled case. However, both controllers A and B could prevent large lateral skidding. Comparison of the sideslip responses with controllers A and B proves that controller B is superior to controller A in lateral stability enhancement as well as maneuverability.

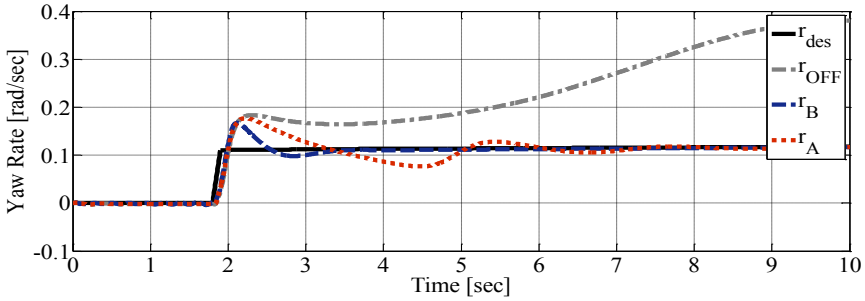

Fig 6.6 Yaw rate response comparison of controllers A and B, and uncontrolled case in a step steer maneuver on snowy surface

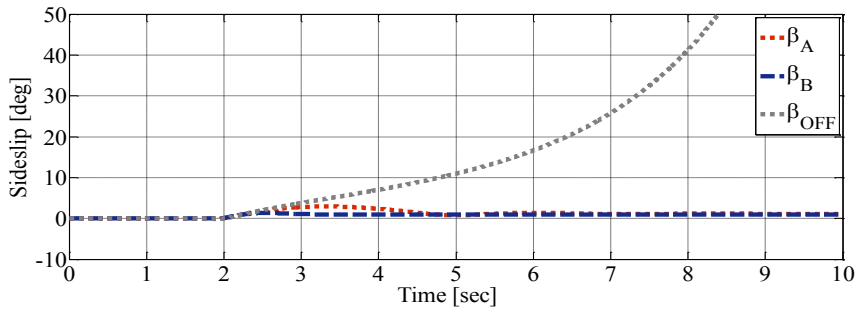

Fig 6.7 Sideslip response comparison of controllers A and B, and uncontrolled case in a step steer maneuver on snowy surface

The torque adjustement that has been accomplished at vehicle corners are shown in Fig 6.8. According to this figure, in every vehicle corner, the control action has a larger value with controller B. This is because the same set of tuned weights are used for both of the controllers and controller B is informed of the actuation dynamic delay. Therefore, this controller requests for a greater control action to compensate for the actuator delay leading to a faster desired lateral dynamics capture. The effect of the actuation delay can be diminished by using higher weights in the tuning process, however, tuning may not be sufficient to eliminate this destructive effect.

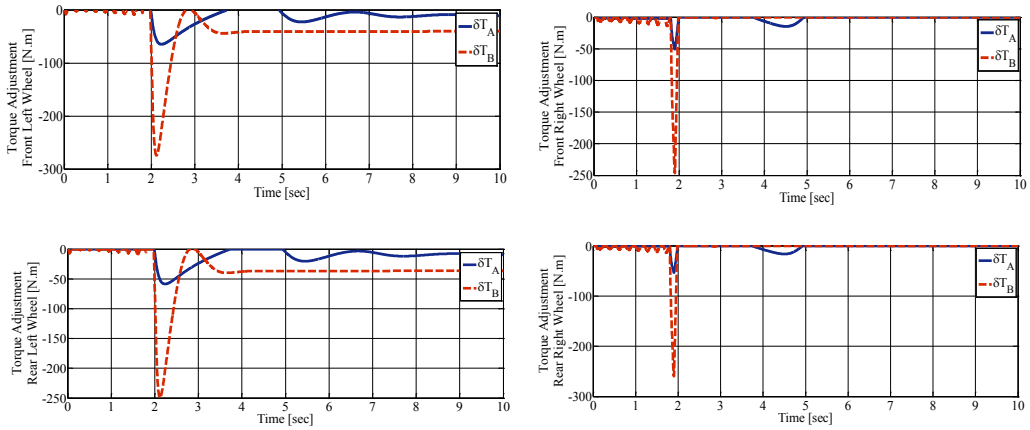

Fig 6.8 Wheel torque adjustment comparison of controllers A and B in step steer maneuver on snowy surface

II. Scenario: A double lane change on packed snow with initial speed of 100 km/hr

In order to evaluate the performance of the controller in a harsher transient condition, a DLC maneuver on packed snow with an approximate friction coefficient of 0.3 is investigated. The driver steering command in this scenario is shown in Fig 6.9, and this has a maximum amplitude of 3 radians. Fig 6.10 shows the vehicle speed, which is initially

100 km/hr. It should be mentioned that during such a severe maneuver, even maintaining the target course roughly can be considered as a success.

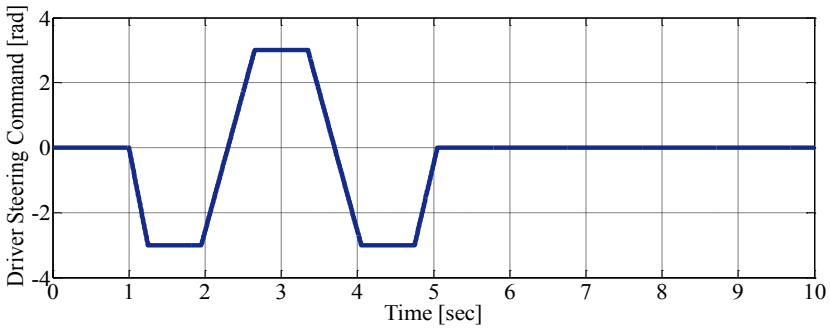

Fig 6.9 Driver steering command in a DLC maneuver on snowy surface

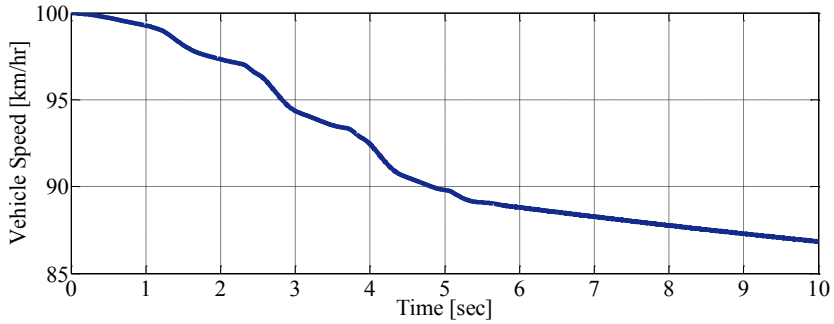

Fig 6.10 Vehicle speed in a DLC maneuver on snowy surface

Fig 6.11 illustrates the vehicle yaw rate response. According to this figure, a significant improvement has been made to the yaw rate response with controller B. As seen with controller A, the vehicle was not able to follow the desired trajectory after the 4th second of driving. The controller depicts more unstable behavior in the uncontrolled case. Fig 6.12 shows the sideslip response of the vehicle that is not under control without controller B.

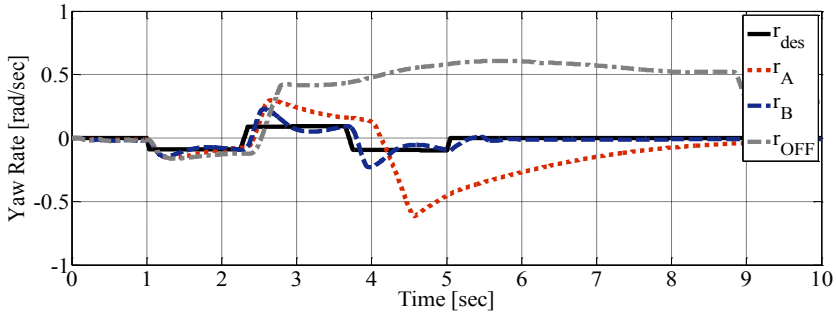

Fig 6.11 Yaw rate response comparison of controllers A and B, and uncontrolled case in a DLC maneuver on snowy surface

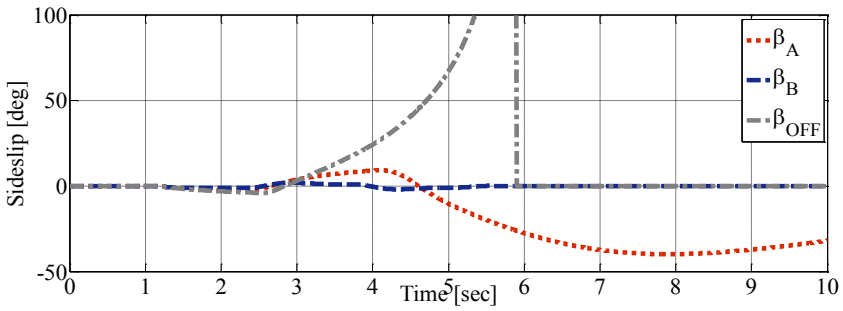

Fig 6.12 Sideslip response comparison of controllers A and B, and uncontrolled case in a DLC maneuver on snowy surface

The torque adjustments of controllers A and B in this scenario are shown in Fig 6.13. Controller B responds more promptly to deviation of the actual dynamic states from the desired ones when considering the peak value of control action in all corners for controllers A and B. A similar trend to the previous driving scenario is seen in this simulation case study as well. The torque adjustments are greater with controller B with the same tuned weights. As discussed, this can be interpreted as an actuator delay consideration effect. Using greater tuned weights may result in better lateral control with controller A, however, it may not compensate for all state errors as it does not inherently consider modelling.

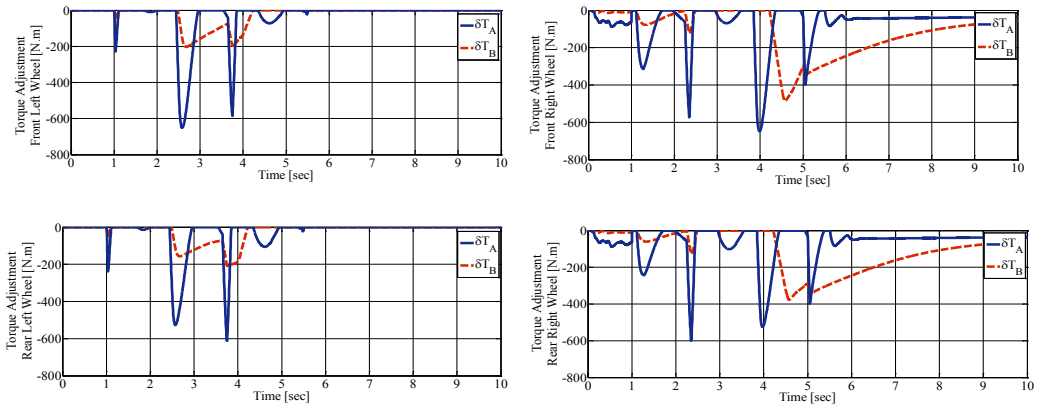

Fig 6.13 Wheel torque adjustment comparison of controllers A and B in a DLC maneuver snowy road

6.7.2 Experiment with Actuator Delay Consideration

For verification purposes, the control system is also implemented on a GM RWD Equinox that is equipped with a hydraulic brake system in real-time. The hydraulic brake system's response to a step input is shown in Fig 6.3. The vehicle platform is shown in Fig 6.14. As previously mentioned, the differential braking system on the vehicle allows for a negative

differential torque adjustment to enhance the vehicle handling performance and lateral stability.

Fig 6.14 GM Equinox platform

I. Scenario: A mild slalom on wet asphalt with initial speed of 40 km/hr with controller B

In order to show the competency of controller B in stabilizing the vehicle in the lateral direction, first, a mild slalom maneuver is designed where driver steering command is shown in Fig 6.15. The driving scenario has been performed on wet sealer that has an adhesion coefficient of approximately 0.4. The vehicle speed is changing between 30 to 40 km/hr, as depicted in Fig 6.16. As seen in Fig 6.17 and Fig 6.18, both yaw rate and sideslip responses of the vehicle with the proposed controller have satisfactory results in handling performance improvement, and achieving the vehicle's desired lateral dynamics on a slippery road condition.

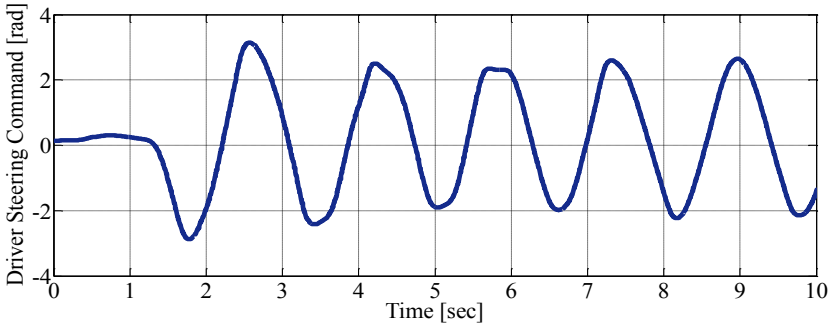

Fig 6.15 Driver steering command in a slalom maneuver on wet surface

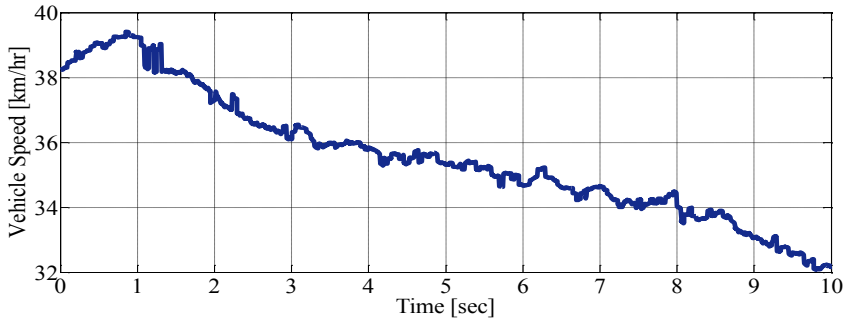

Fig 6.16 Vehicle speed in a slalom maneuver on wet surface

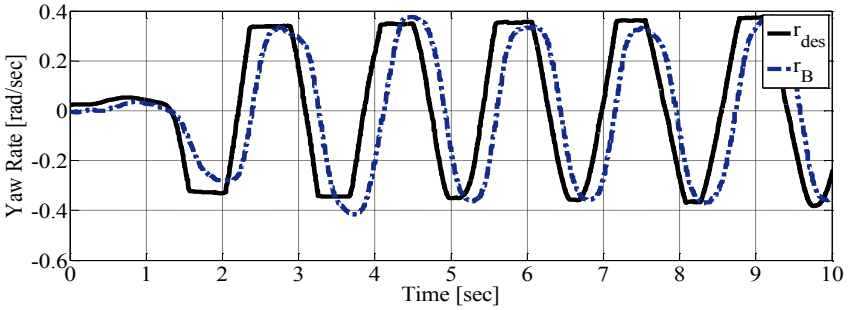

Fig 6.17 Yaw rate response in a slalom maneuver on wet surface with controller B

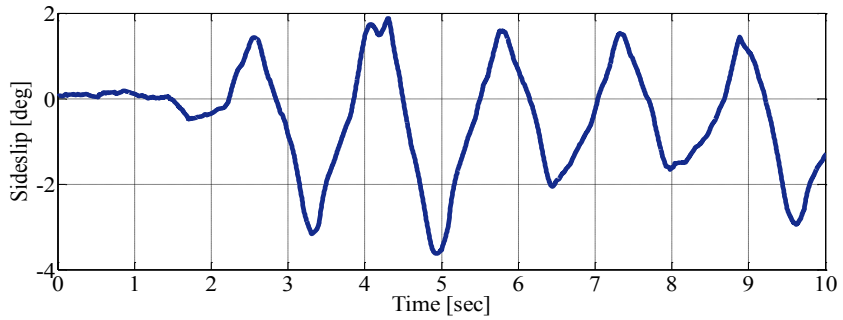

Fig 6.18 Sideslip response in a slalom maneuver on wet surface with controller B

The sideslip angle of the vehicle remains under 4 degrees leading to a stable condition. Fig 6.19 shows that the torque adjustments at the left and right wheels are devoted to generating the required yaw moment to follow the target yaw response as the sideslip angle remains in an acceptable range. As the driver aims to turn left between 1 to 2 seconds of driving, a braking torque is generated in the left wheels of the vehicle to enhance maneuverability during this turning period. However, as soon as the driver changes the turning direction to the right to complete a lane change, a braking torque is generated in the right wheels instead. A relatively consistent trend has been followed that resulted in good vehicle handling.

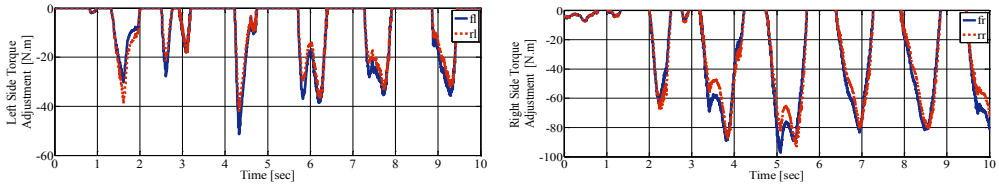

Fig 6.19 Wheel torque adjustment in a slalom maneuver on wet surface with controller B

The generated torque at each corner was constrained to a negative value according to the differential braking actuation bandwidth. As the driving scenario is not a harsh one, the required torque adjustment at the vehicle's corners are not very remarkable. However, the objective of this scenario was to evaluate the performance of the controller in following the desired direction with a reasonable pattern.

II. Scenario: A DLC on wet asphalt with initial speed of 40 km/hr with controllers A and B

In order to investigate the importance of considering an actuation delay effect on proper torque generation and consequently, vehicle controlled handling performance, the experimental results with controller B are compared to ones with controller A. Two double lane change maneuvers with a maximum steering angle of approximately 3-4 radians and vehicle initial speed of approximately 35 km/hr are performed. In the first one, the proposed controller B is activated on the control desk. The driver steering command and vehicle speed are shown in Fig 6. 20 and 6.21 in this scenario. The maneuver is performed on a wet sealer with an approximate road friction coefficient of 0.4. As seen in Fig 6.22 and 6.23, the vehicle could follow the desired yaw rate with minor lateral skidding (less than 2 degrees of sideslip).

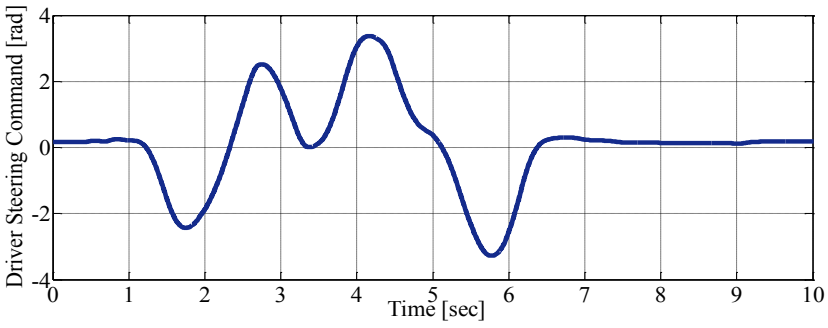

Fig 6.20 Driver steering command in a DLC maneuver on wet surface

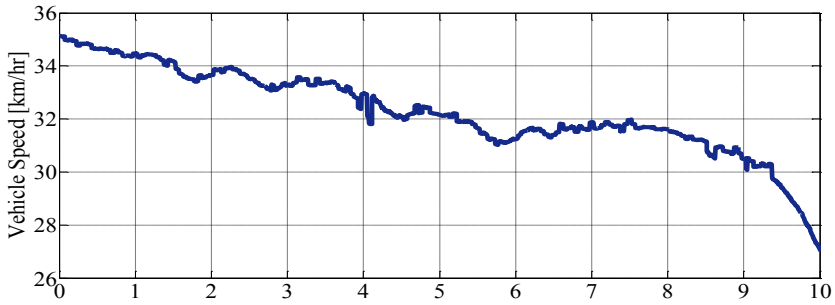

Fig 6.21 Vehicle speed in a DLC maneuver on wet surface

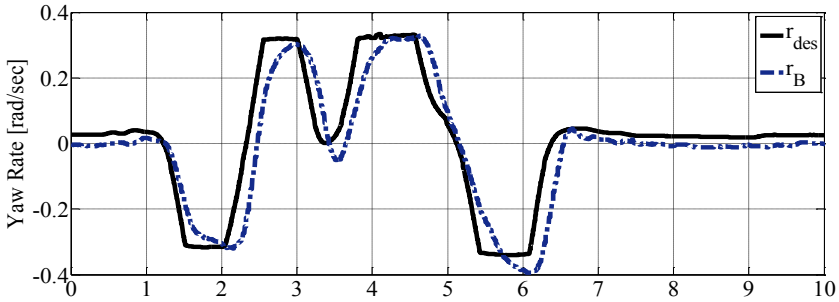

Fig 6.22 Yaw rate response in a DLC maneuver on wet surface with controller B

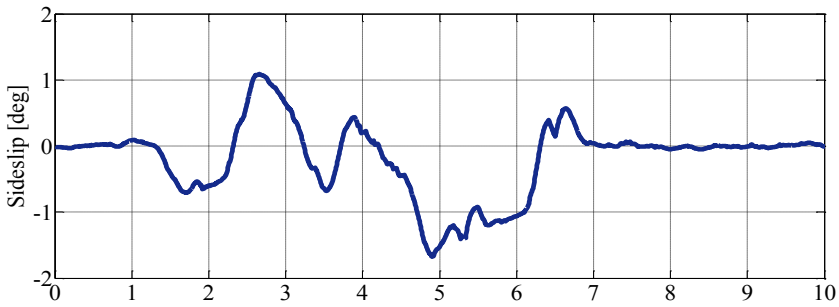

Fig 6.23 Sideslip response in a DLC maneuver on wet surface with controller B

The torque adjustments at the wheels are shown in Fig 6.24. As the driver steering input is more severe in this scenario, the generated yaw moment is greater in comparison with the previous experiment case study. Although the vehicle was equipped with a delayed actuation system, the controller could compensate for this delay and provide a proper performance on the slippery road condition. On the other hand, a similar driving scenario has been performed without considering the actuation delay where controller A was active on the control desk. The driver steering command and vehicle speed are shown in Fig 6.23 and Fig 6.24. A fair comparison could be achieved using a very similar steering command and vehicle speed during a double lane change with both of the controllers.

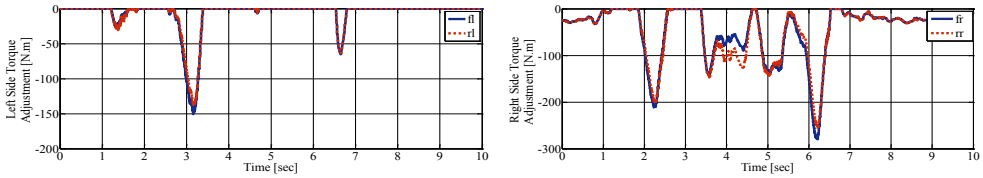

Fig 6.24 Wheel torque adjustment in a DLC maneuver on wet surface

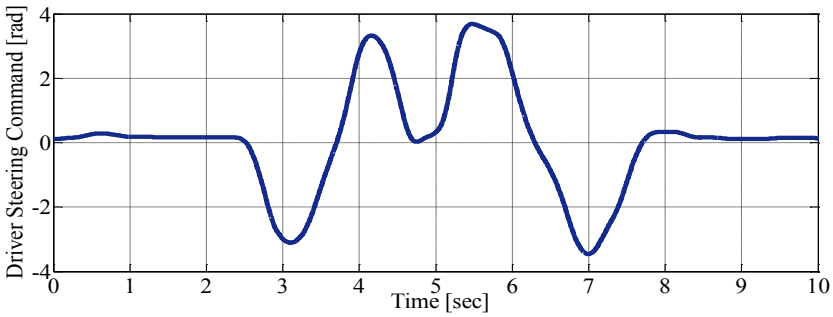

Fig 6.25 Driver steering command in a DLC maneuver on wet surface

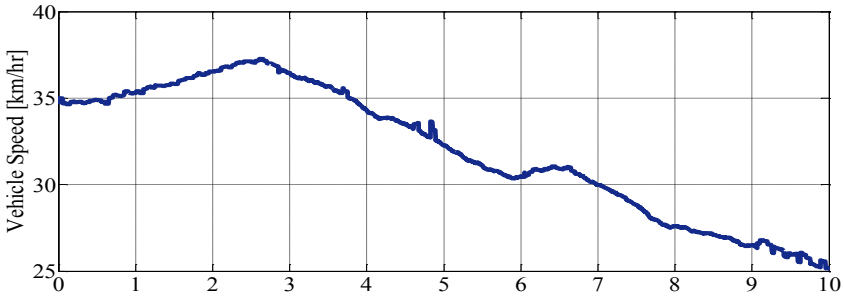

Fig 6.26 Vehicle speed in a DLC maneuver on wet surface

As illustrated in Fig 6.27, although the vehicle remained stable during this maneuver with controller A, it does not show a satisfactory yaw rate tracking response as it noticeably deviates from the desired value between 4-5 seconds of driving. As the effect of the actuator delay has not be considered, it was assumed that the requested torque will be applied to the wheel. However, the requested torque could only be generated after a certain evolution delay that resulted in the deterioration of the vehicle's lateral response. As seen in Fig 6.28, the sideslip angle of the vehicle exceeds 4 degrees during 5-7 seconds of drving that can be interpreted as the vehicle's harsh lateral skidding during these seconds. This scenario verifies the concept that neglecting actuator dynamic delay may deteriorate vehicle controlled handling performance.

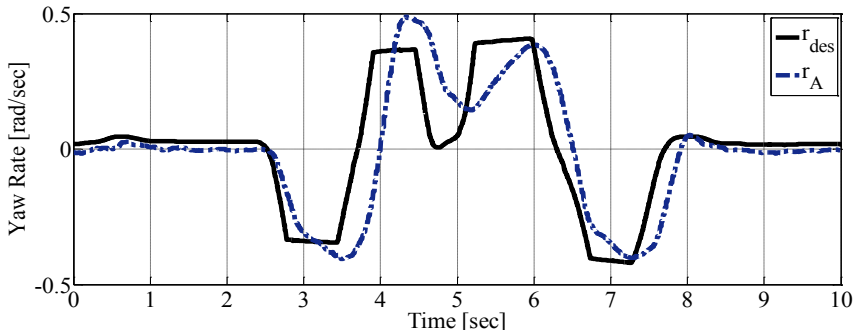

Fig 6.27 Yaw rate in a DLC maneuver on wet surface with controller A

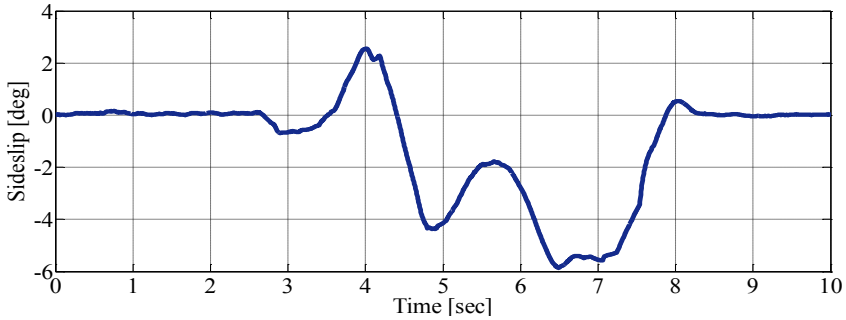

Fig 6.28 Sideslip response in a DLC maneuver on wet surface with controller A

The torque adjustments at each corner during such a maneuver are shown in Fig 6.29. As seen, the generated amount of torque was not sufficient to prevent the vehicle's poor lateral performance. As the sideslip became larger during seconds 5-7 of driving, the controller requested a larger torque adjustment at the right wheels to decrease the lateral skidding, however, its performance, while successful, was poor.

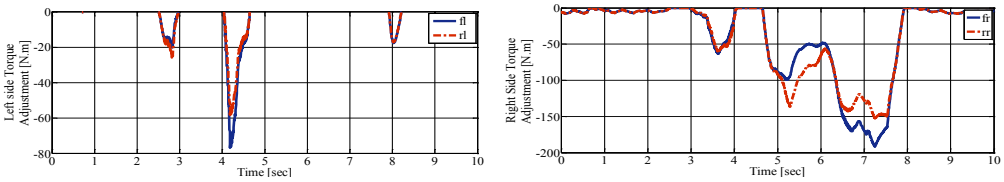

Fig 6.29 Torque adjustment in a DLC maneuver on wet surface with controller A

III. Scenario: A DLC on wet asphalt with initial speed of 40 km/hr with actuation modelling error

An experiment has been designed to investigate the effect of the actuation modelling error, where the driver steering command and vehicle speed are shown in Fig 6.30 and Fig 6.31. It should be noted that in this driving scenario, the actuation dynamic model in controller B design is deliberately inaccurate and imitates an actuator dynamic behavior with 500

milliseconds of delay to reach to 98% of (desired) final value. As seen in Fig 6.32, the yaw rate response of the vehicle leads to understeering, which is due to aggressive torque adjustments. The sideslip response of the vehicle also indicates that the controller was more conservative in stability control.

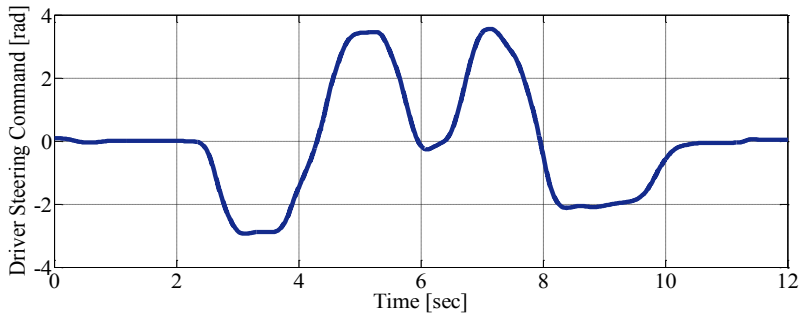

Fig 6.30 Driver steering command in a DLC maneuver on wet surface

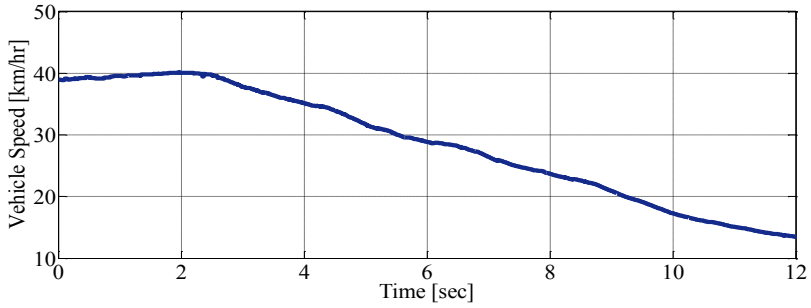

Fig 6.31 Vehicle speed in a DLC maneuver on wet surface

The torque adjustment at each corner shown in Fig 6.34 depicts greater control actions in comparison with the similar driving scenario with controller B in the previous experimental case study. The reason is that the inaccurate actuation modelling resulted in a larger delay compensation and more aggressive control response. In case of actuation delay neglection, a similar response as a previous scenario with controller A should be seen. Therefore, it can be concluded that with a sluggish actuation system, considering the dynamic delay provides a noteworthy improvement in handling performance. Whereas, underestimated (or overestimated) delay assumptions may lead to the vehicle's loss of control or conservative vehicle dynamic response.

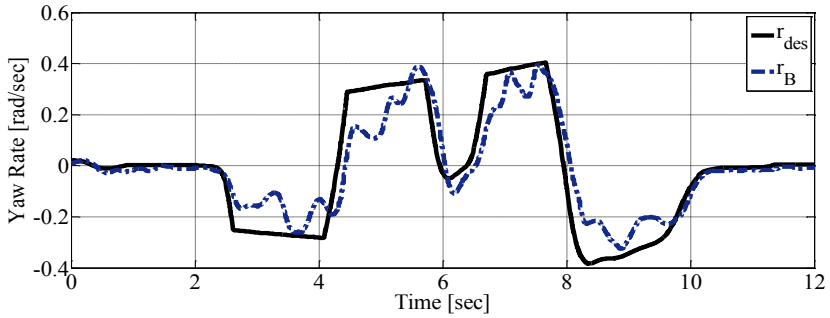

Fig 6.32 Yaw rate response in a DLC maneuver on wet surface with modelling error

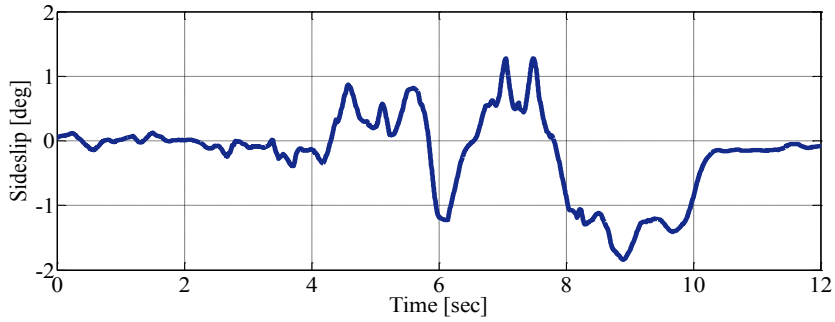

Fig 6.33 sideslip response in a DLC maneuver on wet surface with modelling error

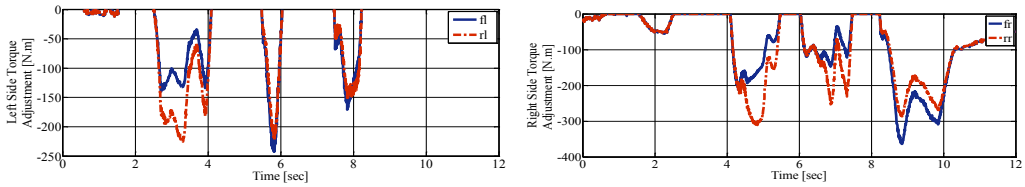

Fig 6.34 Torque adjustment in a DLC maneuver on wet surface with modelling error

6.8 Summary

In this chapter, the original optimal torque distribution algorithm of the HCC was developed to consider the actuation dynamic model. The proposed control algorithm was designed based on a multi-step optimization process at each sampling time that could be incorporated with any actuation system. In this study, an electrohydraulic differential braking system was modeled to prove the effectiveness of the developed algorithm. Simulation and experimental tests were performed on a slippery road condition with a relatively slow actuator to illustrate that modelling could substantially improve vehicle stability and handling performance.

Chapter 7

Conclusion and Future work

7.1 Conclusions and Summary

In this thesis, an integrated stability control structure that can be reconfigured to work with different actuators and drivetrain layouts was designed using optimal control techniques. The control structure is modular and includes an MPC based high-level and a HCC based low-level module. The MPC high-level integrated control module analyzes the vehicle stability at CG and determines the required adjustments to minimize horizontal forces and yaw moment errors. The model predictive technique provides an optimal solution with explicit constraint implementations. The HCC low-level module then, utilizes the model based error analysis in optimal allocation algorithm to generate the required control action through available actuator and prevent vehicle instability. In addition, the original holistic corner control single-step optimization algorithm was developed to encompass the actuator dynamic model for delay compensation and poor performance prevention purposes.

The sub-optimal modular control structure does not only facilitate implementation of the controller on different vehicle configurations with minimum effort, but also results in less computational complexities without sacrificing performance. The closed-loop vehicle performance was evaluated using CarSim simulations as well as experimental test scenarios. The main contributions and findings of this thesis are discussed below.

The incorporation of chassis stability and wheel slip controllers in this thesis resulted in highly optimal control adjustments. A conventional approach is to design a separate module for wheel slip control that adjusts the tire driving/braking torque. The disengagement of chassis stability and wheel slip control modules may lead to ignorance of cross-effects between the modules and allow infrequent contradictions. Whereas, the engagement of these modules minimizes contradictory objectives between them and prevents possible disagreements on control action.

The proposed integrated control structure can be reconfigured to work with various drivetrain and actuator combinations effortlessly. Moving from one drivetrain scheme to another does not require a backward step and extra effort in controller design. The

controller can be configured to work properly with front-wheel-drive, rear-wheel-drive, and all-wheel-drive vehicles. Furthermore, various actuation methods such as differential braking, torque vectoring, active steering, and their combinations are supported with the proposed control structure. Transferring the proposed controller from one vehicle to another with a different drivetrain and actuation system configuration does not require much modification in the tuning process to provide a similar performance. This can be considered as an attractive feature from an industrial perspective since it reduces design and tuning costs.

A multi-step optimization approach was proposed to consider a mathematical description and response-time characteristics of an actuator. This leads to the elimination of the dynamic delay resulting from the actuation evolution process. The effectiveness of the proposed method is evaluated using a relatively slow ABS actuator. A first order dynamic model of the ABS was obtained and contained in the optimization process. As a result, the actual control adjustment was generated sufficiently with a delay compensation technique. In addition, since the actuation model is not encompassed in the MPC prediction model, the online computational burden does not increase drastically, and the controller can be still used for real-time implementation purposes.

The performance evaluation of the proposed control structure was tested using computer simulations in MATLAB /Simulink and CarSim. In order to simulate the vehicle response to driver inputs in a simulation environment, a high-fidelity model of the Electric GM Equinox vehicle was employed. The control structure was executed in a Simulink environment. Several driving scenarios such as full-throttle launch, acceleration in turn, double lane change were designed for controller performance examination. Robust performance of the controller with respect to road adhesion coefficient was sought after with various road surfaces such as dry, wet, snowy, and icy. The vehicle response was compared to uncontrolled or baseline-controlled vehicle responses. Excellent steerability and integrated stability was achieved in simulation results with the proposed controller. The joint use of torque vectoring/differential braking with active steering actuation methods could stabilize the vehicle in extremely severe driving scenarios where stabilization through a unit actuation method was a challenging or impossible task to accomplish. The proposed control structure was also implemented in real-time on dSPACE. Rear-wheel-drive and all-wheel-drive GM Equinox electric vehicles were used to collect test data with different actuation mechanisms such as electric motor and ABS. One of the electric vehicles was upgraded to be equipped with an active steering at front

axle. The real-time qualifications of the control scheme were assessed in several driving scenarios and road surfaces during all seasons of the two-year experiment program. The collected data illustrated that the controller could enhance handling and integrated stability of the vehicle in all scenarios compared to uncontrolled or baseline-controlled cases in experiment as well as simulation.

7.2 Future Work

A few suggestions are made to carry on the research that is conducted in this thesis to further improve the performance of the control structure.

Since the high-level module of the control structure is MPC based, and closed-loop performance of a model predictive controller is highly dependent on the precision of the prediction model, these suggestions are concerned with improving the prediction model accuracy.

- Forward speed change consideration: Considering the vehicle's forward speed in the prediction model as a dynamic state can provide a more precise prediction of the vehicle directional dynamics. For instance, the vehicle forward speed is reduced with differential braking control adjustment. This authorizes more steerability/maneuverability of the vehicle on the same road condition that is not taken into account by a prediction model that neglects forward speed drop. Therefore, more accuracy in prediction will be achieved by considering vehicle speed change.
- Roll dynamics consideration: In high-speed maneuvers on high traction surfaces, the roll angle and roll angle rate are usually significant. In order to prevent rollover in such critical driving scenarios, roll dynamics should be considered in the prediction model. This consideration usually results in more understeer yaw rate response and conservative maneuverability, both of which are necessary for rollover prevention.
- Employment of precise combined-slip tire models: In this thesis, a combined-slip Burkhardt tire model was used for tire cornering coefficient calculations in the piecewise linearized tire model approach. The combined-slip tire characteristic coefficients were obtained by solving an optimization problem (minimization of pure-slip actual and tire model estimated forces). According to the literature, the interaction of the tire longitudinal and lateral forces should not be neglected in the prediction model for instability and tire saturation prognosis. For a certain set of experiment tires, technical properties should be studied through standard test scenarios in different maneuvers, throttle inputs, and forward speeds. The collected combine-slip data should be next analyzed to determine the tire

model parameters on different road surfaces using similar optimization and curve fitting techniques. Careful provision of a combined-slip tire model results in a brand-new set of optimal solutions that were not achievable before with a pure-slip or inaccurate combined slip tire model.

- Employment of nonlinear prediction model: In order to avoid NMPC programming and its computational burden, the nonlinear vehicle dynamic model is linearized about the operating point at each sampling time. Accuracy of model predictive controllers are usually compromised with computational cost, however, nonlinear tire models greatly increase the chance of precise prediction of vehicle responses and provides a globally optimal solution.

In addition to above suggestions, some other modifications can be made in the low-level HCC based module.

- Extension to conventional and hybrid vehicles: In this thesis, an ABS actuator was modelled in the low-level module to consider the effect of actuator dynamics on the torque distribution. In order to use the proposed control structure on conventional and hybrid vehicles, all the components of the driveline such as combustion engines and transmission should also be considered in the modelling procedure. The performance of the control structure can be enhanced to a great extent with such a consideration.

  Lateral load transfer effect: In this thesis, the effect of lateral load transfer is neglected in the distribution algorithm in the low-level module. An identity weight matrix has been used that can be interpreted as an equal normal load and capacity on each tire. However, in high-speed maneuvers on high traction surfaces, the roll angle and roll angle rate are usually remarkable, leading to a significant load transfer from one side to another side. Using normal load estimation methods, a normalized weight matrix can be presented to the controller to foresee the effect of the borne load change.

Bibliography

[1] Transport Canada, "Canadian Motor Vehicle Traffic Collision Statistics 2014 - Collected in Cooperation with the Canadian Council of Motor Transport Administrator," 2014.

[2] A. Høye, "The effects of Electronic Stability Control (ESC) on crashes—An update," *Accid. Anal. Prev.*, vol. 43, no. 3, pp. 1148–1159, 2011.

[3] A. Lyckegaard, T. Hels, and I. M. Bernhoft, "Effectiveness of electronic stability control on single-vehicle accidents," *Traffic Inj. Prev.*, vol. 16, no. 4, pp. 380–386, 2015.

[4] M. Starnes, "Estimating lives saved by electronic stability control, 2008–2012," 2014.

[5] C. G. Bobier, "A phase portrait approach to vehicle stabilization and envelope control." Stanford University, 2012.

[6] K. Koibuchi, M. Yamamoto, Y. Fukada, and S. Inagaki, "Vehicle stability control in limit cornering by active brake," SAE Technical Paper, 1996.

[7] R. C. Hoffman, J. L. Stein, L. S. Louca, and K. Huh, "Using the Milliken Moment Method and dynamic simulation to evaluate vehicle stability and controllability," *Int. J. Veh. Des.*, vol. 48, no. 1–2, pp. 132–148, 2008.

[8] J. He, D. A. Crolla, M. C. Levesley, and W. J. Manning, "Integrated active steering and variable torque distribution control for improving vehicle handling and stability," SAE Technical Paper, 2004.

[9] M. Selby, W. J. Manning, M. D. Brown, and D. A. Crolla, "A comparison of the relative benefits of active front steering and active rear steering when coordinated with direct yaw moment control," in *Proceedings of ASME Int. Mechanical Engineering Congress and Exposition*, 2001, pp. 1–6.

[10] E. Ono, S. Hosoe, H. D. Tuan, and S. Doi, "Bifurcation in vehicle dynamics and robust front wheel steering control," *IEEE Trans. Control Syst. Technol.*, vol. 6, no. 3, pp. 412–420, 1998.

[11] Y. Yasui, K. Tozu, N. Hattori, and M. Sugisawa, "Improvement of vehicle directional stability for transient steering maneuvers using active brake control," SAE Technical Paper, 1996.

[12] M. Klomp, *Longitudinal force distribution and road vehicle handling*. Chalmers University of Technology, 2010.

[13] W. Cho, J. Yoon, J. Kim, J. Hur, and K. Yi, "An investigation into unified chassis control scheme for optimised vehicle stability and manoeuvrability," *Veh. Syst. Dyn.*, vol. 46, no. S1, pp. 87–105, 2008.

[14] M. Abe, Y. Kano, K. Suzuki, Y. Shibahata, and Y. Furukawa, “Side-slip control to stabilize vehicle lateral motion by direct yaw moment,” *JSAE Rev.*, vol. 22, no. 4, pp. 413–419, 2001.

[15] D. Hong, I. Hwang, P. Yoon, and K. Huh, “Development of a vehicle stability control system using brake-by-wire actuators,” *J. Dyn. Syst. Meas. Control*, vol. 130, no. 1, p. 11008, 2008.

[16] D. E. Kirk, *Optimal control theory: an introduction*. Courier Corporation, 2012.

[17] B. D. O. Anderson and J. B. Moore, *Optimal control: linear quadratic methods*. Courier Corporation, 2007.

[18] P. Liu and U. Ozguner, “Distributed Model Predictive Control of Spatially Decoupled Systems Using Switched Cost Functions,” *arXiv Prepr. arXiv1606.02224*, 2016.

[19] M. Canale, L. Fagiano, and M. C. Signorile, “A model predictive control approach to vehicle yaw control using identified models,” *Proc. Inst. Mech. Eng. Part D J. Automob. Eng.*, vol. 226, no. 5, pp. 577–590, 2012.

[20] L. Luo, H. Liu, P. Li, and H. Wang, “Model predictive control for adaptive cruise control with multi-objectives: comfort, fuel-economy, safety and car-following,” *J. Zhejiang Univ. Sci. A*, vol. 11, no. 3, pp. 191–201, 2010.

[21] S. Li, K. Li, R. Rajamani, and J. Wang, “Model predictive multi-objective vehicular adaptive cruise control,” *IEEE Trans. Control Syst. Technol.*, vol. 19, no. 3, pp. 556–566, 2011.

[22] L. Del Re, F. Allgöwer, L. Glielmo, C. Guardiola, and I. Kolmanovsky, *Automotive model predictive control: models, methods and applications*, vol. 402. Springer, 2010.

[23] P. Cortes, J. Rodriguez, C. Silva, and A. Flores, “Delay compensation in model predictive current control of a three-phase inverter,” *IEEE Trans. Ind. Electron.*, vol. 59, no. 2, pp. 1323–1325, 2012.

[24] H. Li and Y. Shi, “Distributed model predictive control of constrained nonlinear systems with communication delays,” *Syst. Control Lett.*, vol. 62, no. 10, pp. 819–826, 2013.

[25] A. Bemporad and M. Morari, “Robust model predictive control: A survey,” in *Robustness in identification and control*, Springer, 1999, pp. 207–226.

[26] P. Falcone, F. Borrelli, H. E. Tseng, J. Asgari, and D. Hrovat, “Linear time-varying model predictive control and its application to active steering systems: Stability analysis and experimental validation,” *Int. J. robust nonlinear Control*, vol. 18, no. 8, pp. 862–875, 2008.

[27] L. Singh and J. Fuller, “Trajectory generation for a UAV in urban terrain, using nonlinear MPC,” in *American Control Conference, 2001. Proceedings of the 2001*, 2001, vol. 3, pp. 2301–2308.

[28] P. Falcone, F. Borrelli, J. Asgari, H. E. Tseng, and D. Hrovat, “Predictive active steering control for autonomous vehicle systems,” *IEEE Trans. Control Syst. Technol.*, vol. 15, no. 3, pp. 566–580,

2007.

[29] G. Palmieri, P. Falcone, H. E. Tseng, and L. Glielmo, “A preliminary study on the effects of roll dynamics in predictive vehicle stability control,” in *Decision and Control, 2008. CDC 2008. 47th IEEE Conference on*, 2008, pp. 5354–5359.

[30] H. Borhan, A. Vahidi, A. M. Phillips, M. L. Kuang, I. V Kolmanovsky, and S. Di Cairano, “MPC-based energy management of a power-split hybrid electric vehicle,” *IEEE Trans. Control Syst. Technol.*, vol. 20, no. 3, pp. 593–603, 2012.

[31] F. Borrelli, P. Falcone, T. Keviczky, J. Asgari, and D. Hrovat, “MPC-based approach to active steering for autonomous vehicle systems,” *Int. J. Veh. Auton. Syst.*, vol. 3, no. 2–4, pp. 265–291, 2005.

[32] J. Asgari and D. Hrovat, “Potential benefits of Interactive Vehicle Control Systems,” *Intern. Rep.*, 2002.

[33] P. Gill, W. Murray, M. Saunders, and M. Wright, “NPSOL–Nonlinear Programming Software,” *Mt. View, CA*, 1998.

[34] Y. Kang and J. K. Hedrick, “Linear tracking for a fixed-wing UAV using nonlinear model predictive control,” *IEEE Trans. Control Syst. Technol.*, vol. 17, no. 5, pp. 1202–1210, 2009.

[35] P. Falcone, “Nonlinear model predictive control for autonomous vehicles,” 2007.

[36] G. Ferrari-Trecate, F. A. Cuzzola, D. Mignone, and M. Morari, “Analysis of discrete-time piecewise affine and hybrid systems,” *Automatica*, vol. 38, no. 12, pp. 2139–2146, 2002.

[37] F. Borrelli, A. Bemporad, and M. Morari, “Predictive control for linear and hybrid systems,” *Cambridge Febr.*, vol. 20, p. 2011, 2011.

[38] M. Morari, M. Baotic, and F. Borrelli, “Hybrid systems modeling and control,” *Eur. J. Control*, vol. 9, no. 2–3, pp. 177–189, 2003.

[39] T. Achterberg, *SCIP-a framework to integrate constraint and mixed integer programming*. Konrad-Zuse-Zentrum für Informationstechnik Berlin, 2004.

[40] S. Di Cairano, H. E. Tseng, D. Bernardini, and A. Bemporad, “Vehicle yaw stability control by coordinated active front steering and differential braking in the tire sideslip angles domain,” *IEEE Trans. Control Syst. Technol.*, vol. 21, no. 4, pp. 1236–1248, 2013.

[41] F. Borrelli, A. Bemporad, M. Fodor, and D. Hrovat, “An MPC/hybrid system approach to traction control,” *IEEE Trans. Control Syst. Technol.*, vol. 14, no. 3, pp. 541–552, 2006.

[42] A. Bemporad and C. Rocchi, “Decentralized linear time-varying model predictive control of a formation of unmanned aerial vehicles,” in *Decision and Control and European Control*

Conference (CDC-ECC), 2011 50th IEEE Conference on, 2011, pp. 7488–7493.

[43] P. Falcone, M. Tufo, F. Borrelli, J. Asgari, and H. E. Tseng, "A linear time varying model predictive control approach to the integrated vehicle dynamics control problem in autonomous systems," in *Decision and Control, 2007 46th IEEE Conference on*, 2007, pp. 2980–2985.

[44] S.-K. Chen, Y. Ghoneim, N. Moshchuk, B. Litkouhi, and V. Pylypchuk, "Tire-Force Based Holistic Corner Control," in *ASME 2012 International Mechanical Engineering Congress and Exposition*, 2012, pp. 133–140.

[45] R. M. Brach and R. M. Brach, "Modeling combined braking and steering tire forces," SAE Technical Paper, 2000.

[46] V. T. Nicholas and T. R. Comstock, "Predicting Directional Behavior of Tractor-Semitrailers when Anti-Skid Brake Systems are Used," in *ASME Winter Annual Meeting, New York, New York*, 1972.

[47] M. G. Pottinger, W. Pelz, and G. Falciola, "Effectiveness of the Slip Circle,'COMBINATOR', Model for Combined Tire Cornering and Braking Forces When Applied to a Range of Tires," SAE Technical Paper, 1998.

[48] J. Svendenius, "Tire modeling and friction estimation," *PhD Theses*, 2007.

[49] D. Kasinathan, A. Khajepour, S.-K. Chen, and B. Litkouhi, "Constrained holistic cornering control," in *American Control Conference (ACC), 2014*, 2014, pp. 3899–3904.

[50] D. Kasinathan, A. Kasaiezadeh, A. Wong, A. Khajepour, S.-K. Chen, and B. Litkouhi, "An Optimal Torque Vectoring Control for Vehicle Applications via Real-Time Constraints," *IEEE Trans. Veh. Technol.*, vol. 65, no. 6, pp. 4368–4378, 2016.

[51] S. Fallah, A. Khajepour, B. Fidan, S.-K. Chen, and B. Litkouhi, "Vehicle optimal torque vectoring using state-derivative feedback and linear matrix inequality," *IEEE Trans. Veh. Technol.*, vol. 62, no. 4, pp. 1540–1552, 2013.

[52] R. de Castro, R. E. Araújo, M. Tanelli, S. M. Savaresi, and D. Freitas, "Torque blending and wheel slip control in EVs with in-wheel motors," *Veh. Syst. Dyn.*, vol. 50, no. sup1, pp. 71–94, 2012.

[53] W. Liang, H. Yu, R. McGee, M. Kuang, and J. Medanic, "Vehicle pure yaw moment control using differential tire slip," in *American Control Conference, 2009. ACC'09.*, 2009, pp. 3331–3336.

[54] M. Amodeo, A. Ferrara, R. Terzaghi, and C. Vecchio, "Wheel slip control via second-order sliding-mode generation," *IEEE Trans. Intell. Transp. Syst.*, vol. 11, no. 1, pp. 122–131, 2010.

[55] V. Ćirović, D. Aleksendrić, and D. Smiljanić, "Longitudinal wheel slip control using dynamic neural networks," *Mechatronics*, vol. 23, no. 1, pp. 135–146, 2013.

[56] H. Mirzaeinejad and M. Mirzaei, “Optimization of nonlinear control strategy for anti-lock braking system with improvement of vehicle directional stability on split-μ roads,” *Transp. Res. Part C Emerg. Technol.*, vol. 46, pp. 1–15, 2014.

[57] P. Falcone, F. Borrelli, J. Asgari, H. E. Tseng, and D. Hrovat, “Low complexity MPC schemes for integrated vehicle dynamics control problems,” in *9th international symposium on advanced vehicle control*, 2008.

[58] J. Wang, Q. Wang, L. Jin, and C. Song, “Independent wheel torque control of 4WD electric vehicle for differential drive assisted steering,” *Mechatronics*, vol. 21, no. 1, pp. 63–76, 2011.

[59] H. Zhao, B. Ren, H. Chen, and W. Deng, “Model predictive control allocation for stability improvement of four-wheel drive electric vehicles in critical driving condition,” *IET Control Theory Appl.*, vol. 9, no. 18, pp. 2688–2696, 2015.

[60] H. Zhou and Z. Liu, “Design of vehicle yaw stability controller based on model predictive control,” in *Intelligent Vehicles Symposium, 2009 IEEE*, 2009, pp. 802–807.

[61] L. Li, F.-Y. Wang, and Q. Zhou, “Integrated longitudinal and lateral tire/road friction modeling and monitoring for vehicle motion control,” *IEEE Trans. Intell. Transp. Syst.*, vol. 7, no. 1, pp. 1–19, 2006.

[62] R. Rajamani, *Vehicle dynamics and control*. Springer Science & Business Media, 2011.

[63] M. Corno, M. Tanelli, I. Boniolo, and S. M. Savaresi, “Advanced yaw control of four-wheeled vehicles via rear active differential braking,” in *Decision and Control, 2009 held jointly with the 2009 28th Chinese Control Conference. CDC/CCC 2009. Proceedings of the 48th IEEE Conference on*, 2009, pp. 5176–5181.

[64] C. Zhao, W. Xiang, and P. Richardson, “Vehicle lateral control and yaw stability control through differential braking,” in *Industrial Electronics, 2006 IEEE International Symposium on*, 2006, vol. 1, pp. 384–389.

[65] T. K. Bera, K. Bhattacharya, and A. K. Samantaray, “Evaluation of antilock braking system with an integrated model of full vehicle system dynamics,” *Simul. Model. Pract. Theory*, vol. 19, no. 10, pp. 2131–2150, 2011.

[66] S. Anwar, “Yaw stability control of an automotive vehicle via generalized predictive algorithm,” in *American Control Conference, 2005. Proceedings of the 2005*, 2005, pp. 435–440.

[67] S. C. Baslamisli, İ. E. Köse, and G. Anlaş, “Gain-scheduled integrated active steering and differential control for vehicle handling improvement,” *Veh. Syst. Dyn.*, vol. 47, no. 1, pp. 99–119, 2009.

[68] P. Koehn and M. Eckrich, “Active steering-the BMW approach towards modern steering technology,” SAE Technical Paper, 2004.

[69] J. Tjonnas and T. A. Johansen, “Stabilization of automotive vehicles using active steering and adaptive brake control allocation,” *IEEE Trans. Control Syst. Technol.*, vol. 18, no. 3, pp. 545–558, 2010.

[70] C. Poussot-Vassal, O. Sename, L. Dugard, and S. M. Savaresi, “Vehicle dynamic stability improvements through gain-scheduled steering and braking control,” *Veh. Syst. Dyn.*, vol. 49, no. 10, pp. 1597–1621, 2011.

[71] G. Burgio and P. Zegelaar, “Integrated vehicle control using steering and brakes,” *Int. J. Control*, vol. 79, no. 5, pp. 534–541, 2006.

[72] J. He, D. A. Crolla, M. C. Levesley, and W. J. Manning, “Coordination of active steering, driveline, and braking for integrated vehicle dynamics control,” *Proc. Inst. Mech. Eng. Part D J. Automob. Eng.*, vol. 220, no. 10, pp. 1401–1420, 2006.

[73] B. Lee, A. Khajepour, and K. Behdinan, “Vehicle stability through integrated active steering and differential braking,” SAE Technical Paper, 2006.

[74] M. Doumiati, O. Sename, L. Dugard, J.-J. Martinez-Molina, P. Gaspar, and Z. Szabo, “Integrated vehicle dynamics control via coordination of active front steering and rear braking,” *Eur. J. Control*, vol. 19, no. 2, pp. 121–143, 2013.

[75] M. Shino and M. Nagai, “Yaw-moment control of electric vehicle for improving handling and stability,” *JSAE Rev.*, vol. 22, no. 4, pp. 473–480, 2001.

[76] S. Sakai, H. Sado, and Y. Hori, “Motion control in an electric vehicle with four independently driven in-wheel motors,” *IEEE/ASME Trans. mechatronics*, vol. 4, no. 1, pp. 9–16, 1999.

[77] F. Li, J. Wang, and Z. Liu, “Motor torque based vehicle stability control for four-wheel-drive electric vehicle,” in *Vehicle Power and Propulsion Conference, 2009. VPPC’09. IEEE*, 2009, pp. 1596–1601.

[78] K. Sawase, Y. Ushiroda, and T. Miura, “Left-right torque vectoring technology as the core of super all wheel control (S-AWC),” *Mitsubishi Mot. Tech. Rev.*, vol. 18, pp. 16–23, 2006.

[79] C. Annicchiarico, M. Rinchi, S. Pellari, and R. Capitani, “Design of a Semi Active Differential to Improve the Vehicle Dynamics,” in *ASME 2014 12th Biennial Conference on Engineering Systems Design and Analysis*, 2014, p. V001T02A006-V001T02A006.

[80] J. Deur, M. Hancock, and F. Assadian, “Bond graph modeling and analysis of active differential kinematics,” in *ASME 2008 Dynamic Systems and Control Conference*, 2008, pp. 1341–1348.

[81] J. Deur, M. Hancock, and F. Assadian, “Modeling of Active Differential Dynamics,” in *ASME 2008 International Mechanical Engineering Congress and Exposition*, 2008, pp. 427–436.

[82] A. Mori and Y. Shibahata, “Drive force control method for four-wheel drive vehicle.” Google Patents, 10-Jun-2008.

[83] F. Zanini, “Design of Thermal Management Control Policies for Multiprocessors Systems on Chip.” Citeseer, 2011.

[84] T. Keviczky, P. Falcone, F. Borrelli, J. Asgari, and D. Hrovat, “Predictive control approach to autonomous vehicle steering,” in *American Control Conference, 2006*, 2006, p. 6–pp.

[85] Huang, Xiaoyu, and Junmin Wang. "Lightweight vehicle control-oriented modeling and payload parameter sensitivity analysis." *IEEE Transactions on Vehicular Technology* 60.5 (2011): 1999-2011.

[86] S. Bingulac and H. F. Vanlandingham, “Discretization and continualization of mimo systems,” *Yugosl. J. Oper. Res.*, vol. 4, no. 7, pp. 27–34, 1994.

[87] T. D. Gillespie, “Fundamentals of vehicle dynamics,” SAE Technical Paper, 1992.

[88] W.-Y. Wang, I.-H. Li, M.-C. Chen, S.-F. Su, and S.-B. Hsu, “Dynamic slip-ratio estimation and control of antilock braking systems using an observer-based direct adaptive fuzzy–neural controller,” *IEEE Trans. Ind. Electron.*, vol. 56, no. 5, pp. 1746–1756, 2009.

[89] Holistic Vehicle Control with Integrated Slip Control”, Amir Khajepour, Alireza Kasaiezadeh, Shih-Ken Chen, Bakhtiar Litkouhi, Pending patent.

[90] C. U. Manual, “Mechanical simulation corporation,” *Ann Arbor, MI*, vol. 48013, 2002.

[91] M. Simulink and M. A. Natick, “The mathworks.” Inc, 1993.

[92] B. A. P. van Duifhuizen, P. D. Hobo, H. Nijmeijer, and A. Khajepour, “Modeling, design and control of an individual wheel actuated brake system,” 2014.

[93] K. Ogata, *Discrete-time control systems*, vol. 2. Prentice Hall Englewood Cliffs, NJ, 1995.